GEOLOGIC MODEL PARAMETERIZATION FOR EFFICIENT HISTORY MATCHING OF CONVENTIONAL AND UNCONVENTIONAL RESERVOIRS

A Dissertation

by

HYUN MIN KIM

Submitted to the Office of Graduate and Professional Studies of
Texas A&M University
in partial fulfillment of the requirements for the degree of

DOCTOR OF PHILOSOPHY

Chair of Committee,	Akhil Datta-Gupta
Committee Members,	Michael J. King
	Eduardo Gildin
	Yalchin Efendiev
Head of Department,	Jeff Spath

August 2019

Major Subject: Petroleum Engineering

ABSTRACT

Proper characterization of heterogeneous rock properties and natural/induced fracture properties is essential for optimizing field development plan and reliable estimation of Estimated Ultimate Recovery (EUR) in conventional and unconventional reservoirs. It is achieved by reconciling the geologic model to the dynamic production and pressure data, otherwise known as history matching. However, history matching of high resolution reservoir models with heterogeneous features and complex fracture properties is challenging because it poses non-uniqueness and stability issues of the highly underdetermined problems. This dissertation proposes novel reservoir model parameterization methods to regularize the ill-posed problem and enhance the efficiency of history matching. We also show practical feasibility of the proposed method by various field cases.

First, the spatial properties of rock and fluid are simultaneously calibrated by grid adjacency-based parameterizations to seismic and pressure data of a heavy oil reservoir in Peace River field, Canada. A novel approach is proposed to integrate frequent time lapse seismic data into high resolution reservoir models based on the seismic onset times. Multi-objective genetic algorithm (MOGA) is utilized to address potential conflicts between seismic and pressure match. We demonstrate the feasibility and robustness of the history matching workflow with MOGA and simultaneous property calibrations in the parameterized transform domain.

Second, a novel multi-resolution parameterization is developed to further improve the regularization when the production data resolution is variant in a reservoir. The multi-resolution parameterization adjusts the modal frequencies or resolutions of basis functions to comply with the various data resolutions. Hence, it better regularizes the undermined history matching problem compared to previous studies.

Third, the grid adjacency-based parameterization is extended to parameterize reservoir models with various fracture geometries simulated by embedded discrete fracture model (EDFM). Analytical basis coefficient sensitivity to production data is calculated with the resulting basis and streamline-based sensitivity. Employing a hierarchical multi-scale workflow and the analytic sensitivity, matrix and fracture properties in EDFM are efficiently calibrated with the proposed parameterization.

DEDICATION

I dedicate this dissertation to my wife, son, and parents of both families.

ACKNOWLEDGEMENTS

I would like to thank my committee chair, Dr. Datta-Gupta for his academic guidance and financial support throughout the course of this research. I also appreciate his support for my professional experiences through internships. I would also like to thank my committee members, Dr. King, Dr. Gildin, and Dr. Efendiev, for their guidance and support.

Thanks also go to MCERI alumni and colleagues. Their mentorship and friendship have contributed to my successful and enjoyable Ph.D. program at Texas A&M University.

Finally, I would like to express my sincere gratitude to my beloved wife, Soyoung Kim, for unconditional support and love she has shown throughout the Ph.D. program.

CONTRIBUTORS AND FUNDING SOURCES

Contributors

This work was supervised by a dissertation committee consisting of Professor Akhil Datta-Gupta (advisor), Michael J. King, and Eduardo Gildin of the Department of Petroleum Engineering and Professor Yalchin Efendiev of the Department of Mathematics.

The seismic onset times in Chapter 2 were calculated by Gill Hetz and the extended collaborated work was published in 2017. In Chapter 4, the EDFM preprocessor was developed by Tsubasa Onishi and streamline tracing in EDFM was developed by Hongquan Chen.

All other work conducted for the dissertation was completed by the student independently.

Funding Sources

This work was made possible by the financial support of the member companies of the Model Calibration and Efficient Reservoir Imaging (MCERI) consortium.

TABLE OF CONTENTS

Page

LIST OF FIGURES

Page

LIST OF TABLES

Page

1. INTRODUCTION AND LITERATURE REVIEW[1]

Proper characterization of heterogeneous rock properties and natural/induced fracture properties is essential for optimizing field development plan and reliable estimation of EUR in conventional and unconventional reservoirs. It is achieved by reconciling the geologic model to the dynamic production and pressure data, called as history matching. However, the history matching of a high resolution reservoir model with heterogeneous features and complex fracture properties is challenging because it poses non-uniqueness and stability issues of the highly underdetermined problem.

This dissertation proposes novel reservoir model parameterization methods to regularize the ill-posed problem and enhance the efficiency of history matching. We also show a practical feasibility of the proposed method by various field cases. In this chapter, we review the previous parameterization researches and present the outline of this dissertation.

1.1. Overview of Parameterization for History Matching

The history matching of high resolution geologic models poses an underdetermined inverse problem because of the large number of reservoir properties defined on grid cells with limited measured data. Therefore, the solution of the inverse

[1] Part of this chapter is from URTeC 2019 Paper 2019-982 "Multi-Resolution Grid Connectivity-Based Transform for Efficient History Matching of Unconventional Reservoirs" by Hyunmin Kim, Feyi Olalotiti-Lawal, Akhil Datta-Gupta, and is reprinted here by permission of the Unconventional Resources Technology Conference, whose permission is required for further use.

problem related to identification of geologic heterogeneity is non-unique and potentially unstable.

The essence of regularization is to address the non-uniqueness and stability issues by either reducing the number of parameters or imposing additional constraints to ensure that the inverse problem is more tractable (Tikhonov 1977, Tarantola 2005, Tonkin and Doherty 2009). In this dissertation, parameterization is used to reduce the number of unknowns, from pixel-based reservoir properties to a low rank approximation of spatial properties with little loss of information. This results in more stable solutions and improved predictive capability of history matched reservoir models.

Of the variety of parameterization methods, the linear transformation of spatial properties in grid cells to parameters in the transform domain has been widely used in hydrology and petroleum engineering (LaVenue and Pickens 1992, Chavent and Bissell 1998, Grimstad et al. 2003, Alcolea, Carrera, and Medina 2006, Jafarpour and McLaughlin 2009, Bhark, Jafarpour, and Datta-Gupta 2011, Bhark, Jafarpour, and Datta-Gupta 2011, Bhark et al. 2011, Hetz, Kim, et al. 2017). It is represented by equation (1.1).

$$u = \Phi v \tag{1.1}$$

where v is m-component column vector of parameters in transform domain, and Φ is a predefined $n \times m$ matrix with columns of interpolation or transformation basis vectors. n is the number of grid cells in a model. Therefore, the updated model is determined by linear combination of basis vectors weighted by v.

The most basic parameterization with linear transformation is segmentation of geologic models into zones of piecewise continuous value. The reservoir property itself or

property multiplier is updated by a constant value within each zone (Jahns 1966, Kang et al. 2015, Olalotiti-Lawal et al. 2017). In case of segmentation, Φ consists of basis vectors of which elements are non-zero constant values only for the corresponding zones and zero for the other zones. Φ should be predefined based on the prior model and does not change in the course of model calibrations. The other common parameterization is Karhunen-Loève transform (KLT) or principal component analysis (PCA) of the property covariance matrix (Karhunen 1947, Loève 1978, Reynolds et al. 1996). The eigenvectors of the covariance matrix are ranked by their corresponding eigenvalues, from largest to smallest, and several eigenvectors with the largest eigenvalues compose the transform basis. In this approach, the basis vectors provide optimal compression if the covariance matrix accurately captures the model geostatistical features. In other words, basis vectors obtained by the KLT approach tend to capture the details of spatial heterogeneity with the fewest transform parameters and result in minimum mean square error for the low rank approximation. Similar to the model segmentation, underdetermined inverse problems can be regularized by reducing the number of unknowns from pixel-based property field to a low rank approximation with little loss of information. However, Jafarpour and McLaughlin (2009) and Bhark, Jafarpour, and Datta-Gupta (2011) discussed the limitations of KLT in a realistic history matching problem of high resolution models: (1) the covariance is generally unknown, resulting in the possibility of suboptimal basis functions if prior model is incorrect, (2) it often entails an eigen-decomposition of large covariance matrices which can be prohibitively expensive.

To overcome these limitations, there have been studies conducted on model-independent parameterization in image processing (Jain 1989, Gonzalez 2001, Rao and Yip 2014). They used the discrete cosine transform (DCT) which is a type of Fourier transform that reconstructs a discrete signal as the sum of cosine harmonics (Britanak, Yip, and Rao 2010). Jafarpour and McLaughlin (2009) applied DCT in reservoir characterization, and Bhark, Jafarpour, and Datta-Gupta (2011) developed it to the multiscale history matching workflow. Φ in equation (3.1) of DCT also refers to a linear transformation matrix of which columns are each cosine function with corresponding frequency that depicts a harmonic pattern of grid. As each cosine function is calculated based not on the properties in grid cells, but on the grid structure, basis vectors are constructed independent of the prior model. Each transform parameter in **v** is merely the amplitude of each cosine function. Therefore, DCT basis vectors are calculated analytically only once with cosine functions for a given inverse problem, and considerably smaller parameter set (v) updates the prior model during calibrations. This parameter reduction is possible because DCT has a strong compression performance, so it is able to capture larger scales of spatial continuity and heterogeneity with a significantly reduced number of parameters. In addition, mapping transform parameter to spatial property is achieved simply by the transpose of basis vectors due to their pairwise orthonormality. However, to calculate DCT transformation matrix, the grid cells should be rectangular and of uniform thickness in certain orientation to satisfy the underlying assumption of periodicity (Bhark, Datta-Gupta, and Jafarpour 2011, Bhark, Jafarpour, and Datta-Gupta 2011). Bhark, Jafarpour, and Datta-Gupta (2011) developed the grid connectivity-based

transform (GCT) as a generalization of the DCT basis for generic grid geometries. The GCT basis vectors are defined as the eigenvectors of a Laplacian matrix that has two-point grid connectivity information, so they depend solely on the grid structure independent of grid properties. They proved that in the case of a regular periodic and fully connected grid, the GCT basis vectors are same as those of DCT in either structured or unstructured grid geometry. They also demonstrated that GCT is applicable for reservoir model calibrations in any grid geometries. The detailed concept and illustrations for the re-parameterization are presented in Appendix A.

1.2. Research Objectives and Dissertation Outline

This research proposes novel reservoir model parameterizations for efficient history matching and shows practical feasibility of the proposed method by field-scale applications to both conventional and unconventional reservoirs. The outline of this dissertation is as follows:

- Integrate frequent time lapse (4D) seismic data into high resolution reservoir model by utilizing simultaneous adjacency-based transforms of rock properties, fluid saturations, and temperature and by utilizing a novel seismic onset time approach (Chapter 2)
- Propose a multi-resolution grid connectivity-based transform for efficient history matching by adaptively coarsening the grid Laplacian according to the data resolution (Chapter 3)

- Propose a hierarchical multi-scale history matching workflow for embedded discrete fracture model (EDFM) using a novel parameterization method combined with streamline-based sensitivity (Chapter 4)

2. GRID ADJACENCY-BASED TRANSFORM FOR HISTORY MATCHING OF FREQUENT SEISMIC SURVEYS USING ONSET TIMES[2]

2.1. Chapter Summary

In this chapter, we present a novel and efficient approach to integrate frequent time lapse (4D) seismic data into high resolution reservoir models based on seismic onset times, defined as the calendar time when the seismic attribute crosses a pre-specified threshold value at a given location. Our approach reduces multiple time-lapse seismic survey data into a single map of onset times, leading to substantial data reduction for history matching while capturing all relevant information regarding fluid flow in the reservoir. Hence, the proposed approach is particularly well suited when frequent seismic surveys are available using permanently embedded sensors.

Grid adjacency-based transform (ABT) effectively parameterizes spatial distribution of reservoir properties into a low rank property descriptions, resulting in significantly reduced parameter set size. It regularizes history matching problems and addresses the non-uniqueness and stability issues. We demonstrate the power and efficacy of the parameterization method first using a synthetic example. In a field example, large-scale features such as regional permeabilities, pore volumes, temperature and fluid saturations are adjusted to match seismic and bottom-hole pressure data using a Pareto-based multi-

[2] Reprinted with permission from "History Matching of Frequent Seismic Surveys Using Seismic Onset Times at the Peace River Field, Canada" by Hetz, Gill, Hyunmin Kim, Akhil Datta-Gupta et al., 2017, SPE-187310-MS, Copyright 2017 by Society of Petroleum Engineers

objective history matching workflow. Rather than an artificial subdivision of the domain, multiple zones of spatially continuous heterogeneity are captured based on an eigen-decomposition of the grid Laplacian.

The field example involves steam injection into a heavy oil reservoir at Pad 31 in the Peace River Field (Alberta, Canada) with daily time lapse seismic surveys recorded by a permanently buried seismic monitoring system (Lopez et al. 2015). In our specific application, we have used time lapse data (in terms of two-way travel time) from a Cyclic Steam Stimulation (CSS) cycle in the pad with a total of 175 seismic surveys. With a single onset time map derived from this data we were able to capture the propagation of pressure and saturation fronts and significantly improve the dynamic model through the estimation of permeability distribution, fluid saturation evolution and swept volume. With this methodology we correctly identified and further refined the location of stimulated zones as inferred before from reservoir engineering judgement and manual adjustments aiding better understanding of CSS behavior in the studied field. The results clearly demonstrate the effectiveness of the onset time approach for integrating large number of seismic surveys by compressing them into a single map. Also, the onset times appear to be relatively insensitive to the petro elastic model but sensitive to the steam/fluid propagation, making it a robust method for history matching of time lapse surveys.

2.2. Introduction

Reservoir monitoring is an integral part of reservoir management during enhanced oil recovery, where for example, steam (Eastwood et al. 1994) and CO_2 are injected to

ensure injectant conformance and flood front management, maximizing recovery and minimizing operational costs. The availability of dense areal information from frequent 4D seismic offers a great opportunity to achieve these goals. It enables better understanding of reservoir sweep and flow patterns, reduction of the uncertainty in the reservoir properties and adjustment of the operational strategy to restore conformance and optimize recovery (Przybysz-Jarnut et al. 2015, Watanabe et al. 2017). However, it also poses new challenges in terms of dynamic reservoir modeling and seismic history matching to infer changes in the state of the reservoir. The underlying issues for successful monitoring of reservoir fluid-flow systems using time-lapse data were reviewed by Lumley (2001) and Behrens et al. (2001).

Traditionally, time-lapse seismic techniques for inferring flow properties have been focused on amplitude, traveltime, and waveform changes. For example, Tura and Lumey (1999) and Landrø, Digranes, and Strønen (2001) used the inverted seismic responses and amplitude versus offset inversion to discriminate between the pressure and saturation changes. Arenas, van Kruijsdijk, and Oldenziel (2001) used the compressional velocity to calibrate the permeability field. Vasco et al. (2004) used reflection amplitude to update the flow properties, where the sensitivity of seismic amplitude is analytically computed. Dadashpour, Landrø, and Kleppe (2007), Dadashpour et al. (2009), and Dadashpour et al. (2010) applied the propagator-matrix method (Stovas and Arntsen 2006) to generate the seismic traces from a stack of plane layers and calibrate reservoir properties by a Gauss-Newton optimization technique. Rey et al. (2012) applied a streamline-based sensitivity calculation to integrate the seismically derived water saturation changes and

the acoustic impedance differences and demonstrated field-scale applications. Watanabe et al. (2017) used the time-lapse changes in acoustic impedance to update grid cell permeability with a hierarchical approach involving global and local updates. Cho et al. (2019) investigated capabilities of a multiscale method that can deal with fine scale heterogeneities of the reservoir layer and more coarsely meshed rock properties in the surrounding domains in the same fashion.

Although such methods can often detect changes in geophysical quantities and were successfully applied to field cases, relating geophysical changes to quantified changes in the fluid flow properties remains a fundamental challenge (Vasco, Daley, and Bakulin 2014). The connection between the current state of the reservoir and the geophysical observations relies on underlying rock physics model that can have considerable uncertainty. One of the main uncertainties comes from the fact that these models are built based on laboratory measurements that may not be representative of the field conditions. This makes seismic history matching difficult as the estimation results highly depend on the saturation mapping chosen and can be quite different, while originating from the same seismic measurement. Another difficulty is integrating the data from Permanent Reservoir Monitoring systems (PRM), where tens to hundreds time-lapse seismic surveys may be available.

To deal with the above-mentioned issues we present a novel and computationally efficient approach for frequent time lapse seismic integration using the concept of onset time (Vasco, Daley, and Bakulin 2014, Vasco et al. 2014). The onset times are defined as the calendar times at which geophysical observations begin to deviate from their initial or

background values above a pre-defined threshold value. It allows compression of multiple seismic surveys into a single map of front propagation, which can be used to effectively guide history matching and for dynamic model updating. The onset time can be related to the arrival time of a particular physical phenomenon (e.g. saturation front and/or pressure front). Hetz, Kim, et al. (2017) demonstrated the power and the utility of the onset time methodology for history matching using synthetic study and field application. They compared the traditional seismic integration based on matching the magnitudes of seismic observations with the onset time approach.

The history matching of high resolution geologic models poses an underdetermined inverse problem due to the large number of reservoir properties defined on grid cells with limited measured data. Therefore, the solution of the inverse problem related to identification of geologic heterogeneity is non-unique and potentially unstable. To address these issues, there have been various parameterization studies (LaVenue and Pickens 1992, Chavent and Bissell 1998, Grimstad et al. 2003, Alcolea, Carrera, and Medina 2006, Jafarpour and McLaughlin 2009, Bhark, Jafarpour, and Datta-Gupta 2011, Bhark, Jafarpour, and Datta-Gupta 2011, Bhark et al. 2011). Bhark, Jafarpour, and Datta-Gupta (2011) developed the grid connectivity-based transform (GCT) as a generalization of the discrete cosine transform (DCT) (Jain 1989, Gonzalez 2001, Rao and Yip 2014) basis for generic grid geometries. Bhark, Datta-Gupta, and Jafarpour (2011) applied GCT with prior static property (adjacency-based transform; ABT) in a field case to calibrate permeability field to water production and bottom-hole pressure data.

In this research, the field example involves steam injection into a heavy oil reservoir at Pad 31 in the Peace River Field (Alberta, Canada) with daily time lapse seismic surveys (in terms of two-way travel time) recorded by a permanently buried seismic monitoring system. We simultaneously update static reservoir properties, initial temperature, and initial fluid saturation to match bottom-hole pressure and onset time derived from the continuous seismic land monitoring, using ABT and Pareto-based multi-objective history matching workflow.

2.3. Background and Methodology

In this section, we introduce our proposed approach of integrating time lapse seismic into the reservoir model using onset-times. We start with an explanation of the data integration workflow and illustrate the concept of onset time in a stepwise manner using a simple synthetic example. The workflow and re-parameterization analysis of ABT are also given in this section compared with GCT.

2.3.1. Onset Time of Frequent Seismic Data

2.3.1.1. From Multiple Surveys to a Single Map of Onset Times

The traditional approach to time lapse seismic data integration uses multiple seismic surveys and integrates seismic attributes (amplitudes or travel times) or changes thereof via dynamic modeling and history matching. In contrast, the onset time methodology collapses multiple seismic surveys into a single map of changes propagating

in the reservoir. The onset times (Vasco et al. 2014) are defined as the calendar times at which measured time-lapse attributes begin to deviate from their initial values above a pre-defined threshold value. The magnitude and sign of the threshold value depends on the signal-to-noise ratio of the seismic dataset and the particular physical phenomenon that is being tracked (e.g. saturation front and/or pressure front).

2.3.1.2. Time Lapse Seismic Data and Petro Elastic Model (PEM)

In order to connect between the state of the reservoir and the geophysical observation, we have to rely on a PEM to calculate the elastic properties of the rock that vary in time as a result of changes in the dynamic reservoir properties: fluid saturations, reservoir pressure, and temperature etc. The relationship between the seismic properties and the rock elastic properties can often be described by Gassmann's equations (Gassmann 1951) for calculating the effective bulk modulus of the entire saturated rock. The model relates the bulk modulus of a rock to its pore, frame, and fluid properties. The Gassmann's relation is valid in most practical cases; however, it can have considerable uncertainty, particularly in the model used to describe how the fluids are distributed within the pore space. The onset time, as opposed to magnitude matching, seems to be insensitive to the specific model used for mapping the fluid saturations (Vasco et al. 2014), and thus more robust against uncertainties in the underlying rock physics model.

2.3.1.3. Five-Spot Synthetic Case

We first illustrate the major steps involved in the onset time data integration procedure using a two-dimensional synthetic application. The model is composed of 50×50 grid cells and involves reservoir production in an inverted 5-spot pattern with four producers located at the corners and one central injector. The wells are constrained by the historical (constant) liquid flow rates, and the injection program starts simultaneously with the production of the reservoir. The permeability field shown in Figure 2.1 is generated using the sequential Gaussian simulation with well permeability values as conditioning data. The observed 4D seismic data were generated from the permeability field using a commercial reservoir simulator and a petro-elastic model. Over an interval of 2080 days, a total of 8 time-lapse seismic surveys (260 days each) in the form of acoustic impedance maps, are available for integration.

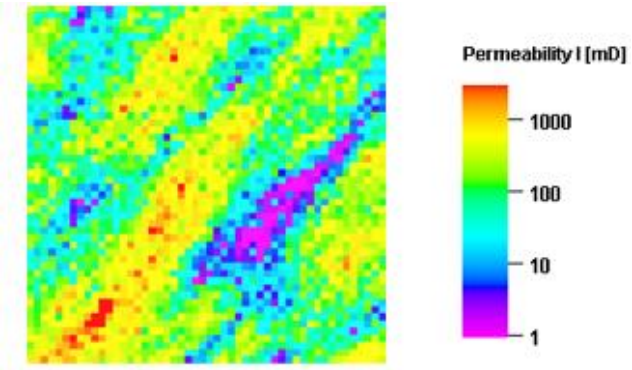

Figure 2.1 Permeability field for the illustration of onset time

In our onset time approach, the first step is to define a threshold value that allows a meaningful conversion of multiple attribute maps to a single map of onset time. The pre-defined threshold has two main roles: (1) to ensure that the magnitude of seismic observation is above the noise level, which determines the value of the threshold, (2) to define the physical phenomenon that is being tracked, which specifies the sign of the threshold value. Time-lapse seismic data are typically noisy due to non-repeatable noise, environmental noises, sensors spacing, and changes in near surface propagation due to variations in the water table or in the overlying water column. These variations lead to seismic signals even when there are no dynamic changes within the reservoir, and thus a need for threshold value to distinguish between noise and meaningful signal. In this example, we define the threshold to be 5% above the acoustic impedance of the baseline survey (that is, before the injection started). This increase above the threshold corresponds to an increase in the bulk density and velocity of the seismic waves, which results from replacement of "softer" for "harder" reservoir fluids (e.g. oil or gas being displaced by the injected water). Figure 2.2 illustrates the procedure of converting the time-lapse acoustic impedance data to an onset time map. For each cell in our model we indicate the calendar time at which the measured acoustic impedance crosses the threshold value. This time (day), will be recorded in the onset time map, and the spatial location is not visited anymore. Thus data from multiple attribute maps is reduced to a single onset time map (Figure 2.2(c)). The contours of the onset time provide a display of the changes propagating in the reservoir.

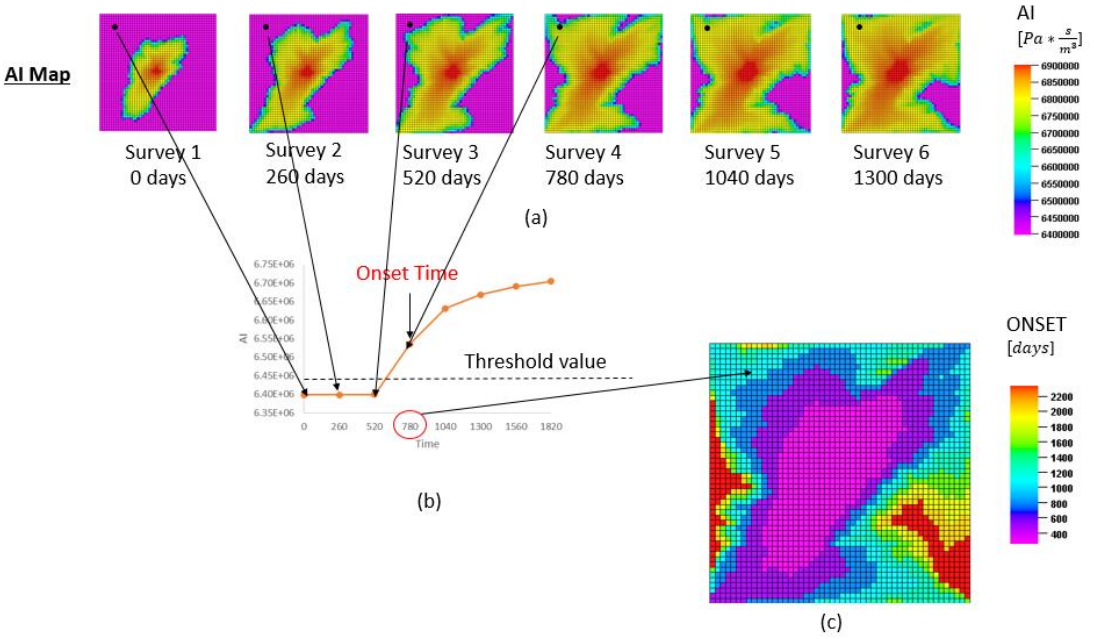

Figure 2.2 Illustration of onset time – conversion of multiple attribute maps (AI) to onset time map. (a) A sample of 6 attribute maps (AI). (b) Plot of the seismic response of a specific cell (black do in (a)) to indicate the onset time. (c) Onset time map after converting from seismic attribute to calendar time. The contours display the front propagation

2.3.2. Adjacency-Based Transform

The literature survey and detailed mathematical formulation of the GCT are explained in chapter 3. In this section, the ABT is compared with GCT in terms of Laplacian matrix formulation and re-parameterization analysis.

2.3.2.1. Parameterization with Prior Information

Figure 2.3 shows the workflow of basis function calculation both for GCT and ABT. A similarity matrix is first constructed and Laplacian matrix is calculated by equation (2.1).

$$L = D - A \tag{2.1}$$

L is a Laplacian matrix, and A is the $N \times N$ similarity matrix, where N is the total number of grids in a reservoir model. D is the $N \times N$ diagonal matrix, known as degree matrix, whose entries are row sums of A as in equation (2.2).

$$d_i = \sum_{j=1}^{N} a_{i,j} \tag{2.2}$$

The Laplacian matrix is then eigen-decomposed and selected eigenvectors will define the basis functions.

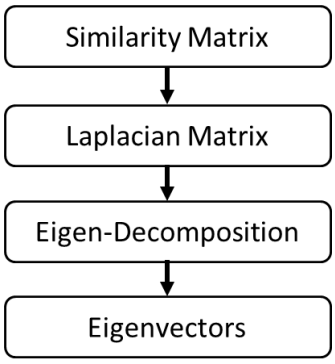

Figure 2.3 Workflow of basis function calculation for GCT and ABT

The only difference between GCT and ABT is the method of constructing the similarity matrix, whose elements represent the degree of similarity among every grid cell pairs. In GCT, each component of the similarity matrix is defined by equation (2.3).

$$a_{i,j} = \begin{cases} 1 & if \ \ neighbored \\ 0 & otherwise \end{cases} \tag{2.3}$$

The grid cells in direct connection are considered as similar and both of them are assigned a value of unity. The grid cell has no similarity with the others without direct connectivity. Therefore, GCT takes into account only grid connectivity represented by unity or zero in the similarity matrix. However, an element of the similarity matrix in ABT is defined by equation (2.4).

$$a_{i,j} = \exp\left(\frac{-\left\|p_i - p_j\right\|_2^2}{\sigma_p}\right)\begin{cases} \exp\left(\dfrac{-\left\|x_i - x_j\right\|_2^2}{\sigma_x}\right) & if \ \ \left\|x_i - x_j\right\| < r \\ 0 & otherwise \end{cases} \tag{2.4}$$

$p_{i,j}$ is the property value of the grid cell, $x_{i,j}$ is the coordinate of grid cell centroid, and r is a Euclidean cutoff distance, beyond which the similarity is considered to be zero regardless of their properties and distance. Therefore, ABT considers grid cell properties as well as their distance.

Figure 2.4 compares Laplacian matrix of GCT and ABT in a 9-points grid system. Figure 2.4(a) shows a 9-points grid system where a color represents the property value in each grid cell and values on white lines are the similarities between a center grid cell and others calculated by equation (2.4). Blue boxes in Figure 2.4(b) and Figure 2.4(c) clearly show the difference between GCT and ABT. While GCT Laplacian matrix has the direct grid connectivity information, ABT Laplacian matrix includes all the similarity values around the corresponding grid cell. For example, as there is a large property difference between the top-left grid cell and the center grid cell, the similarity is calculated to be almost zero, as the first element of the blue box. On the other hand, the property value of the middle-right grid cell is similar to that of center grid cell and the distance between two grid cells is small, the similarity is calculated to be closer to unity, 0.8. It is shown as the 6th element of the blue box. Eigenvectors of the corresponding Laplacian matrices will define our basis functions.

(a)

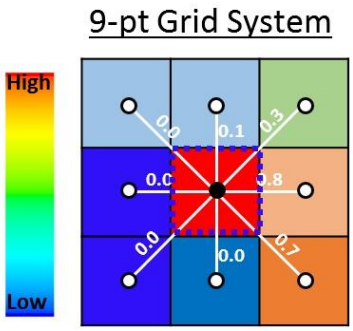

(b)

Laplacian Matrix (GCT)

2	-1	0	-1	0	0	0	0	0
-1	3	-1	0	-1	0	0	0	0
0	-1	2	0	0	-1	0	0	0
-1	0	0	3	-1	0	-1	0	0
0	-1	0	-1	4	-1	0	-1	0
0	0	-1	0	-1	3	0	0	-1
0	0	0	-1	0	0	2	-1	0
0	0	0	0	-1	0	-1	3	-1
0	0	0	0	0	-1	0	-1	2

(c)

Laplacian Matrix (ABT)

1.8	-1.0	0.0	-0.8	0.0	0.0	0.0	0.0	0.0
-1.0	2.5	-0.5	-0.7	-0.1	-0.2	0.0	0.0	0.0
0.0	-0.5	1.7	0.0	-0.3	-0.9	0.0	0.0	0.0
-0.8	-0.7	0.0	3.3	0.0	0.0	-1.0	-0.8	0.0
0.0	-0.1	-0.3	0.0	1.9	-0.8	0.0	0.0	-0.7
0.0	-0.2	-0.9	0.0	-0.8	3.1	0.0	-0.3	-0.9
0.0	0.0	0.0	-1.0	0.0	0.0	1.9	-0.9	0.0
0.0	0.0	0.0	-0.8	0.0	-0.3	-0.9	2.4	-0.4
0.0	0.0	0.0	0.0	-0.7	-0.9	0.0	-0.4	2.0

Figure 2.4 Laplacian matrix comparison of GCT and ABT in a 9-points grid system

2.3.2.2. Re-parameterization Analysis of ABT

For the two dimensional reference permeability field in Figure 2.5(a), basis functions of GCT and ABT are compared in Figure 2.5(b) and (c). While GCT basis functions have grid connectivity information only, ABT entails property values in its basis functions.

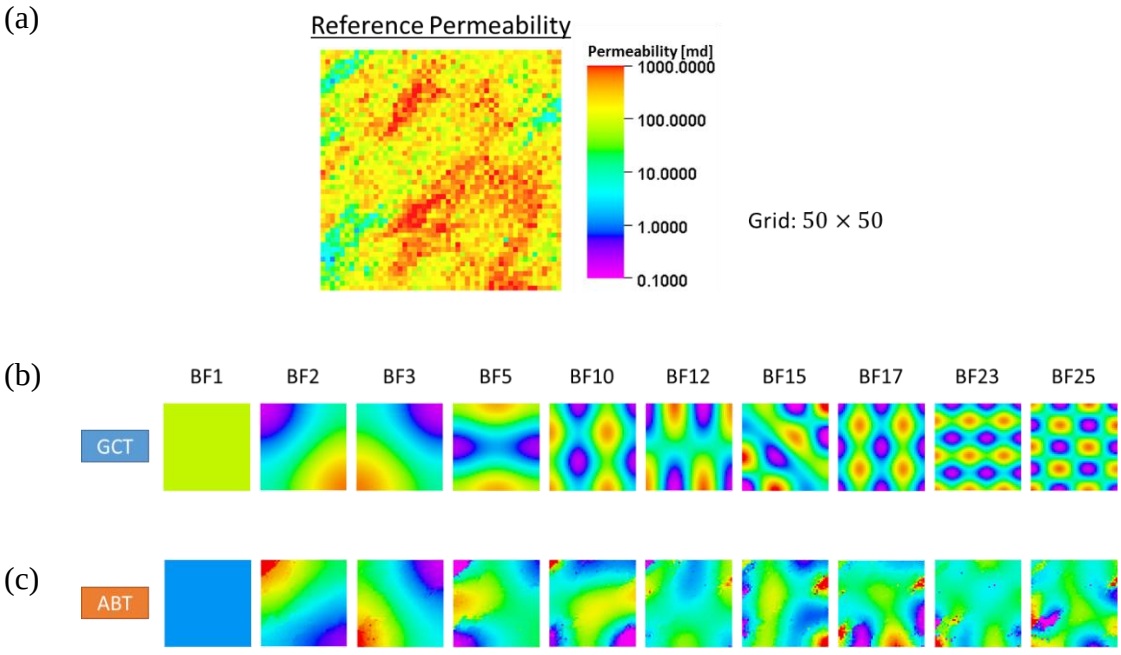

Figure 2.5 Basis function comparison of GCT and ABT in a 50×50 grid system. (a) Reference permeability field. (b) GCT basis functions. (c) ABT basis functions

Reconstructed permeability fields of GCT and ABT with different number basis functions are shown in Figure 2.6. Qualitatively indicated from Figure 2.6, ABT has a higher compression power than GCT.

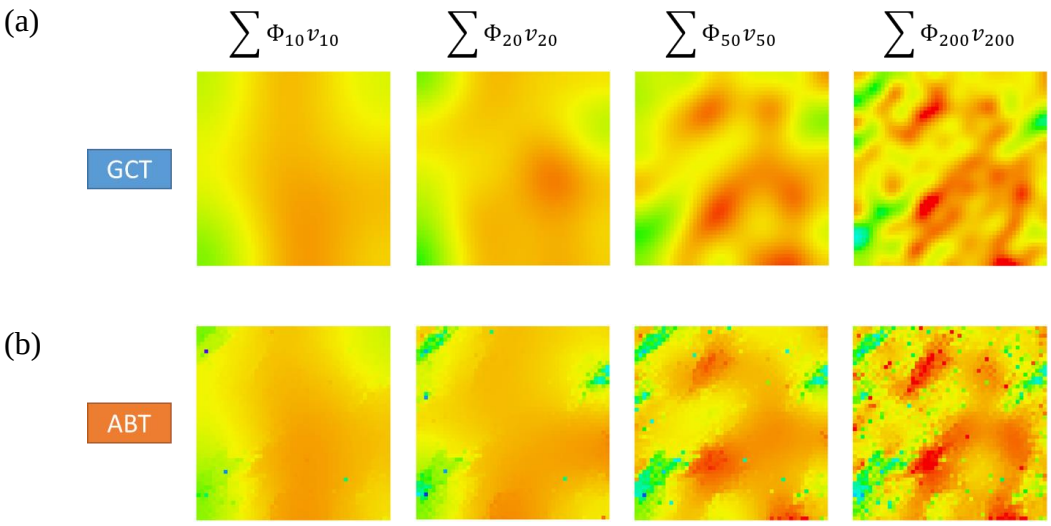

Figure 2.6 Re-parameterized permeability fields of GCT and ABT with different number of basis functions

To quantitatively compare the compression power, root mean square errors (RMSE) as in equation (2.5) between the reconstructed permeability field and the reference field are calculated. RMSE's of GCT and ABT are compared in Figure 2.7.

$$RMSE = \frac{1}{N}\sqrt{\sum_{i=1}^{N}\left|k_i^{reference} - k_i^{re-parameterized}\right|^2} \tag{2.5}$$

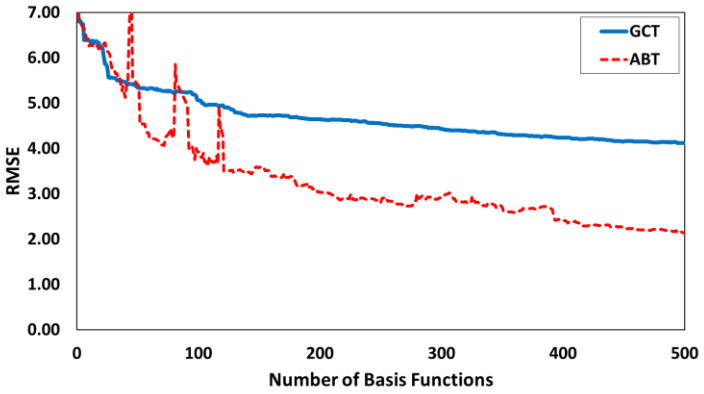

Figure 2.7 RMSE comparison of GCT and ABT

2.4. Application – Field Case at Peace River, Pad 31

2.4.1. Field History and Data

The Peace River is a heavy oil field in Alberta, Canada. The field has been under several thermal recovery schemes including Cyclic Steam Stimulation (CSS) and Steam Assisted Gravity Drainage (SAGD) to increase the recovery of the bitumen deposits. These processes led to limited recovery of the bitumen originally in place, partly due to insufficient stimulation of the reservoir volume. Recently, one of the production pads, Pad 31, was re-developed with six new horizontal steam injectors (in green, Figure 2.8) and operated as a Top Down Steam Drive (TDSD). This new development was monitored with a permanent seismic monitoring system (the monitoring period was between May 2014 and May 2016) that provides snapshots of reservoir state on a daily basis (Hetz, Datta-Gupta, et al. 2017, Lopez et al. 2015). In addition to the ongoing TDSD, one of the

producers (31-08 well, Figure 2.8) has undergone CSS to promote communication with the northern part of the pad.

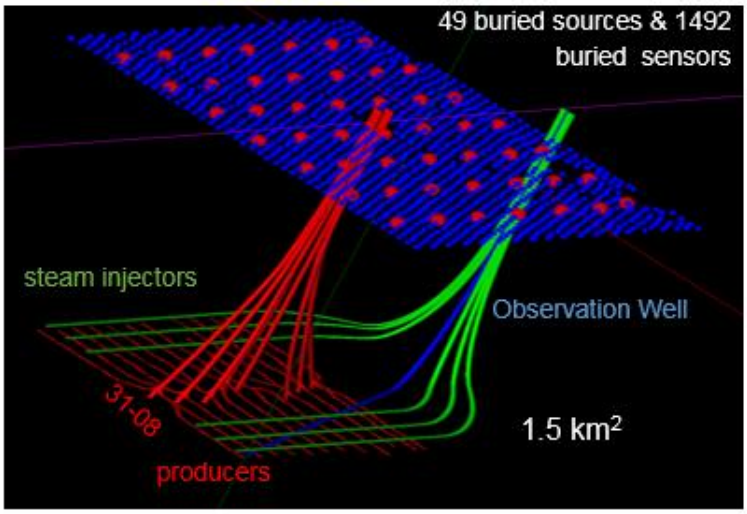

Figure 2.8 Pad 31 horizontal production wells (red), injection wells (green), and observation well (blue). Also shown are seismic sources (red dots) and receivers (blue dots). Producer 31-08 underwent CSS and is the focus of this study

The fact that the well under consideration is relatively isolated from the rest of the pad and did not seem to be influenced by the ongoing TDSD, allows one to use a sector model for dynamic modeling on a fine grid (Przybysz-Jarnut et al. 2016). The seismic data is translated into time shift maps, expressing the travel time changes in the seismic wave propagation across the reservoir between a chosen baseline survey (e.g. the start of the cycle) and subsequent monitor surveys. Over the CSS cycle, a total of 175 time lapse

seismic surveys are available for integration (Figure 2.9) and bottom-hole pressure data is also available (Figure 2.10).

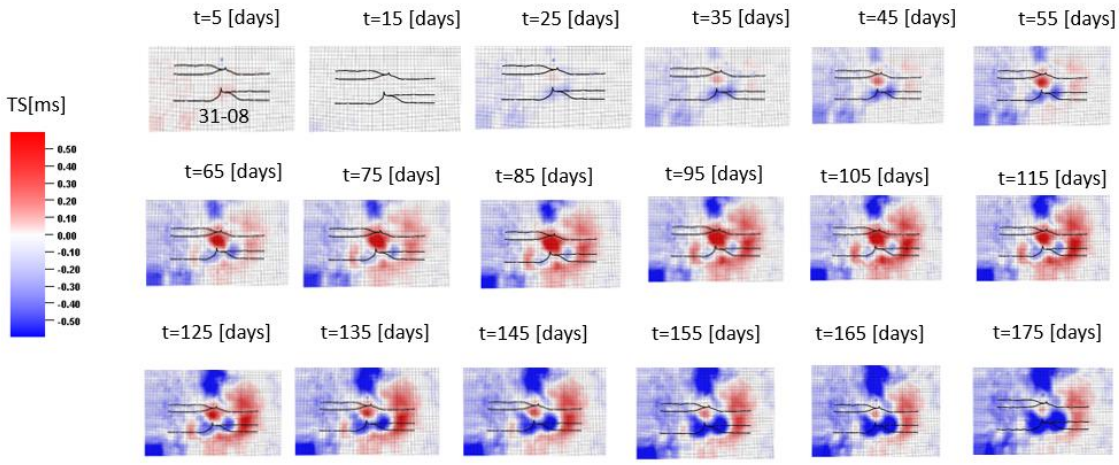

Figure 2.9 Seismic observations in well 31-08 (top view). 18 samples of time shift maps are shown out of 175 time shift maps that are available for integration

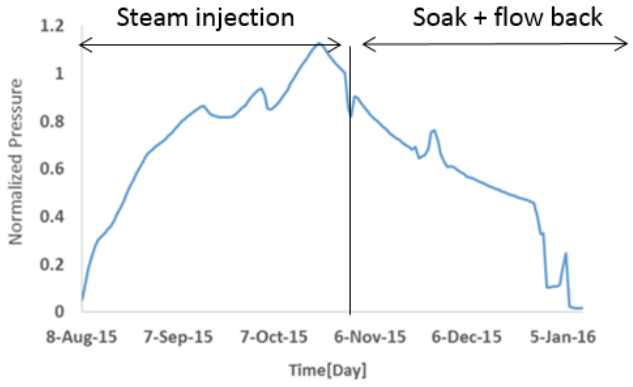

Figure 2.10 Normalized bottom-hole pressure response over the CSS cycle

The amount and the nature of the recorded time shift data, which combine the effects of temperature, pressure and phase saturation changes in the reservoir, make it extremely challenging and time consuming for manual or even assisted history matching. To overcome these problems, we use our onset time approach to integrate the time lapse seismic data into the model. Based on the signal to noise ratio of the seismic dataset, we define the threshold as a decrease of 0.1[mS] in the time-shift. At the first part of the cycle (e.g. the injection), the onset time is associated with water phase replacing gas phase as a result of steam injection. In the second part (e.g. soak), the onset is related to pressure diffusion after the injection ceases.

For the field application, the first step in our data calibration procedure is to sample the seismic observations into the reservoir model grid to be able to compare it with the simulation response. The calculated onset time map is shown in Figure 2.11.

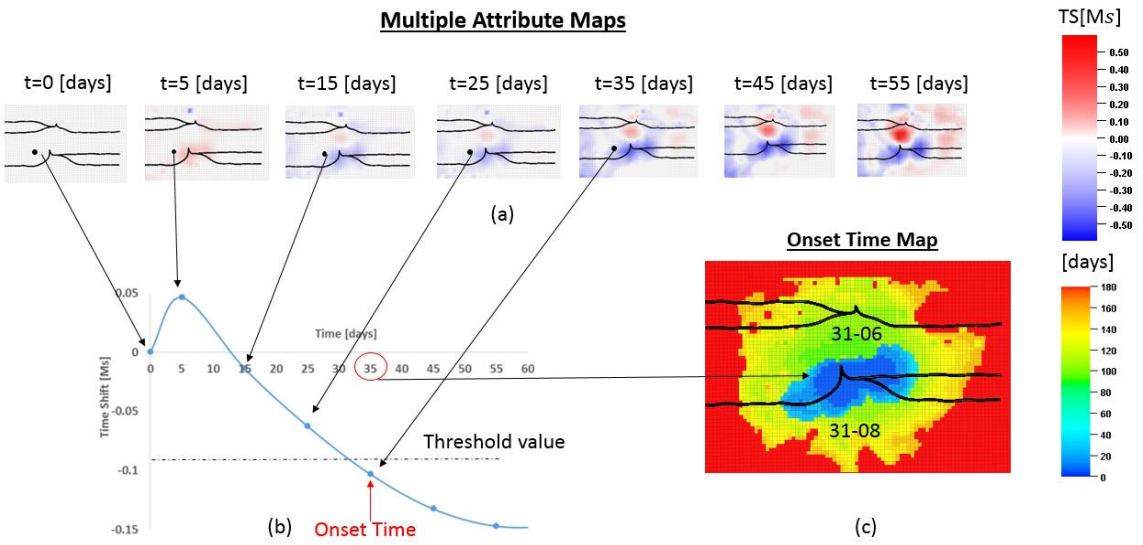

Figure 2.11 Conversion of multiple attribute maps (time shift) to onset time map. (a) A sample of 7 attribute maps (time shifts) out of 175 that are available for integration. (b) A plot of the seismic response of a specific cell (label as black dot in (a)) to indicate the onset time. (c) The onset time map after converting from seismic attribute to time. The contours display the front propagation

2.4.2. History Matching of Onset Time and BHP

Since the heavy oil field has been under production for more than ten years with different thermal recovery schemes, the significant uncertainty lies in the initial conditions for this re-development and the flow properties of the reservoir at the beginning of the CSS cycle. Our objective is to calibrate the initial saturations, initial temperature, porosity, and the permeability field to the 4D seismic and the pressure data acquired to understand the unexpected reservoir behavior during CSS cycle in 31-08 well with much less injected volume and higher than expected injection pressure. Our sensitivity analysis (Hetz, Datta-Gupta, et al. 2017) showed that above mentioned parameters have the largest influences on the matching quality. The history matching was performed with ABT parameterization

and MOGA workflow with the parameters in Table 2.1. A steam injection period is used for history matching and a production period is used to validate the calibrated models.

Table 2.1 Parameters for history matching in Peace River field case

Objective Function	Onset time misfit Bottom-hole pressure misfit
Variable	Permeability (10 basis coefficients) Porosity (10 basis coefficients) Initial gas saturation (10 basis coefficients) Initial water saturation (10 basis coefficients) Initial temperature (10 basis coefficients)
Constraint	Water rate
Number of Basis Functions	50
Population Size	150
Maximum Generation	30

Initial misfits for onset time and BHP are shown in Figure 2.12. It indicates that the initial model could not capture the correct fluid propagation and energy in the reservoir.

(a)

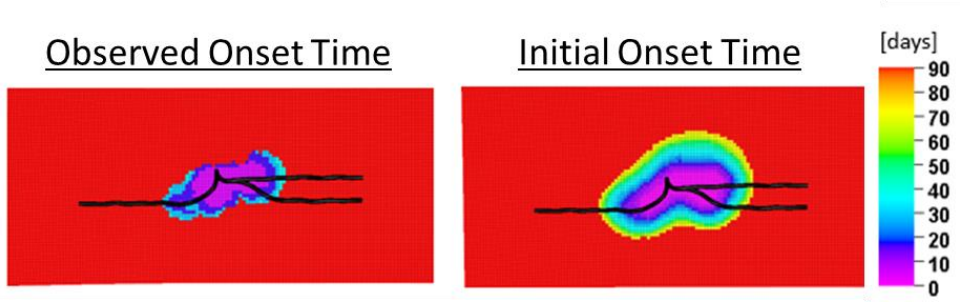

(b)

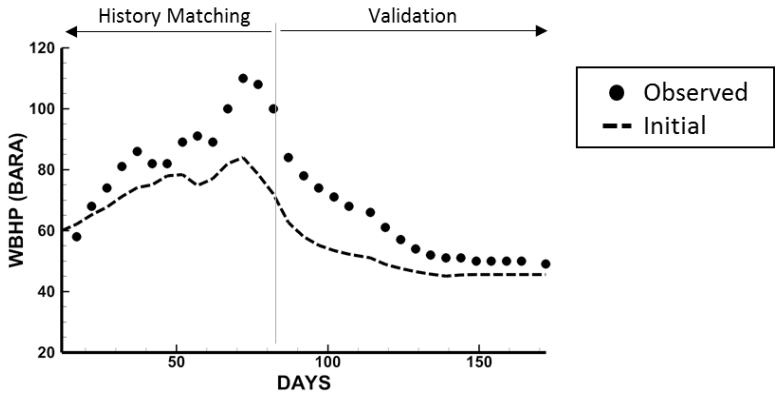

Figure 2.12 Initial misfits for onset time and BHP in Peace River Field Case

The first step in our data calibration procedure is to parameterize the initial saturations, initial temperature, porosity and permeability using ABT parameterization. While most of the parameters were initialized based on the geologic model or uniformly distributed, the initial temperature distribution was interpolated from the tubing head

temperature (THT) at the beginning of the cycle, within the observed onset time map region. Since the gas saturation was uniformly distributed, we use the observed onset time as prior knowledge to calculate its adjacency matrix for the ABT parameterization. A Total of 50 basis functions (10 per each property) and corresponding basis coefficients are used to modify the initial properties in the course of model calibration. As an example, the ABT basis functions of layer 17 are shown in Figure 2.13. Note that the variations in the ABT basis functions result from the prior property heterogeneity.

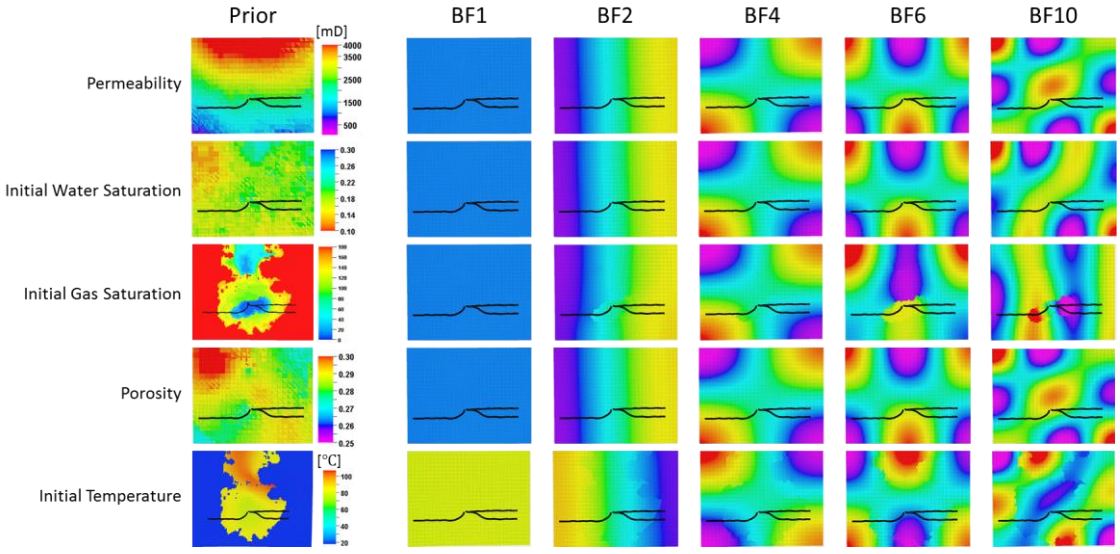

Figure 2.13 ABT basis functions of parameter fields at layer 17

Both onset time and BHP misfits were significantly reduced through MOGA as shown in Figure 2.14. The large number of simulations allows us to test different combinations of the model parameters and alternative dynamic realizations.

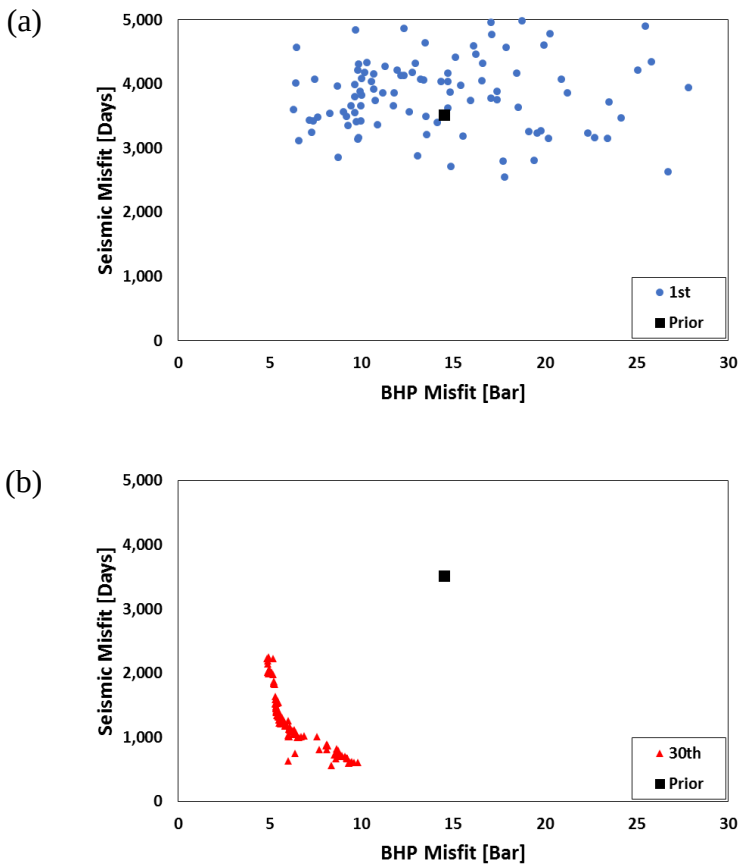

Figure 2.14 Comparison of objective functions at (a) 1st and (b) 30th generations along with the initial misfits

While an overall reduction is observed for both the seismic data and the BHP, the trade-off between the objectives is clearly shown at the Pareto-fronts (Figure 2.14(b)). By

applying a cluster analysis, we further investigate the objective function space as shown in Figure 2.15. Cluster 1 has more weight on matching seismic data, cluster 3 does on matching pressure data, and cluster 2 is an intermediate.

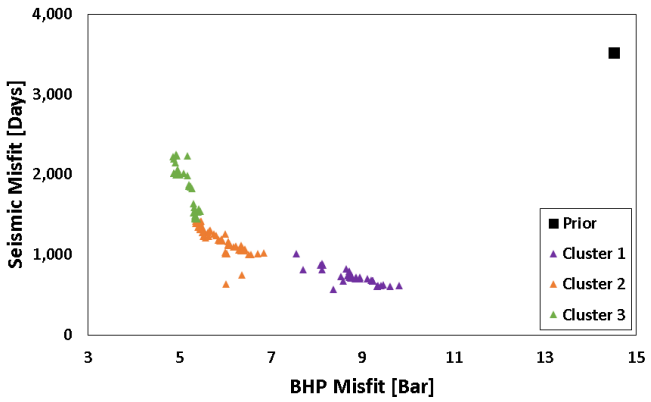

Figure 2.15 Clustered populations at 30th generation

Figure 2.16 shows the updated onset time maps of selected models for each cluster, respectively. For every clusters, we have observed a notable improvement from the initial onset time map calculated using the prior model. As expected, however, cluster 1 has the most similar shape of onset time map with the observed one, since it has more weight on matching seismic data.

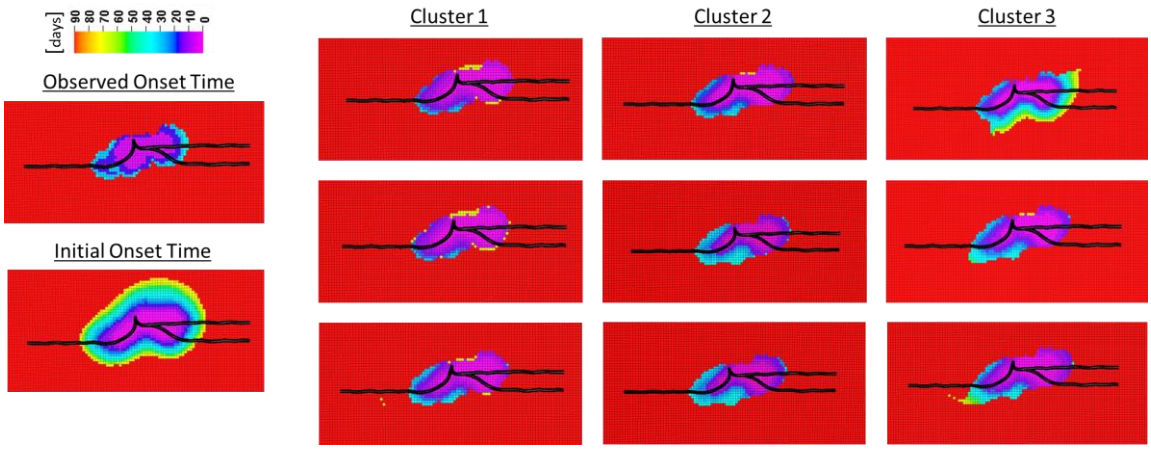

Figure 2.16 Onset time maps for selected models for each cluster

In Figure 2.17, we plot the pressure responses at the 30th generation, represented by different colors for each cluster, over the entire CSS cycle. There is marked improvement in the match quality. One notable feature is the consistent pressure match to the soak part (validation), where we used the history matched models to predict the pressure behavior indicating that the models are able to adequately represent the saturation propagation in the reservoir. As expected again, cluster 3 has the best pressure matches with the observed data, since it has more weight on matching pressure data.

(a)

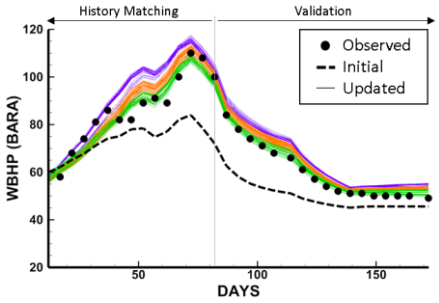

(b)

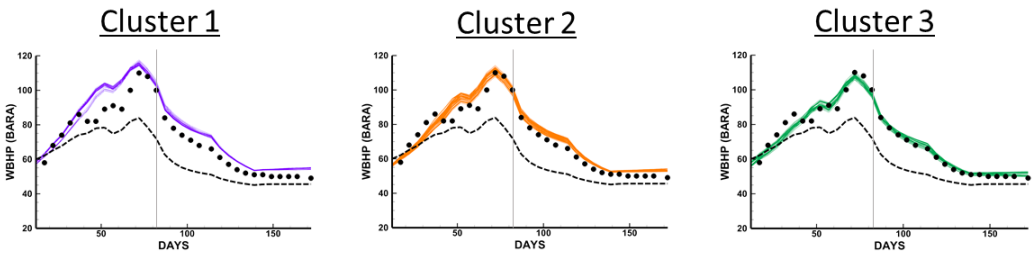

Figure 2.17 Updated BHP responses for each cluster. (a) All responses. (b) Respective responses for each cluster

Water saturation changes after 45 days and 85 days are shown in Figure 2.18. There has not been much difference in water saturation changes after 45 days for the initial model and calibrated models. However, after 85 days which is the end of steam injection period, water saturation increase is confined to a smaller region than that of the initial model. It means that the reservoir needs to be less softened compared to the initial model, resulting in a more concentrated onset time maps as seen in the observed data.

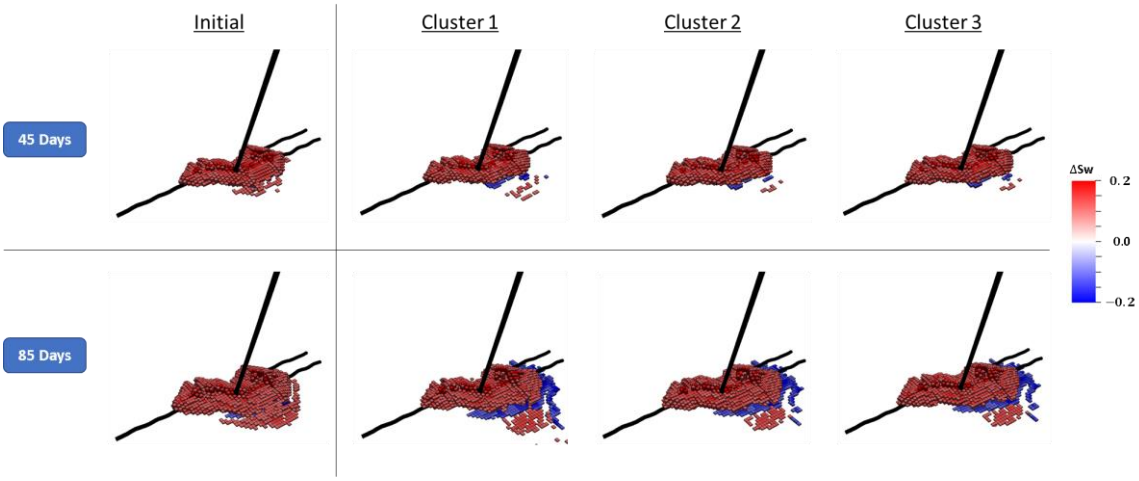

Figure 2.18 Water saturation changes after 45 days and 85 days after model calibration

Overall our history matching workflow significantly reduced the misfit associated with 4D seismic and pressure data and provided an improved representation of reservoir sweep through identification of fluid saturation distribution.

2.5. Conclusions

In this chapter, we have proposed a novel approach to integrate frequent time lapse seismic data into high resolution reservoir models based on the seismic onset times. The ABT parameterization is used to simultaneously reconcile the model heterogeneity by compressing multiple seismic surveys into a single map of onset times that represents the propagation of changes in the reservoir. Some of the conclusions from this study are the following:

- We propose a novel and computationally efficient approach for time lapse seismic integration using the onset time which is able to efficiently display the front propagation in order to update the flow properties.
- The onset time leads to a significant data reduction and provides practical and faster approach that allows testing alternative dynamic realizations, making the algorithm suitable for large field applications with frequent seismic surveys.
- The parameterization with prior information (ABT) has been demonstrated in a synthetic case compared with GCT and effectively applied to a field case.
- The Peace River application demonstrates the feasibility and the robustness of the history matching workflow (MOGA with ABT) to integrate onset times and pressure data. Unlike the manual history matching (Przybysz-Jarnut et al. 2016), our approach updates the parameters simultaneously, which allows testing different combinations of parameters uncertainty range. The compression of the frequent seismic surveys into a single set of onsets assists efficient history matching using the population-based technique that requires a large number of simulation runs. With this technique we were able to identify the injectivity profile along the horizontal well, which was crucial for further development considerations.

3. MULTI-RESOLUTION GRID CONNECTIVITY-BASED TRANSFORM FOR EFFICIENT HISTORY MATCHING OF CONVENTIONAL AND UNCONVENTIONAL RESERVOIRS[3]

3.1. Chapter Summary

Proper characterization of heterogeneous rock properties and hydraulic fracture parameters is essential for optimizing field development and reliable estimation of EUR in conventional and unconventional reservoirs. High resolution characterization of matrix properties and complex fracture parameters requires efficient history matching of well production and pressure response. We propose a novel reservoir model parameterization method to reduce the number of unknowns, regularize the ill-posed problem, and enhance the efficiency of history matching of conventional and unconventional reservoirs.

Our proposed method makes a low rank approximation of the spatial distribution of reservoir properties taking into account the varying model resolution of the rock and fracture properties. In a conventional waterflooded reservoir, we have more information on the flooded region between injectors and producers. Therefore, it enables a higher resolution model descriptions. Typically in an unconventional reservoir, hydraulic fractures are represented with much higher resolution through local grid refinements compared to the matrix properties. In our approach, the spatial property distribution of

[3] Part of this chapter is from URTeC 2019 Paper 2019-982 "Multi-Resolution Grid Connectivity-Based Transform for Efficient History Matching of Unconventional Reservoirs" by Hyunmin Kim, Feyi Olalotiti-Lawal, Akhil Datta-Gupta, and is reprinted here by permission of the Unconventional Resources Technology Conference, whose permission is required for further use.

both for matrix and fractures is represented using a few parameters via a linear transformation with multi-resolution basis functions. The parameters in transform domain are then updated during model calibrations, substantially reducing the number of unknowns. The multi-resolution basis functions are constructed by eigen-decomposition of an adaptively coarsened grid Laplacian corresponding to the data resolution. High property resolution at the area of interest through the adaptive resolution control while keeping the original grid structure improves quality of history matching, reduces simulation runtime, and improves the efficiency of history matching.

We demonstrate the power and efficacy of our method using synthetic and field examples. First, we illustrate the effectiveness of the proposed multi-resolution parameterization by comparing it with traditional method. It is shown in a conventional waterflooded reservoir that the proposed parameterization method outperforms the conventional parameterization method based on history matching quality. For the field application, an unconventional tight oil reservoir model with a multi-stage hydraulic fractured well is calibrated using bottom-hole pressure and water cut history data. The hydraulic fractures as well as the stimulated reservoir volume (SRV) near the well are represented with higher grid resolution. In addition to matrix and fracture properties, the extent of the SRV and hydraulic fractures are also adjusted through history matching using a Multi-Objective Genetic Algorithm (MOGA). The calibrated ensemble of models are used to obtain bounds of production forecast.

Our proposed method is designed to calibrate reservoir and fracture properties with higher resolution in regions that have improved data resolution and higher sensitivity to

the well performance data, for example flooded region in conventional reservoirs and the SRV region and the hydraulic fractures in unconventional reservoirs. This leads to a fast and efficient history matching workflow and enables us to make optimal development/completion plans in a reasonable time frame.

3.2. Introduction

Proper characterization of the heterogeneous rock properties is essential for optimizing field development plan and reliable estimation of EUR in conventional and unconventional reservoirs. It is critical to understand the rock properties in conventional reservoirs which are calibrated through history matching. In unconventional reservoirs, we also need to calibrate fracture parameters that significantly affect well production and pressure response. The history matching of high resolution geologic models poses an underdetermined inverse problem because of the large number of reservoir properties defined on grid cells with limited measured data. Therefore, the solution of the inverse problem related to identification of geologic heterogeneity is non-unique and potentially unstable.

The essence of regularization is to address the non-uniqueness and stability issues by either reducing the number of parameters or imposing additional constraints to ensure that the inverse problem is more tractable (Tikhonov 1977, Tarantola 2005, Tonkin and Doherty 2009). In this chapter, parameterization is used to reduce the number of unknowns, from pixel-based reservoir properties to a low rank approximation of spatial

properties, with little loss of information. This results in more stable solutions and improved predictive capability of history matched reservoir models.

Of the variety of parameterization methods, the linear transformation of spatial properties in grid cells to parameters in the transform domain has been widely used in hydrology and petroleum engineering (LaVenue and Pickens 1992, Chavent and Bissell 1998, Grimstad et al. 2003, Alcolea, Carrera, and Medina 2006, Jafarpour and McLaughlin 2009, Bhark, Jafarpour, and Datta-Gupta 2011, Bhark, Jafarpour, and Datta-Gupta 2011, Bhark et al. 2011, Hetz, Kim, et al. 2017). It is represented by equation (3.1).

$$u = \Phi v \tag{3.1}$$

where v is a m-component column vector of parameters in transform domain, and Φ is a predefined $n \times m$ matrix with columns of interpolation or transformation basis vectors. n is the number of grid cells in a model. Therefore, the updated model is determined by linear combination of basis vectors weighted by v.

The most basic parameterization with linear transformation is segmentation of geologic models into zones of piecewise continuous value. The reservoir property itself or property multiplier is updated by a constant value within each zone (Jahns 1966, Kang et al. 2015, Olalotiti-Lawal et al. 2017). In case of segmentation, Φ consists of basis vectors of which elements are non-zero constant values only for the corresponding zones and zero for the other zones. Φ should be predefined based on the prior model and does not change in the course of model calibrations. The other common parameterization is Karhunen-Loève transform (KLT) or principal component analysis (PCA) of the property covariance matrix (Karhunen 1947, Loève 1978, Reynolds et al. 1996). The eigenvectors of the

covariance matrix are ranked by their corresponding eigenvalues, from largest to smallest, and several eigenvectors with the largest eigenvalues compose the transform basis. In this approach, the basis vectors provide optimal compression if the covariance matrix accurately captures the model geostatistical features. In other words, basis vectors obtained by the KLT approach tend to capture the details of spatial heterogeneity with the fewest transform parameters and result in minimum mean square error for the low rank approximation. Similar to the model segmentation, underdetermined inverse problems can be regularized by reducing the number of unknowns from pixel-based property field to a low rank approximation with little loss of information. However, Jafarpour and McLaughlin (2009) and Bhark, Jafarpour, and Datta-Gupta (2011) discussed the limitations of KLT in a realistic history matching problem of high resolution models: (1) the covariance is generally unknown, resulting in the possibility of suboptimal basis functions if prior model is incorrect, (2) it often entails an eigen-decomposition of large covariance matrices which can be prohibitively expensive.

To overcome these limitations, there have been studies conducted on model-independent parameterization in image processing (Jain 1989, Gonzalez 2001, Rao and Yip 2014). They used the discrete cosine transform (DCT) which is a type of Fourier transform that reconstructs a discrete signal as the sum of cosine harmonics (Britanak, Yip, and Rao 2010). Jafarpour and McLaughlin (2009) applied DCT in reservoir characterization, and Bhark, Jafarpour, and Datta-Gupta (2011) further developed it to the multiscale history matching workflow. The matrix Φ in equation (3.1) of DCT also refers to a linear transformation matrix of which columns are cosine function with corresponding

frequency that depicts a harmonic pattern of grid. As each cosine function is calculated based not on the properties in grid cells, but on the grid structure, basis vectors are constructed independent of the prior model. Each transform parameter in **v** is merely the amplitude of each cosine function. Therefore, DCT basis vectors are calculated analytically only once with cosine functions for a given inverse problem, and considerably smaller parameter set (v) updates the prior model during calibrations. This parameter reduction is possible because DCT has a strong compression performance, so it is able to capture larger scales of spatial continuity and heterogeneity with a significantly reduced number of parameters. In addition, mapping transform parameter to spatial property is achieved simply by the transpose of basis vectors due to their pairwise orthonormality. However, to calculate DCT transformation matrix, the grid cells should be rectangular and of uniform thickness in certain orientation to satisfy the underlying assumption of periodicity (Bhark, Datta-Gupta, and Jafarpour 2011, Bhark, Jafarpour, and Datta-Gupta 2011). Bhark, Jafarpour, and Datta-Gupta (2011) developed the grid connectivity-based transform (GCT) as a generalization of the DCT basis for generic grid geometries. The GCT basis vectors are defined as the eigenvectors of a Laplacian matrix that has two-point grid connectivity information, so they depend solely on the grid structure independent of grid properties. In the case of a regular periodic and fully connected grid, the GCT basis vectors are same as those of DCT in either structured or unstructured grid geometry.

The limitation of GCT is that the resolution within each basis vector is forced to follow the grid cell resolution because its underlying periodicity calculation is solely based on the grid connectivity, not on the grid cell size and shape (Bhark et al. 2011). The

geologic model should be reconciled in accordance with multi-resolution static and dynamic data, for which resolution can vary from regional to the grid-cell scale. There have been studies on the structured data integration algorithms that are each suited to the scale of the estimated properties and the type and resolution of available data (Landa and Horne 1997, Cheng, Dehghani, and Billiter 2008, Kim et al. 2014, Kam, Han, and Datta-Gupta 2017, Park et al. 2019, Park and Janova 2019). Bhark, Jafarpour, and Datta-Gupta (2011) and Bhark, Jafarpour, and Datta-Gupta (2011) suggested an adaptive multiscale inversion workflow with DCT and GCT to balance parameter resolution with data resolution, that is, the low rank property descriptions are updated and successively refined to the spatial scale beyond which the available data do not support further refinement. If there is a region with higher data resolution in a reservoir, considered as an area of interest (AOI), it is required to include more basis vectors to achieve corresponding spatial resolution of heterogeneity, although the data resolution outside AOI is limited to a coarser scale. It masks the regularization effect by requiring more basis vectors, which are necessary for AOI but redundant for the region outside AOI.

In this chapter, we propose a multi-resolution parameterization method to enhance the regularization when data resolution is variant in a reservoir (Kim, Olalotiti-Lawal, and Datta-Gupta 2019). In our approach, for each basis vector, frequency in the AOI is higher than the coarsened regions. Multi-resolution grid connectivity-based transform (MGCT) requires smaller parameter set (less basis vectors) than GCT to have the same adaptive ability to detect and characterize local and global spatial features at different resolutions. In other words, MGCT has better capability of integrating multi-resolution data into a

geologic model given the same number of parameters. The history matching workflow starts with the establishment of AOI based on the type and location of measured data. By coarsening the regions outside AOI, MGCT basis is constructed by spectral analysis of the locally refined grid connectivity information. Using multi-resolution basis vector set, reservoir property field is transformed from spatial domain to spectral domain, and vice versa during model calibrations. It enables adaptive updates of reservoir heterogeneity that are amenable to variant data resolutions.

In the following sections, the multi-resolution GCT parameterization method is explained in detail, mainly in comparison with GCT. The implementations and analyses of re-parameterization, which is a low rank approximation, are demonstrated with a synthetic case. We further compare MGCT with GCT through history matching exercise of the widely used SPE Brugge benchmark case, where measured data are concentrated in specific regions. The inversion problem is solved by one of powerful gradient-free methods, Pareto-based multi-objective genetic algorithm to eliminate potential conflicts between objective functions (Park, Datta-Gupta, and King 2015). After demonstrating improved performance, MGCT is applied to an unconventional tight oil reservoir with multi-stage hydraulic fractures for which AOI is the stimulated reservoir volume (SRV) near the well.

3.3. Background and Methodology

The proposed history matching method follows a gradient-free inversion process with reservoir property parameterization as depicted in Figure 3.1. First, transformation basis functions are constructed as the eigenvectors of a multi-resolution grid Laplacian, followed by Pareto-based multi-objective genetic algorithm. Initial population in low-dimensional transform domain are generated, with which reservoir properties in high-dimensional spatial domain are calculated using predefined basis functions. Simulations are run with these properties and we calculate objective functions, which are the data misfits for history matching. Through selection, crossover, mutation, non-dominated sorting and ranking algorithms (Deb and Pratap 2002), we will have new populations and repeat this process until the solution is converged or the maximum generation is reached. The detailed backgrounds and methodologies will be explained in the following subsections.

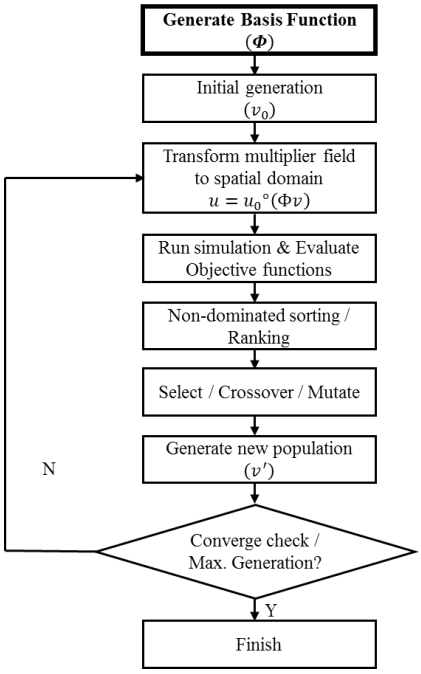

Figure 3.1 Workflow of history matching with multi-resolution parameterization and multi-objective genetic algorithm

3.3.1. Grid Connectivity-Based Transform (GCT)

The GCT is a generalization of the DCT basis for generic grid geometries, which is a Fourier-based transform designed for signal decorrelation (Britanak, Yip, and Rao 2010). With the analytic form of cosine functions as an example for two-dimensional $N_x \times N_y$ -grid cell property in equation (3.2), DCT basis is easily calculated and commonly used for data compression (Gonzalez 2001).

$$v(r,s) = \alpha(r)\alpha(s)\sum_{x=0}^{N_x-1}\sum_{y=0}^{N_y-1} u(x,y)\cos\left[\frac{(2x+1)r\pi}{2N_x}\right]\cos\left[\frac{(2y+1)s\pi}{2N_y}\right] \qquad (3.2)$$

where $u(x,y)$ is a spatial parameter, $v(r,s)$ is a parameterized coefficient in a spectral domain, and $\alpha(r=0)=\sqrt{\frac{1}{N_x}}$, $\alpha(r\neq 0)=\sqrt{\frac{2}{N_x}}$, $\alpha(s=0)=\sqrt{\frac{1}{N_y}}$, $\alpha(s\neq 0)=\sqrt{\frac{2}{N_y}}$ for $r=0,\ 1,\ 2,\ \cdots,\ N_x-1$, and $s=0,\ 1,\ 2,\ \cdots,\ N_y-1$. As in its multiplication form of two separate cosine functions for two-dimensional property, the DCT can be extended to three-dimensional case with multiplying the other cosine function. Jafarpour and McLaughlin (2009) applied DCT to characterize and update the prior model with a low-rank approximation that captures important large scale heterogeneity with significantly reduced number of parameters, resulting in a regularized history matching problem. Bhark, Jafarpour, and Datta-Gupta (2011) generalized DCT to arbitrary grid geometry by GCT, of which basis functions are defined as a set of the grid Laplacian eigenvectors. Strang (1999) showed that DCT basis can be derived as the eigenvectors of symmetric second difference matrix. Bhark, Jafarpour, and Datta-Gupta (2011) demonstrated that grid Laplacian is a discrete second difference operator when applied to a function on the grid with Neumann boundary condition. For one-dimensional grid example, function u_j is defined on grid j, shown in Figure 3.2(a). Second differences for interior grid cell $j=[2,N-1]$ are calculated as $L(j,\bullet)=(u_{j+1}-u_j)-(u_j-u_{j-1})=-(-u_{j-1}+2u_j-u_{j+1})$. Therefore, all the rows except top and bottom rows have the same form $[-1\ \ 2\ \ -1]$ as in Figure 3.2(b). For the boundary grid cell $j=1,\ N$, Neumann's zero derivative condition is applied. The second difference at the left boundary is $L(1,\bullet)=-u_0+2u_1-u_2=-u_1+2u_1-u_2=u_1-u_2$, because $u'_{1/2}=0\ \Rightarrow\ u_0=u_1$. Similarly at

the right boundary, the second difference is $L(N,\bullet) = -u_{N-1} + 2u_N - u_{N+1} = -u_{N-1} + 2u_N - u_N = -u_{N-1} + u_N$, because $u'_{N+1/2} = 0 \Rightarrow u_{N+1} = u_N$. The second difference matrix for one-dimensional grid is now completed as in Figure 3.2(b) and its eigenvectors are same as DCT basis vectors (Strang 1999).

(a)

(b)

$$Lu = \begin{bmatrix} 1 & -1 & & & & \\ -1 & 2 & -1 & & & \\ & & \ddots & & & \\ & & -1 & 2 & -1 & \\ & & & -1 & 1 & \end{bmatrix} \begin{bmatrix} u_1 \\ u_2 \\ \vdots \\ u_{N-1} \\ u_N \end{bmatrix}$$

Figure 3.2 (a) 1D uniformly structured grid and extended edges to explain the Neumann boundary condition and (b) corresponding symmetric second difference matrix

The grid Laplacian is constructed as in equation (3.3) (Mohar 1997, Sorkine 2006, Von Luxburg 2006).

$$L_{i,j} = \begin{cases} d_i & i = j \\ -1 & (i,j) \in E \\ 0 & otherwise \end{cases} \tag{3.3}$$

where i and j are grid cell indices from 1 to N, E is the two-point edge set of grid cells i and j, and d_i is the degree of a cell which is equivalent to the total number of grid cells connected to grid i. Equation (3.3) is equivalent to the second difference matrix constructed in Figure 3.2(b), therefore, the grid Laplacian eigenvectors are also DCT basis vectors (Bhark, Jafarpour, and Datta-Gupta 2011). Another practical form of grid Laplacian is equation (3.4).

$$L = D - A \tag{3.4}$$

where A is the $N \times N$ grid adjacency matrix, where N is the total number of grids in a reservoir model. The entries of A are given by grid connectivity between two grid cells, that is, unity if neighbored and zero otherwise as in equation (3.5).

$$a_{i,j} = \begin{cases} 1 & if\ neighbored \\ 0 & otherwise \end{cases} \tag{3.5}$$

D is the $N \times N$ diagonal matrix, known as degree matrix, whose entries are row sums of A as in equation (3.6).

$$d_i = \sum_{j=1}^{N} a_{i,j} \tag{3.6}$$

Therefore, we can construct the grid Laplacian only using grid connectivity information for any grid system. From the construction rule of grid Laplacian, it is always sparse and real symmetric, of which eigen-decomposition is

$$L = V \Lambda V^T = \sum_{i=1}^{N} \lambda_i v_i v_i^T \tag{3.7}$$

where V is an $N \times N$ matrix with columns as eigenvectors, and Λ is the $N \times N$ diagonal matrix of the real eigenvalues λ. As L is real symmetric, it is positive semidefinite, resulting in N nonnegative real eigenvalues with spectrum $0 \le \lambda_i \le \cdots \le \lambda_N$, where i is the spectral index. The eigenvector of lower modal frequency has a lower eigenvalue. For the low rank approximation of spatial properties, only a small number of leading eigenvectors are used, from the lowest frequency to higher. Therefore, full eigen-decomposition of a Laplacian is not required, but we only need to carry out a partial decomposition to calculate eigenvectors with small eigenvalues. Utilizing a sparse form of Laplacian, the partial decomposition is efficiently performed by the Arnoldi Package (ARPACK) subroutines (Lehoucq, Sorensen, and Yang 1998). For given grid geometry and structure, the grid Laplacian is constructed, followed by a partial eigen-decomposition to calculate the basis vectors with low frequency, that represent large scale heterogeneity. Any spatial property can be projected onto the selected low frequency basis vectors, and corresponding spectral coefficients are updated during history matching, resulting in large scale property updates. In addition, the eigenvectors in equation (3.7) are pairwise orthonormal, linear transforms and inverse transforms are conducted in an efficient way in equation (3.8).

$$v = \Phi^T u \quad \Leftrightarrow \quad u = \Phi v \tag{3.8}$$

where u is a n-component column vector of a spatial parameter set, same as the number of grid cells, and v is a m-component column vector of a spectral parameter in a transform domain, much smaller than n for re-parameterization to regularize the inverse

problems. Φ is the $n \times m$ linear transform matrix of which columns are the selected low frequency GCT basis vectors.

For example, Figure 3.3 shows twenty leading basis vectors of 50×50 grid system. As constructed entirely by grid structure and geometry, specifically by the grid connectivity, these are independent of reservoir property. Each of these has constant resolution over the entire grid system, because the grid cell size and shape are constant in this case. In case of variant grid cell sizes, the grid Laplacian contains information related not to cell size, but only to connectivity (Bhark et al. 2011).

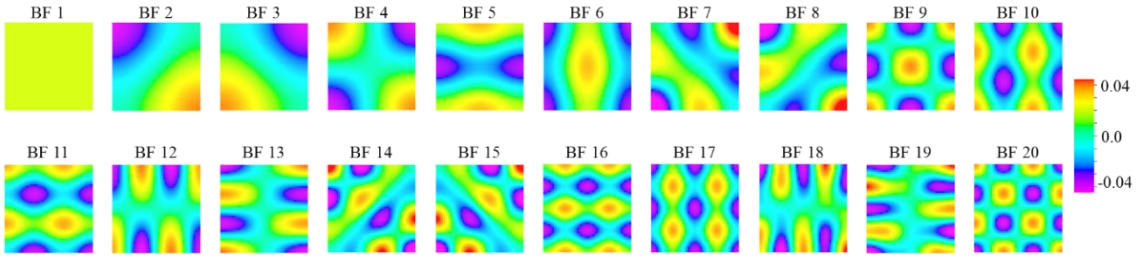

Figure 3.3 Low frequency GCT basis functions of 50×50 grid system

3.3.2. Multi-Resolution Grid Connectivity-Based Transform (MGCT)

As mentioned in the introduction, the resolution in each GCT basis function follow the grid cell resolution, because grid Laplacian is constructed only from the grid connectivity, not from the grid cell size and shape. History matching problems often entail reconciliation of multi-resolution static and dynamic data. Basis functions that have multiple resolutions

corresponding to the measured data better regularize the history matching problem than GCT.

We suggest a novel multi-resolution parameterization method, multi-resolution grid connectivity-based transform (MGCT), by coarsening the region that has low data resolution, outside the AOI. Merging grid cells into a smaller number of grid cells makes the grid size larger, therefore, it lowers basis function frequency in the coarsened area and AOI gets a benefit of higher frequency. Figure 3.4 shows a comparison of grid Laplacian constructions by GCT and MGCT, where AOI is the center region assumed to have higher data resolution. GCT has 36×36 Laplacian matrix in Figure 3.4(a), where the integer values implying grid connectivity and the degree of each grid cell are shown as each color. By coarsening the region outside AOI with 2×2 scheme, MGCT has much smaller 12×12 Laplacian, despite a little less sparsity caused by the new connections between coarsened grid and neighboring fine grid cells. Due to significantly reduced size, MGCT requires less computation load on the eigen-decomposition even with larger off-diagonal elements ratio (less sparsity). By this formulation, basis functions in AOI will have higher resolutions without changing grid cell geometry than those of GCT.

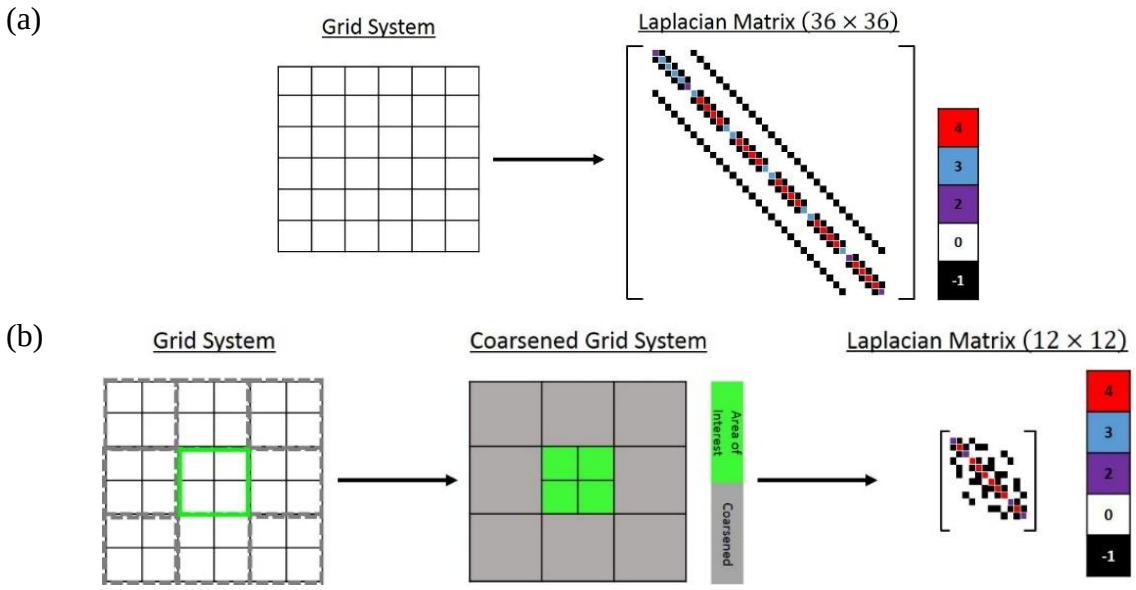

Figure 3.4 (a) Grid Laplacian for GCT and (b) coarsened grid Laplacian for MGCT

For the example of the same grid geometry as Figure 3.3, MGCT shows the twenty leading basis vectors with AOI located at the center (I-direction: 16 – 35, J-direction: 16 – 35) and the peripheral area is coarsened with 5×5 scheme as in Figure 3.5. Except for the constant basis function (BF1) with zero eigenvalue, MGCT always has higher frequencies in AOI than GCT. This feature makes MGCT have a better capability of integrating multi-resolution data into a geologic model, given the same degree of freedom.

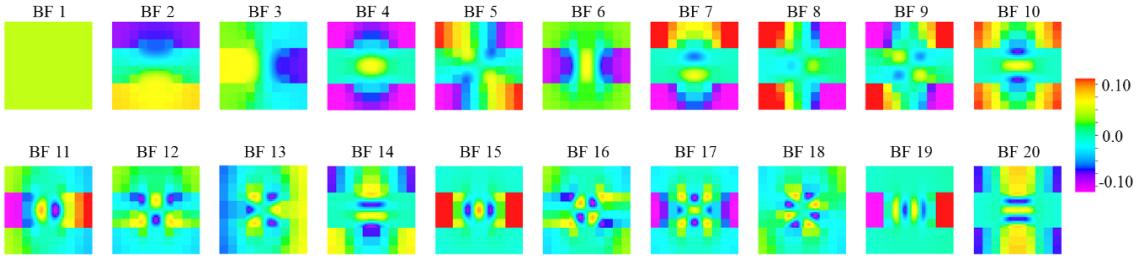

Figure 3.5 Low frequency MGCT basis functions of 50×50 grid system

MGCT Laplacian should also be a symmetric second difference matrix, in order for its eigenvectors to be DCT basis vectors. In Figure 3.6, u_j is a function defined on the coarsened grid, with $C_x \times C_y$ coarsening scheme. $u_{j,i}^{E,W,N,S}$ are functions defined on the i^{th} neighboring fine grids located on (E,W,N,S) edges.

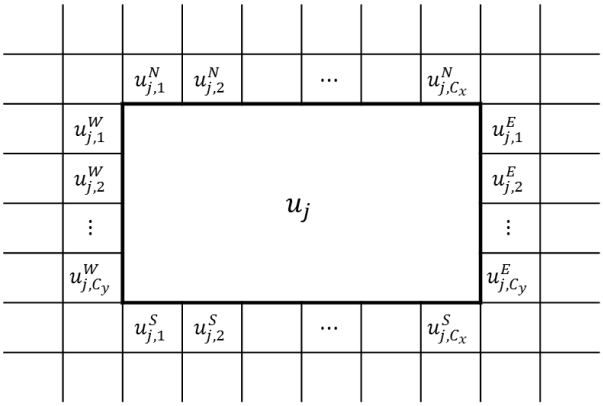

Figure 3.6 Coarsened grid and neighboring fine grids

In the horizontal direction, discrete second difference is calculated as in equation (3.9), and the one in the vertical direction as equation (3.10).

$$\begin{aligned}&\left(u_{j,1}^{W}-2u_j+u_{j,1}^{E}\right)+\left(u_{j,2}^{W}-2u_j+u_{j,2}^{E}\right)+\cdots+\left(u_{j,C_y}^{W}-2u_j+u_{j,C_y}^{E}\right)\\&=-\sum_{i=1}^{C_y}\left(-u_{j,i}^{W}+2u_j-u_{j,i}^{E}\right)\end{aligned} \tag{3.9}$$

$$\begin{aligned}&\left(u_{j,1}^{N}-2u_j+u_{j,1}^{S}\right)+\left(u_{j,2}^{N}-2u_j+u_{j,2}^{S}\right)+\cdots+\left(u_{j,C_y}^{N}-2u_j+u_{j,C_y}^{S}\right)\\&=-\sum_{i=1}^{C_x}\left(-u_{j,i}^{N}+2u_j-u_{j,i}^{S}\right)\end{aligned} \tag{3.10}$$

Finally, the second difference matrix with $\left(C_x\times C_y\right)$-coarsened grid cell will have the form as in equation (3.11) which is equivalent with the two-point grid connectivity of grid Laplacian. The coarsened grid u_j has a coefficient as the total number of neighbored fine grid cells, each of which has the coefficient of -1 implying two-point grid connectivity. The coarsened grid Laplacian can be easily extended to three-dimension with inclusions of neighboring grids on top and bottom edges and generalized to any coarsening scheme with the corresponding grid connectivity information.

$$-\left[2\left(C_x+C_y\right)u_j+\sum_{i=1}^{C_y}\left(-u_{j,i}^{W}-u_{j,i}^{E}\right)+\sum_{i=1}^{C_x}\left(-u_{j,i}^{N}-u_{j,i}^{S}\right)\right]\Leftrightarrow L_{i,j}=\begin{cases}d_i & i=j\\-1 & (i,j)\in E\\0 & else\end{cases} \tag{3.11}$$

As in the GCT, MGCT basis vectors are calculated solely dependent on grid structure and geometry, so model independent, however, its frequencies can be adjusted by a coarsening scheme. As a simple example, we show how frequencies of basis vectors in AOI are changing in one-dimensional grid system, according to different coarsening schemes in Figure 3.7. The AOI is the yellow area $[0,\ 4]$, and the other region is

coarsened with 1×1(no coarsen), 2×1, 3×1, and 4×1 each. The one-dimensional DCT basis functions in equation (3.12) are compared for each grid system as in Figure 3.7(b).

$$\Phi(r)=\alpha(r)\cos\left[\frac{(2x+1)r\pi}{2N_x}\right] \tag{3.12}$$

(a)

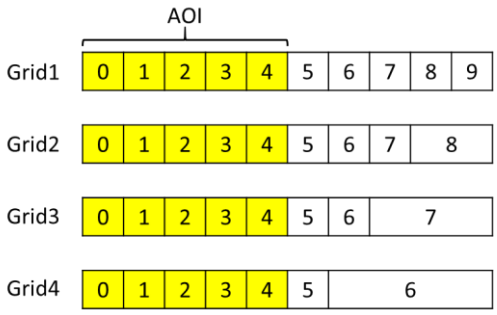

(b)

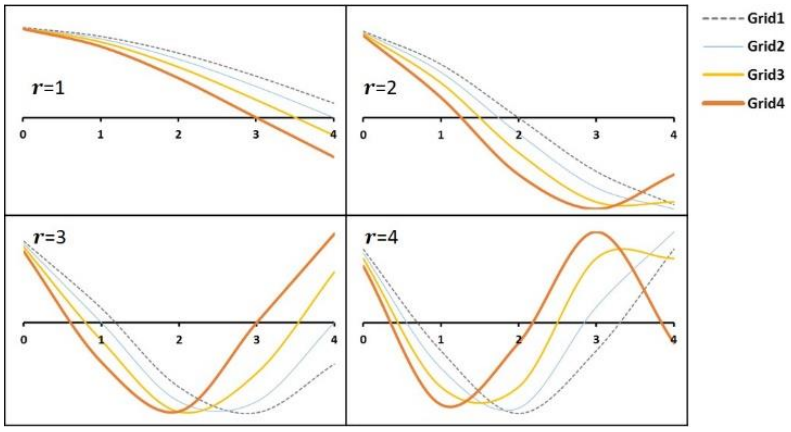

Figure 3.7 (a) Various coarsening schemes and (b) corresponding DCT basis functions in AOI

In each modal frequency, from the lowest to higher modes ($r = 1, 2, 3, 4$), the more aggressive coarsening scheme results in higher frequency of basis function in the AOI. It is caused by that total number of grids (N_x), which is decreased by grid coarsening. Therefore, frequency of cosine function, $(2x+1)r / 2N_x$, becomes higher given an order of basis function (r). In this manner, we are able to adaptively change the resolutions within each MGCT basis vectors. Coarsening the regions where data resolution is lower than in AOI, which can be also variant depending on the given data sources, MGCT controls spatial property resolutions mapped onto each basis vectors. This adaptive resolution control of MGCT is a significant benefit, considering that GCT requires an inclusion of more basis functions in order to achieve the spatial resolution comparable to the data resolution in the AOI.

3.3.3. Re-parameterization Analysis

In the course of history matching, the prior model ranges from uninformed to well informed. The basis function of model dependent parameterization, such as KLT, may not be effective and can mislead the property update when prior model is not known or incorrect. Model independent parameterizations (DCT, GCT, and MGCT) do not require prior knowledge and the basis functions are not limited by uncertain or incorrect prior assumptions. Although the basis constructions are independent of prior information, we can benefit from the prior model if it is well informed by available data sources. The benefit comes from the method to sort and select basis functions superimposed onto the prior model.

Jafarpour and McLaughlin (2009) demonstrated the method to truncate the images (re-parameterization) with a few significant coefficients when the prior model is well informed. When inverse transformed from the prior model to a set of coefficients in equation (3.13), the large coefficients are concentrated on the low frequency basis vectors. A large coefficient implies that the corresponding basis vector includes a large amount of prior information. Therefore, the leading eigenvectors, from the lowest frequency to higher, should be re-sorted to select the basis functions that provide the best approximation to a single known image.

$$v = \Phi^T u \tag{3.13}$$

We calculate the coefficients of the leading GCT basis functions shown in Figure 3.3, for the reference permeability field in Figure 3.8. Figure 3.9(a) shows the coefficients with the order of eigenvalues, from the lowest to higher (leading mode). The magnitudes of these coefficients, which are not the eigenvalues, do not decrease monotonically but fluctuate from eigenvector to eigenvector, due to the projection onto the prior model as in equation (3.13). The coefficients are then sorted in a descending order to select the basis functions with large prior information as in Figure 3.9(b). We call that these basis functions are now in a 'significant mode'. Note that the sequence of eigenvectors in a significant mode is not in a monotonic order any more. The selected twenty basis functions with the significant coefficients are shown in Figure 3.10. In summary, if the prior knowledge is uncertain or incorrect, the leading mode should be used. Otherwise, the significant mode is recommended for the selection of basis functions.

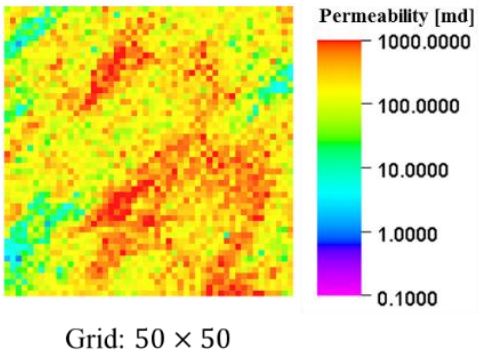

Figure 3.8 Reference permeability for re-parameterization

(a)

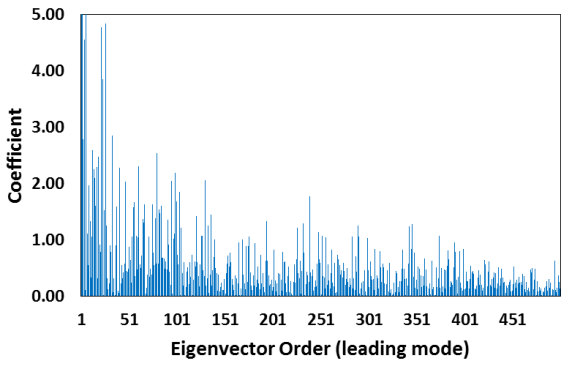

(b)

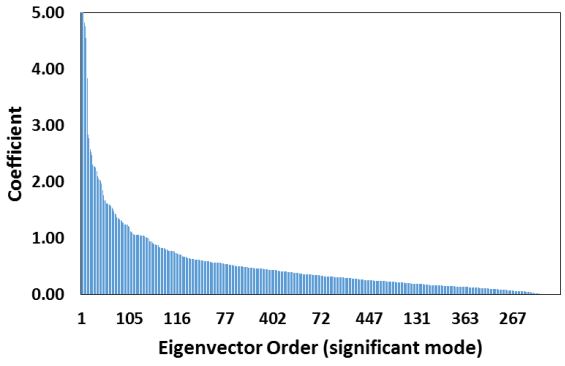

Figure 3.9 (a) Coefficients in the order of eigenvalues and (b) coefficients in the order of coefficient magnitudes

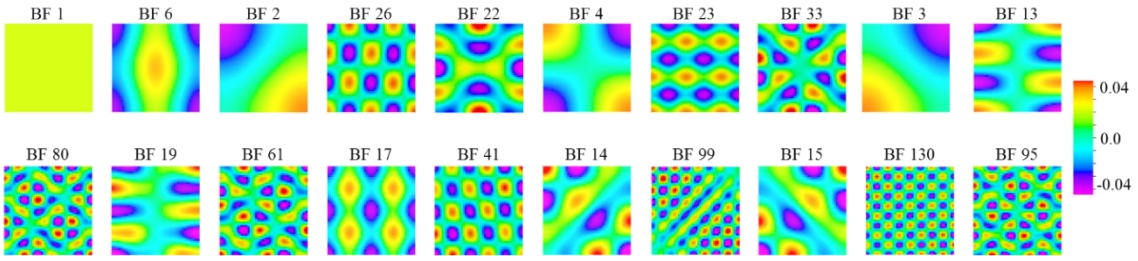

Figure 3.10 GCT basis functions of 50×50 grid system (significant mode)

To compare the compression performance of each modes, the root mean square errors (RMSE) between the reference and low rank approximation, in equation (3.14), are calculated as a function of the number of basis functions included.

$$RMSE = \frac{1}{N}\sqrt{\sum_{i=1}^{N}\left(k_i^{reference} - k_i^{approximation}\right)^2} \tag{3.14}$$

where N is the number of grid cells in the model, $k_i^{reference}$ is the reference permeability of i^{th} grid, and $k_i^{approximation}$ is the permeability value of a low rank approximation in i^{th} grid. RMSE from the significant mode is always smaller than that of the leading mode when using the same number of basis functions as shown in Figure 3.11(a), implying the higher compression performance of a significant mode than a leading mode. It should be noted that the perfect reconstruction of the reference permeability field is possible if the full rank of basis functions are used, whether it is model dependent or model independent and whether it is a leading mode or a significant mode, and that the purpose of re-parameterization (truncation) is to represent as much information as possible with a small number of coefficients. Therefore, from the RMSE point of view, the significant mode is

better than the leading mode, if the prior model is well informed. Figure 3.11(b) shows the low rank approximations with the corresponding (unsorted or sorted) basis functions, from which it is obvious that the significant mode results in a better compression performance than the leading mode, especially when smaller number of basis functions are retained.

(a)

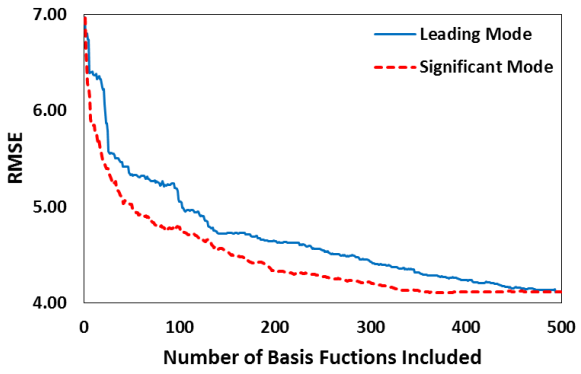

(b)

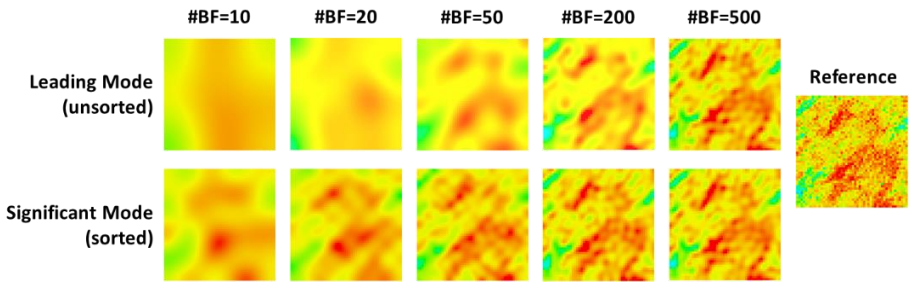

Figure 3.11 (a) Comparison of RMSE and (b) low rank approximation for each mode

The compression performances of GCT and MGCT in the AOI, defined in Figure 3.5, are compared in Figure 3.12. The basis functions for each method are selected both

in significant modes. In the AOI, assumed to have higher data resolution, MGCT always has higher compression performances than GCT as confirmed by its lower RMSE values in Figure 3.12(a). As a result of grid coarsening, the low rank approximations of MGCT have multiple resolutions as compared to a constant spatial resolution of GCT in Figure 3.12(b). This feature makes the underdetermined history matching problem more regularized by MGCT when the data resolution is variant throughout the reservoir. The re-parameterized permeability fields only in the AOI are also compared in Figure 3.12(c).

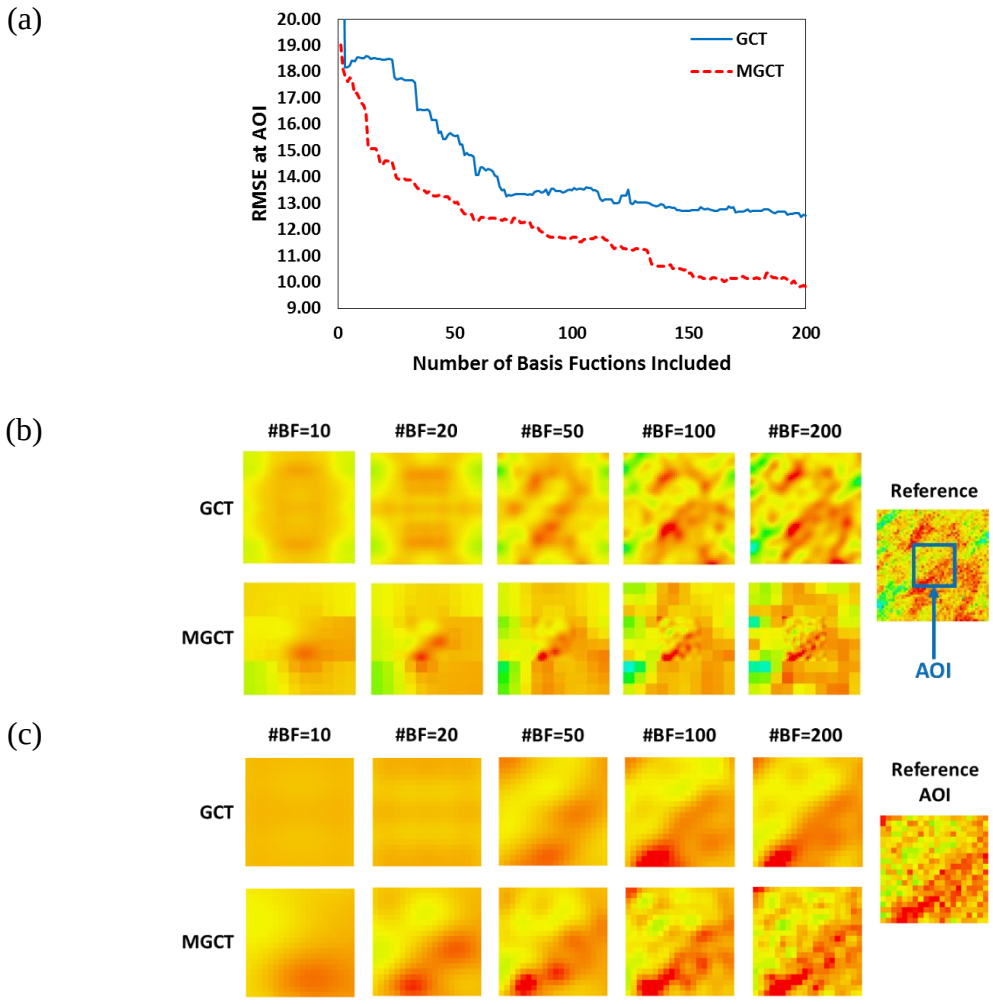

Figure 3.12 (a) Comparison of RMSE, (b) low rank approximation in entire region, and (c) low rank approximation in the AOI for GCT and MGCT

3.3.4. Multi-Objective Genetic Algorithm

In this section, we briefly review the genetic algorithm (GA) with the direct use of the dominance relation between each solutions, instead of aggregating objective functions into a scalar function. The purpose of stochastic optimization approach is to secure as diverse realizations as possible for uncertainty quantification. The GA with the aggregated

sum method, however, results in incomplete exploration of the solution space especially when the objectives are conflicting each other (Deb and Pratap 2002). The multi-objective genetic algorithm (MOGA) is designed to find a representative set of solutions in the Pareto optimal front, which displays the trade-off between multiple objectives.

Of many evolutionary algorithms, we use non-dominated sorting genetic algorithm (NSGA-II) in order to directly use the dominance relation between each member of the population (Deb and Pratap 2002, Park, Datta-Gupta, and King 2015). The major difference of NSGA-II from the classical GA with the aggregated sum methods is the selection method. Instead of fitness function, NSGA-II uses 'rank' and 'crowding distance' to select one population over the other. In each generation, the members are sorted based on the dominance relationship, which means that one member dominates the other only if all objective functions are smaller than those of the other. We first find non-dominated solutions which are not dominated by any other members, and assign the ranks as 1. The next sorted populations are ranked as 2, which are not dominated by any member except at least one of members in rank 1. In the same manner, all the members are assigned the ranks. If populations have the same ranks, the one with larger crowding distance is selected to preserve the diversity of the populations. It represents the density of solutions around certain population, calculated as in equation (3.15) and Figure 3.13. The detailed background and methodology are well described in Deb and Pratap (2002) and Park, Datta-Gupta, and King (2015).

$$\text{Crowding Distance}^i = \sum_{k=1}^{m} \frac{d_k^i}{f_k^{\max}} \tag{3.15}$$

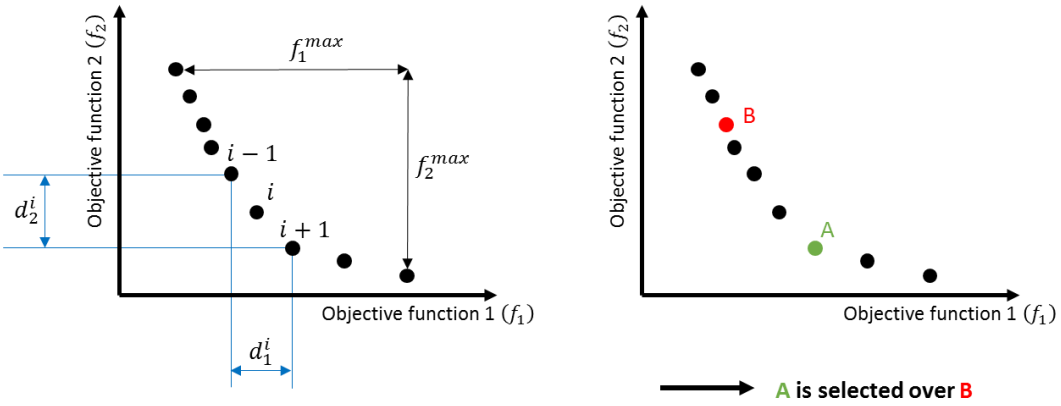

Figure 3.13 Illustration of crowding distance in dual objectives case

3.4. Application

In this section, we demonstrate the applications of our proposed approach. First, we parameterize permeability field for the Brugge reservoir model, a SPE benchmark case (Peters et al. 2010), to calibrate it to water cut and bottom-hole pressure. Both GCT and MGCT are utilized to compare the resolutions of basis functions, required computation powers, and history matching results. Second, we apply MGCT to parameterize matrix permeability in an unconventional tight oil reservoir with multi-stage hydraulic fractures, in which AOI is the region for the stimulated reservoir volume (SRV) near the well.

3.4.1. Brugge Benchmark Model

The Brugge reservoir model is a benchmark case developed by the Netherlands Organization for Applied Scientific Research (TNO) to test the combined use of waterflooding-optimization and history-matching methods in a closed-loop workflow.

The properties in the model imitate a North Sea Brent-type field within an east-west half dome. There is a single interior fault and a truncating boundary fault at the north edge. The model has 44,355 active cells in nine layers, with twenty producers at the center dome and ten peripheral water injectors in the supporting aquifer. It has ten years of history data for water production rate, oil production rate, and bottom-hole pressure at each producer. We constrain the total well liquid rates and calibrate the isotropic permeability, whose prior distribution is shown in Figure 3.14, to match water cuts and bottom-hole pressures of each well, by updating basis coefficients.

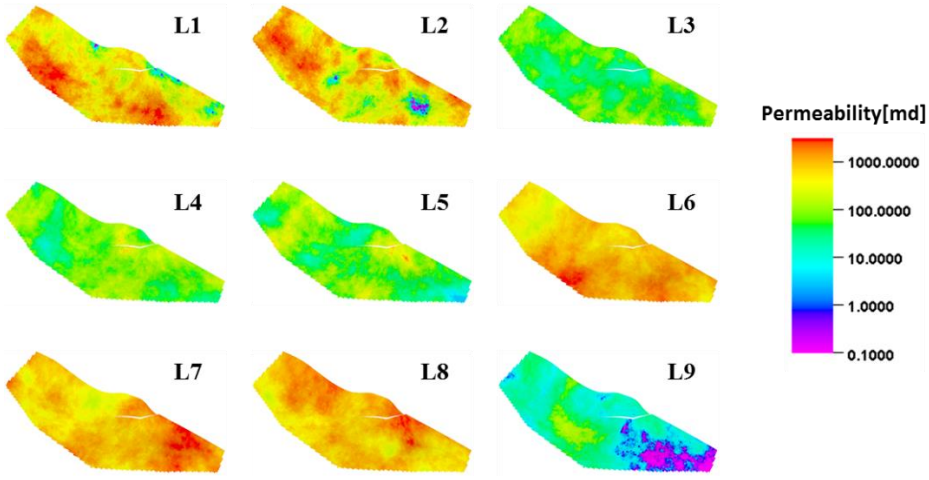

Figure 3.14 Prior permeability distribution of Brugge model for each layer

The logarithmic multiplier is parameterized as in equation (3.16), to avoid negative multiplier values and to preserve high resolution of the prior permeability field, assumed to be well informed. GCT basis functions (Φ) are not variant regardless of the grid

property, while basis coefficients (v) are dependent on the parameterized property. Therefore, any type of spatial property can be parameterized by the equation (3.16), with the same GCT basis functions. Note that ' $\circ$ ' represents an entrywise product between two vectors.

$$\log_{10}\left(multiplier\right) = \Phi v \;\Rightarrow\; k = k_0 \circ \left(10^{\Phi v}\right) \tag{3.16}$$

3.4.1.1. Comparison of Re-parameterization

In order to benefit from the well informed prior model, GCT basis functions are sorted by their coefficients projected to prior permeability distribution as shown in Figure 3.15(a). That is, we are to use the basis functions that have the most similar spatial trends to the prior model in a significant mode. The corresponding RMSE is shown in Figure 3.15(b). It should be noted that there is a tradeoff between model calibration performance and the spatial property resolution from the parameterization. Improving the resolution of the property update via the inclusion of more basis functions deteriorates the regularization by increasing the parameter set size in underdetermined inversion problems. Therefore, we need to decide the optimal number of basis functions to include as much spatial information as possible with the fewest basis coefficients. In the Brugge case, thirty basis functions are selected as indicated by red dotted lines in Figure 3.15(a) and (b). The improvement of spatial heterogeneity information is negligible with further increasing the parameter set. The selected GCT basis functions are shown in Figure 3.16. The modal shapes reflected by basis functions and their resolutions follow the grid structure and geometry, honoring the discontinuity across the interior fault.

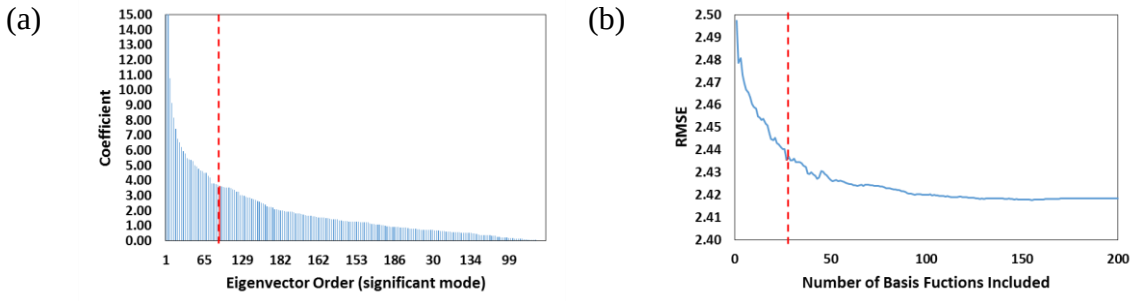

Figure 3.15 (a) Sorted coefficients in a significant mode and (b) corresponding RMSE of GCT in Brugge

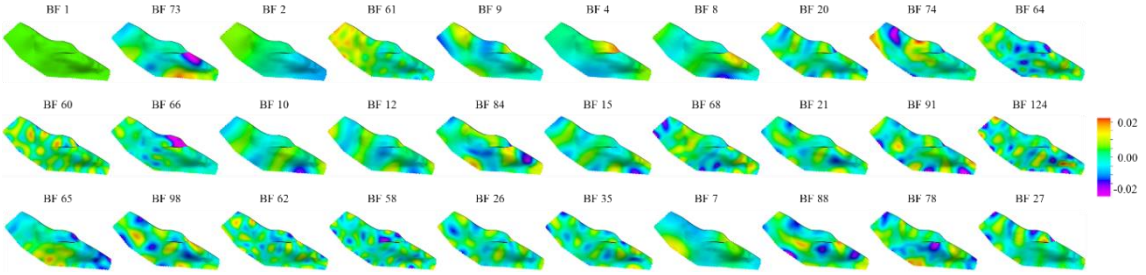

Figure 3.16 GCT basis functions selected for model calibration of Brugge model

In order to employ MGCT, we need to set an appropriate AOI where the data resolution is higher than the other regions. The main production mechanism in the Brugge case is waterflooding from the peripheral water injectors to the oil producers at the center of the dome. It is evident that the history data measured at each well would facilitate the reservoir property calibration around them to the finer scale than the other regions. Obviously, the region of high fluid saturation changes through production is more influential to both history data and simulation results. Based on the well distributions and the initial water saturation shown in Figure 3.17(a), the AOI is set as in Figure 3.17(b).

The other regions are coarsened with $(3\times3\times3)$ scheme. Due to the grid coarsening, MGCT has significantly smaller Laplacian matrix, reduced by more than 50% from the GCT's. As a result, the computation time for eigen-decomposition of MGCT Laplacian is reduced by 30% shown in Figure 3.18. The reason that the effect of computation time reduction is slightly smaller than the degree of Laplacian size reduction is that the grid coarsening generates more off-diagonal elements in the matrix by additional connections between coarsened grids and neighboring fine grid cells. However, because it is computed only once for model calibrations, MGCT benefits over GCT from the lighter computation loads, in addition to its ability to adjust the resolutions within each basis function.

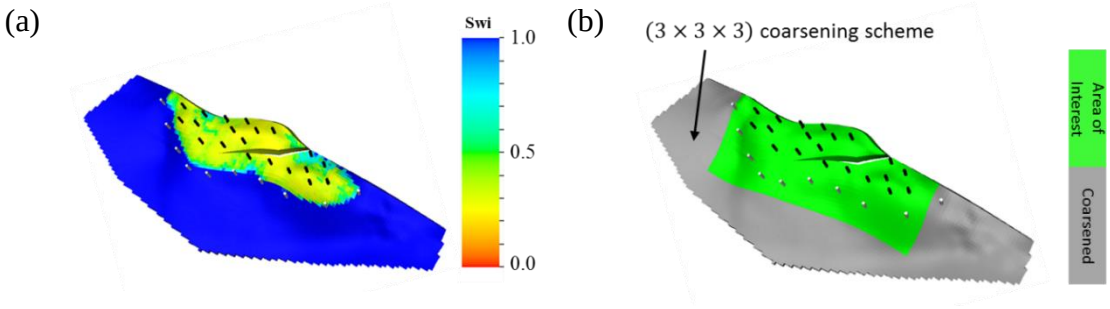

Figure 3.17 Initial water saturation and well distribution and (b) AOI for Brugge model

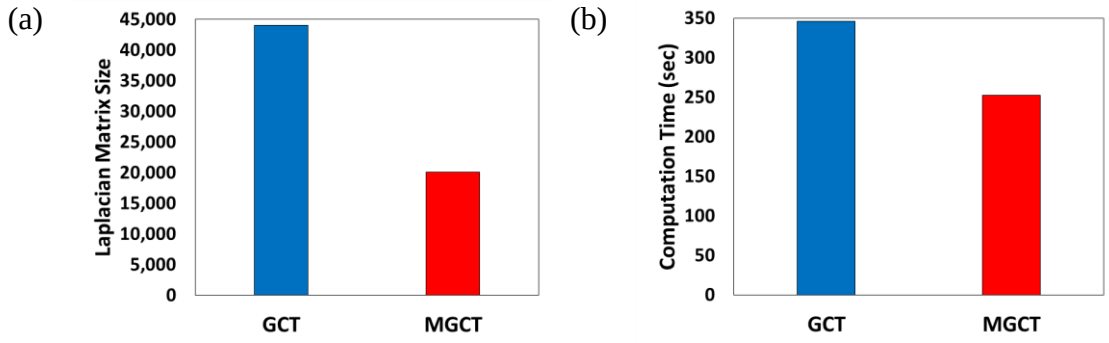

Figure 3.18 Comparison of GCT and MGCT for (a) Laplacian matrix size and (b) computation time for eigen-decomposition

In order to compare the history matching performances, the same number of MGCT basis functions are selected with the same sorting method, shown in Figure 3.19. All the MGCT basis functions have higher modal frequencies in the AOI than the coarsened peripheral area. The re-parameterized permeability multipliers by these basis functions have higher spatial resolutions in the AOI, so that we can adaptively update the reservoir properties that are amenable to variant data resolutions.

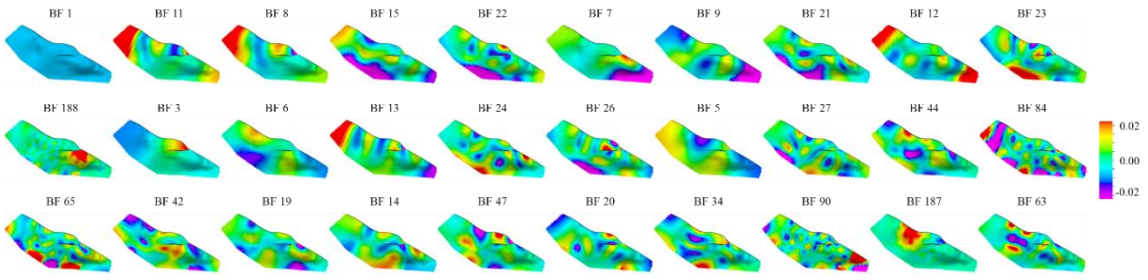

Figure 3.19 MGCT basis functions selected for model calibration of Brugge model

3.4.1.2. Comparison of History Matching Performance

The objective functions in the Brugge case are data misfits for water cut and bottom-hole pressure of each producer as in equation (3.17) and (3.18). O_{WCT} is the objective function for water cut, N_{well} is the number of wells, N_{time} is the number of time steps, $WCT_{i,j}^{observed}$ and $WCT_{i,j}^{simulation}$ are the observed and simulated water cuts of j^{th} well for i^{th} time step. The same nomenclatures are followed for bottom-hole pressure. In a multi-objective optimization method, the objective functions are not combined, but remain independent while being minimized by the dominance relationship between solutions. To more precisely compare the effect of parameterization methods (GCT and MGCT) on the model calibrations, all the parameters for MOGA are same as in Table 3.1, except for the basis formulation.

$$O_{WCT} = \sum_{j=1}^{N_{well}} \sqrt{\frac{1}{N_{well}} \sum_{i=1}^{N_{time}} \left(WCT_{i,j}^{observed} - WCT_{i,j}^{simulation} \right)^2} \tag{3.17}$$

$$O_{BHP} = \sum_{j=1}^{N_{well}} \sqrt{\frac{1}{N_{well}} \sum_{i=1}^{N_{time}} \left(BHP_{i,j}^{observed} - BHP_{i,j}^{simulation} \right)^2} \tag{3.18}$$

Table 3.1 MOGA parameters in the Brugge case

Objective function	WCT and BHP misfits
Variable	Absolute permeability (isotropic)
Number of basis functions	30
Population size	100
Maximum generation	50

After the model calibrations through MOGA, both objective functions are significantly reduced as shown in Figure 3.20(a), which shows the results at the 50th generation. Only with different basis formulation, MGCT makes the improved Pareto front than GCT, meaning smaller data misfits. It is expected that given the same number of parameters, MGCT can capture more detailed heterogeneity in the AOI through the integration of data that also has higher resolution in the same region. The individual data misfit reduction through the generations are shown in Figure 3.20(b) and (c). It is confirmed that MGCT has better performance than GCT.

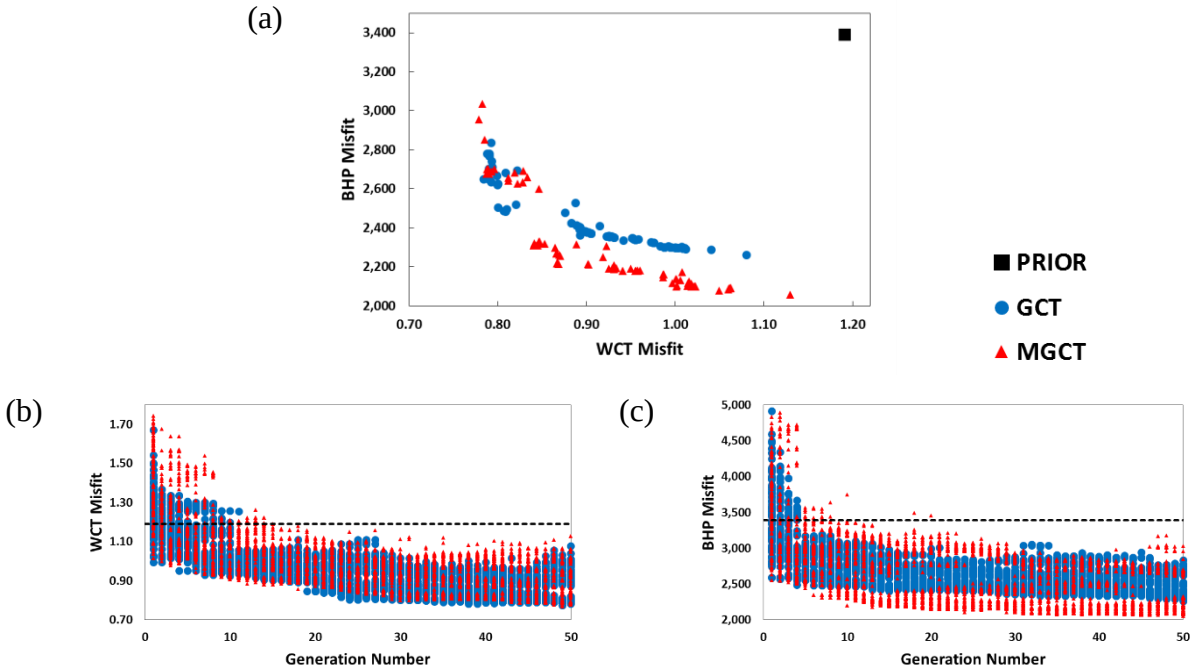

Figure 3.20 (a) Data misfits at the 50th generation, (b) water cut misfits through generations, and (c) bottom-hole pressure misfits through generations by GCT and MGCT

The simulation results at the 50th generation for each of the 20 production wells are shown in Figure 3.21 and Figure 3.22. Most of the wells have significant improvements on the data misfit both for water cuts and bottom-hole pressures. A few wells (P10 for water cut, and P2, P5, P11, P12, P13 for bottom-hole pressure) have remained unchanged or have deteriorated matching results. The more important aspect here is that we have better improvements with MGCT than with GCT. It can be more effectively compared in the data misfit histogram of all populations at the 50th generation, as shown in Figure 3.23 and Figure 3.24. These figures clearly show the improved data misfit distributions compared to the initial misfit. In P9, for example, GCT reduced both water cut and bottom-hole pressure misfits; however, MGCT reduced data misfits even further as implied by the distributions shifted closer to zero. Based on the data misfit histograms, MGCT has smaller data misfits for both water cut and bottom-hole pressure at all the wells, except only for one well (P15). Therefore, it is concluded that MGCT is more computationally efficient and better able to calibrate reservoir models to the observed data which has variant resolution throughout the reservoir. It is because MGCT basis functions comply with the data resolution by its formulation.

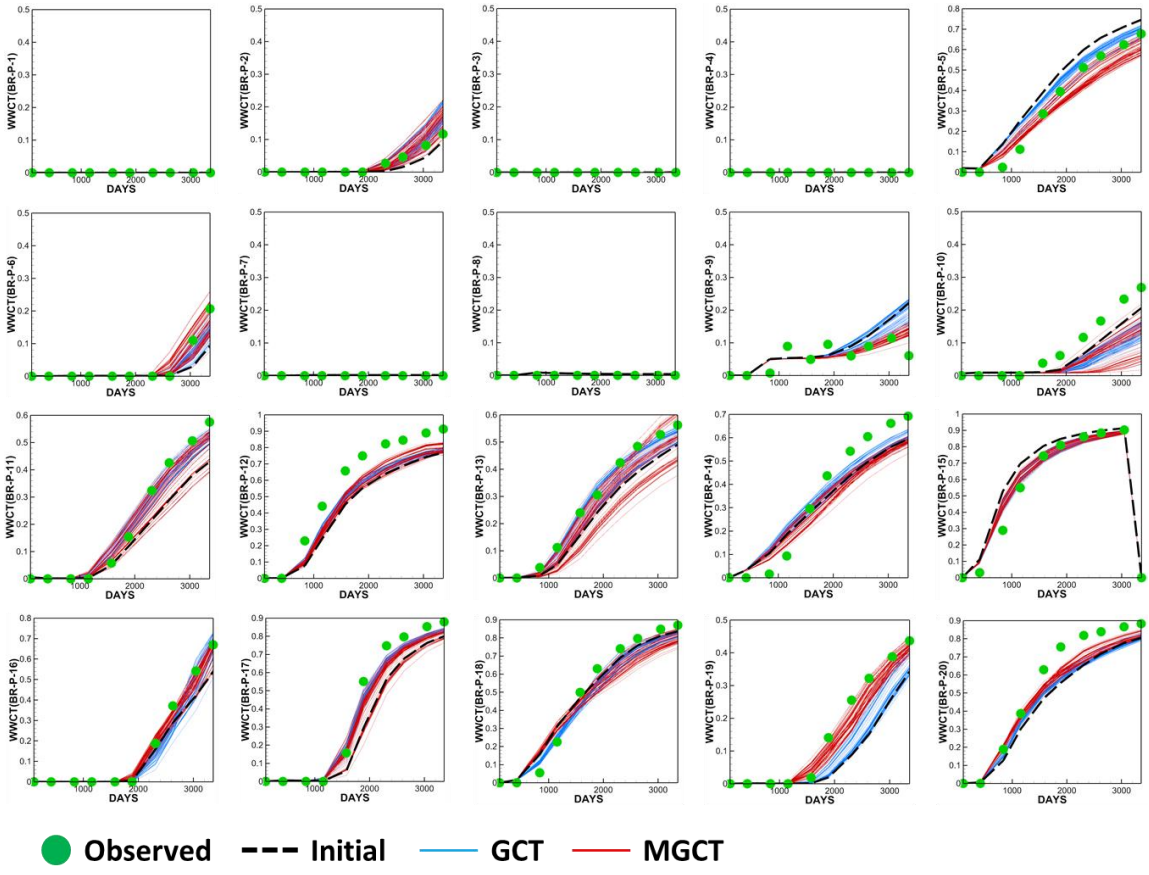

Figure 3.21 Simulated water cut at each production well corresponding to the observation, initial, GCT and MGCT for Brugge case

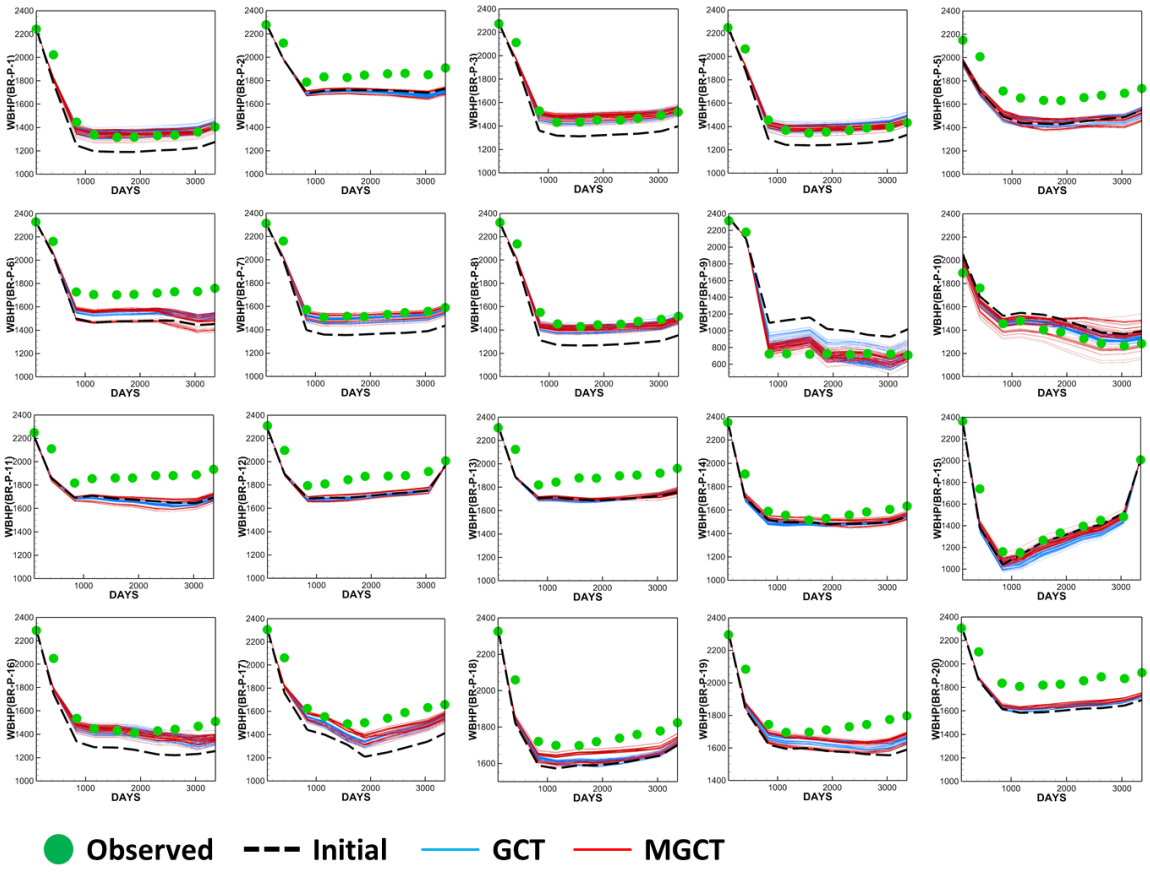

Figure 3.22 Simulated bottom-hole pressure at each production well corresponding to the observation, initial, GCT and MGCT for Brugge case

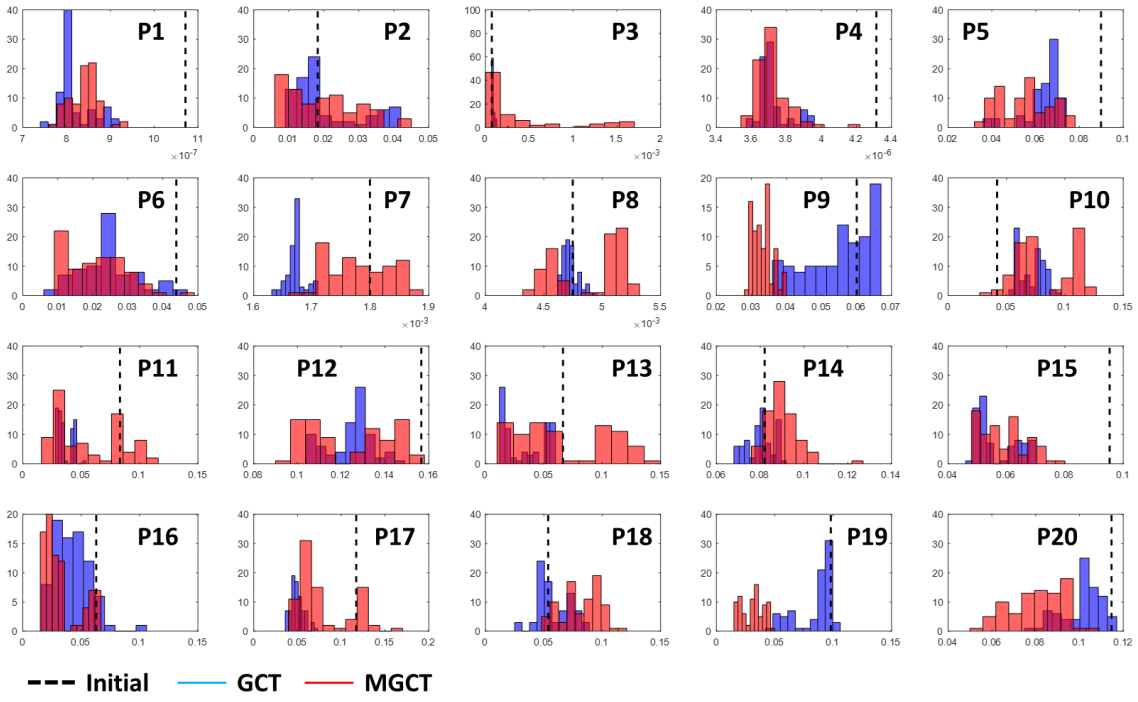

Figure 3.23 Data misfit histogram for water cuts of all populations at the 50th generation in Brugge case

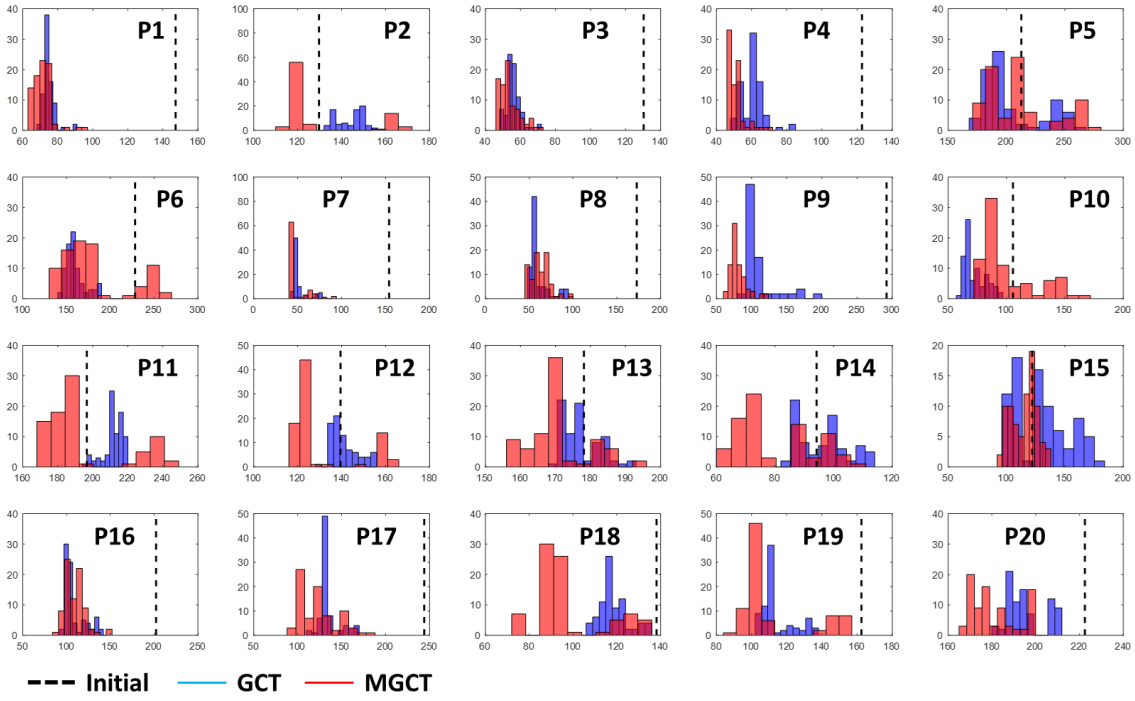

Figure 3.24 Data misfit histogram for bottom-hole pressures of all populations at the 50th generation in Brugge case

To compare the updated permeability fields, one model is selected each from GCT and MGCT results. Both the calibrated models show smooth and continuous geological features similar to the prior model, shown in Figure 3.25. Large scale heterogeneity updates are shown for the entire region and the AOI in Figure 3.26, respectively. As expected, MGCT shows multi-resolution permeability updates, higher in the AOI and lower at the peripheral area.

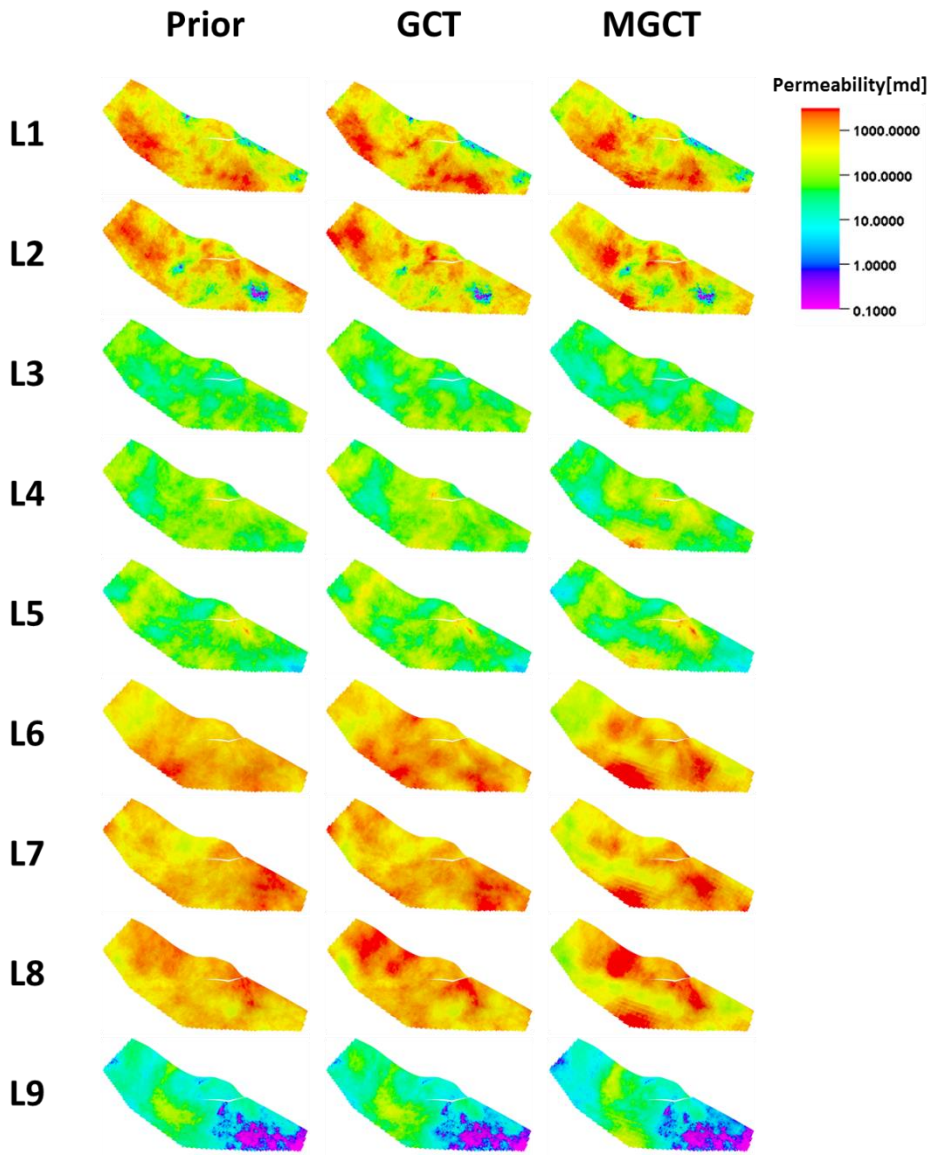

Figure 3.25 Prior permeability field for the prior model (left), updated permeability field by GCT (middle), and by MGCT (right) in Brugge case

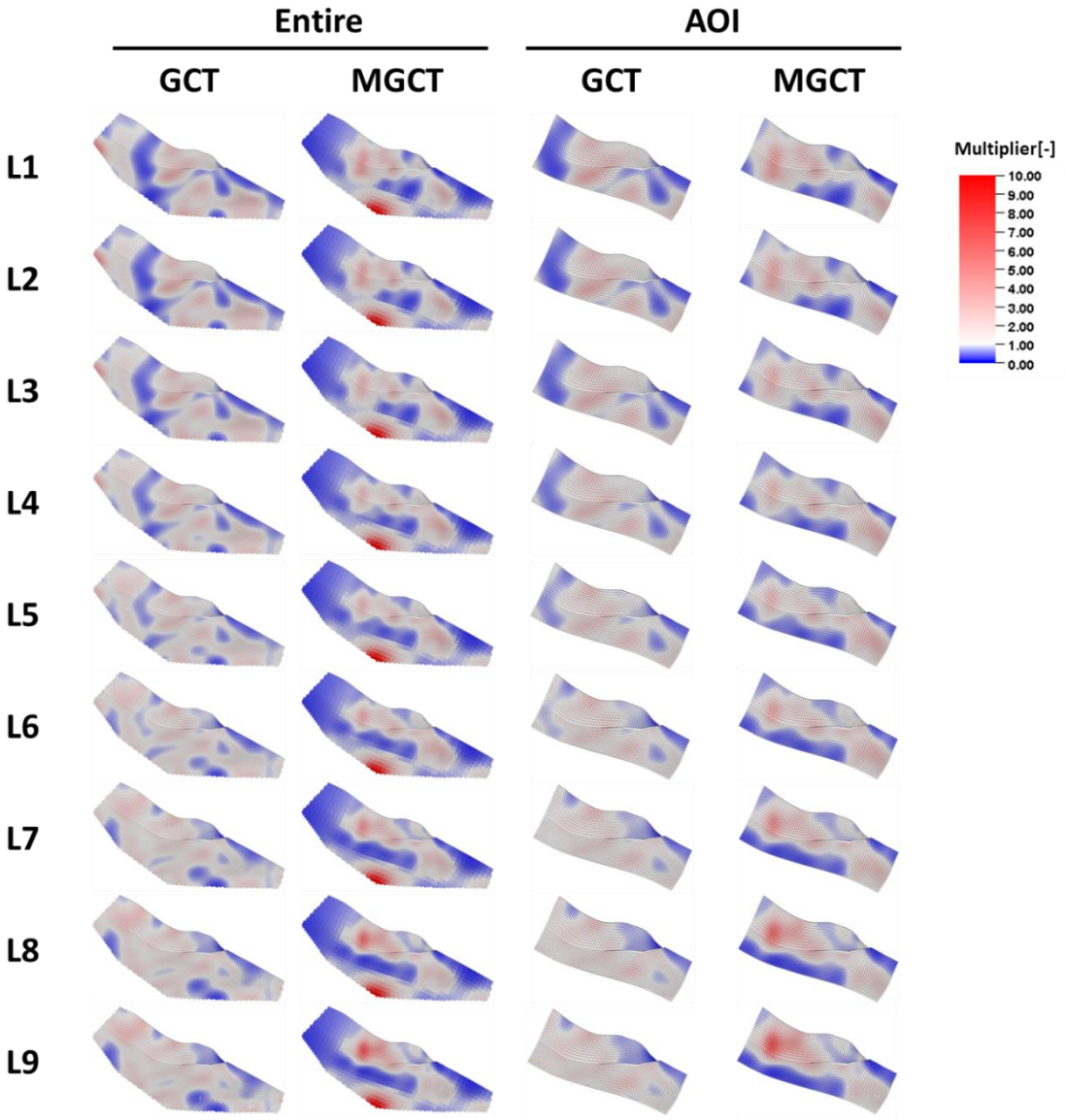

Figure 3.26 Permeability multiplier fields for the entire reservoir and for the AOI calibrated by GCT and MGCT in Brugge case

3.4.2. Unconventional Tight Oil Reservoir With Multi-Stage Hydraulic Fractures

In this section, we apply MGCT to parameterize matrix permeability in an unconventional tight oil reservoir with multi-stage hydraulic fractures, where the AOI is

usually within stimulated reservoir volume (SRV), to show its ability to calibrate the rock property with multiple levels of spatial detail and to demonstrate the entire history matching workflow. Tartan grid is used in order for propped fractures to be located in the refined grid so that the flow dynamics are more accurately simulated. In a low permeable tight oil reservoir, a horizontal well is completed and perpendicular hydraulic fractures are generated. The detailed model description and prior information are shown in Table 3.2. The prior permeability field is as in Figure 3.27(a) with a cube-cropped region to show both matrix and hydraulic fractures. The AOI is shown as a green box in Figure 3.27(b). The producer is constrained by oil rate and we calibrate the rock properties and uncertain hydraulic fracturing parameters to match the observed water cut and bottom-hole pressure.

Table 3.2 Model description and prior information for the tight oil reservoir with multi-stage hydraulic fractures

Parameter	**Range**
Model size	$\sim 2.4 million \left(41 \times 1267 \times 46\right)$
Phase	Oil and water
Matrix permeability	0.0001 ~ 0.0076 mD
SRV permeability multiplier	50
Hydraulic fracture conductivity	120 mD-ft
Number of fracture stages	12
Number of clusters per stage	10
Fracture half length	130 ~ 311 ft
Production period	10 months

(a)

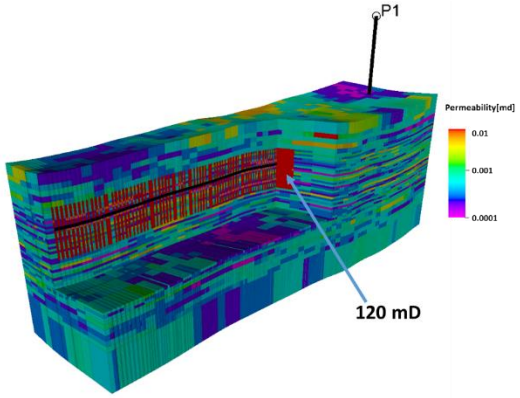

(b)

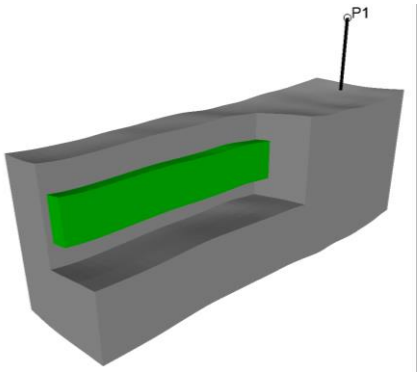

Figure 3.27 (a) Prior permeability field and (b) AOI as the green box for the tight oil reservoir with multi-stage hydraulic fractures

3.4.2.1. Sensitivity Analysis

The first step for the model calibration is to select key parameters that are sensitive enough to change the objective functions, which in this application are data misfits for water cut and bottom-hole pressure. This parameter set size reduction by removal of insensitive parameters further improves regularization of the inverse problem. To eliminate disproportionate parameter perturbation sizes and dimensions, the dimensionless scaled sensitivity is used as in equation (3.19) (Olalotiti-Lawal et al. 2017, 2019, Onishi et al. 2019), where x_{Base} is the prior parameter, Δx is the parameter

perturbation, J_{Base} is the objective function for the prior model, and ΔJ is the perturbed objective function caused by Δx. As we have two separate objective functions (water cut misfit and bottom-hole pressure misfit), two sensitivity analyses are performed with the ranges shown in Table 3.3. Fracture half length is set as a constant value within each group ('XfCell1', 'XfCell2', 'XfCell3'). The stage groups are defined as in Figure 3.28.

$$sensitivity_x = \frac{\Delta J / J_{Base}}{\Delta x / x_{Base}} \tag{3.19}$$

Table 3.3 Parameter descriptions and ranges for sensitivity analyses

Parameter	Description	Low	Base	High
permHF	Conductivity of hydraulic fractures (mD-ft)	90	120	150
permMulSRV	Permeability multiplier for SRV	5	40	80
permMulMtr	Permeability multiplier for matrix	0.5	1	10
XfCell1	Fracture half length in Group 1 (ft)	130	198	311
XfCell2	Fracture half length in Group 2 (ft)	130	198	311
XfCell3	Fracture half length in Group 3 (ft)	130	198	311

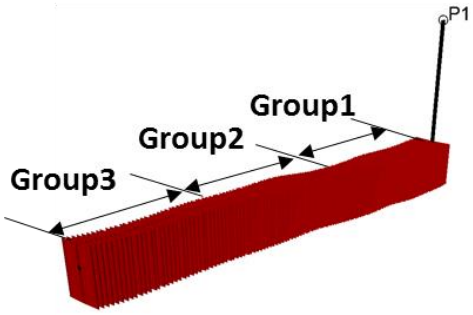

Figure 3.28 Group of hydraulic fracturing stages

The results of sensitivity analyses are shown in the tornado charts for water cut and bottom-hole pressure as in Figure 3.29. The same parameter order as in the tornado chart of water cut is used for the bottom-hole pressure in order to easily compare the effect of parameters on the data misfits. Matrix permeability is the most important parameter in that it has the most significant impact on water cut data misfit and on the positive sensitivity side of bottom-hole pressure misfit (right side of the tornado plot in Figure 3.29(b)). Therefore, matrix permeability field is parameterized with MGCT rather than using single uniform multiplier, in order to make more variability. MGCT gives us higher degree of freedom in the AOI, which is the SRV in this case. The opposite direction of sensitivity implies that there is a potential conflict between data misfits. For example, when taking the high value of fracture half length at group 2 (orange bar of 'XfCell2'), water cut misfit increases but bottom-hole pressure misfit decreases. That is, most of parameter perturbations reduce one data misfit while increasing the other. Therefore, all the other parameters, which are related with hydraulic fracturing performance and have impacts on the data misfits, are also included in the history matching through MOGA.

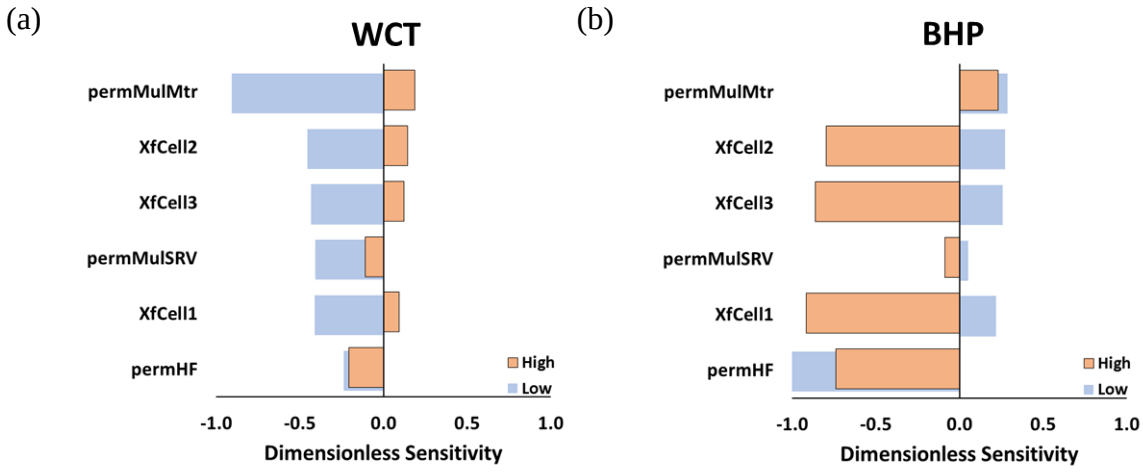

Figure 3.29 Dimensionless sensitivity of model parameters to (a) water cut misfit and (b) bottom-hole pressure misfit

3.4.2.2. Re-parameterization Analysis

To decide the optimal number of basis functions, the re-parameterization analysis is performed and the results are shown in Figure 3.30. In this case, six basis functions are selected as indicated by red dotted lines in Figure 3.30(a) and (b). The improvement of spatial heterogeneity information is negligible with increasing parameter set. The selected MGCT basis functions are shown as the first row in Figure 3.31 and show slightly higher modal frequencies in the AOI than the coarsened peripheral area. The small resolution differences within the low frequency basis functions are observed. It is because the major modal variation occurs along the J direction due to its significantly larger number of grid cells than the other directions. Therefore, at the $I-K$ plane of certain J index, the numbers of grid cells of I and K directions are not enough to have visible variations in

the low frequency basis functions. The higher frequency basis functions, some of which are already selected, are shown in the second row of Figure 3.31 for the reference.

(a)

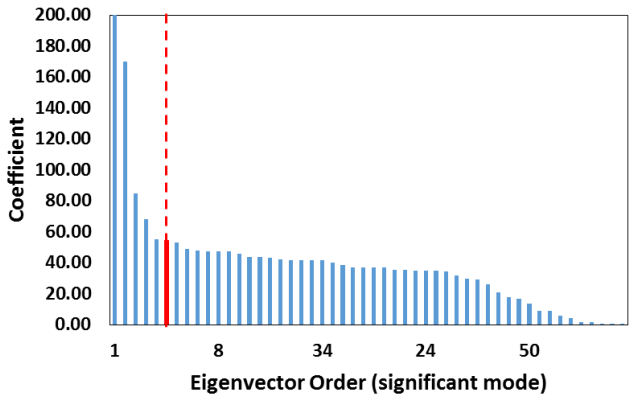

(b)

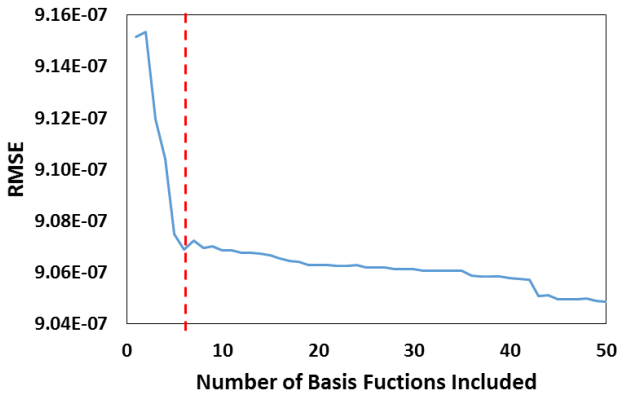

Figure 3.30 (a) Sorted coefficients in a significant mode and (b) the corresponding RMSE of MGCT in the tight oil reservoir

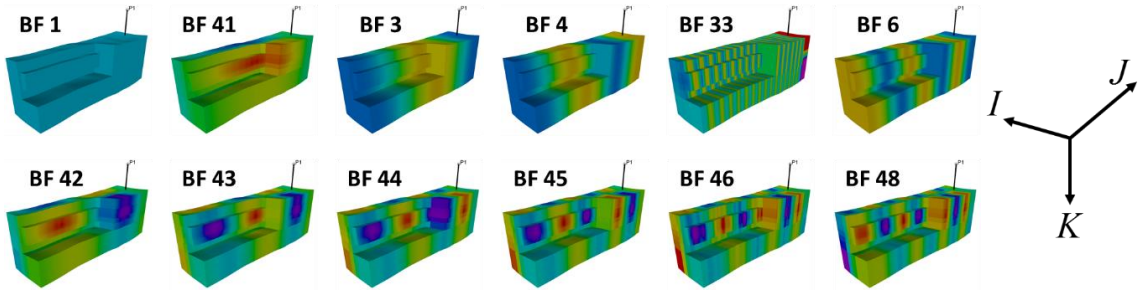

Figure 3.31 MGCT basis functions of tight oil reservoir model. First row shows the selected basis functions for model calibration, and second row shows the higher frequency basis functions as examples of visible resolution differences

3.4.2.3. History Matching

As the data misfits show opposing trends in the sensitivity analysis, MOGA is used for the model calibration with the parameters in Table 3.4. Parameterization is applied to matrix permeability as in equation (3.20) to keep the resolution of prior spatial heterogeneity.

Table 3.4 MOGA parameters in the tight oil reservoir case

Objective Function	Water cut misfit Bottom-hole pressure misfit
Variable	Matrix permeability (6 basis coefficients) SRV permeability multiplier (1 variable) Fracture conductivity (1 variable) Fracture half length (3 variables)
Number of Basis Functions	6
Population Size	40
Maximum Generation	10

$$u = u_0 \circ \Phi v \tag{3.20}$$

where u_0 is the prior matrix permeability field, ' $\circ$ ' represents an entrywise product between two vectors. We parameterize matrix permeability multiplier field in a low rank approximation and basis coefficients are updated to calibrate the matrix permeability field.

After the model calibration through MOGA, both objective functions are significantly reduced as shown in Figure 3.32. It does not show a clear Pareto front. MOGA always outperforms the aggregated sum single objective genetic algorithm whether objective functions are strongly conflicting each other or not, except when there are specific weighting factors for each objective. Without any preferred weighting factors, as in this case, we can accept the significant data misfit reductions through MOGA after 10 generations. Individual data misfit reductions through the generations are also shown in Figure 3.32(b). Notice the logarithmic units of axes.

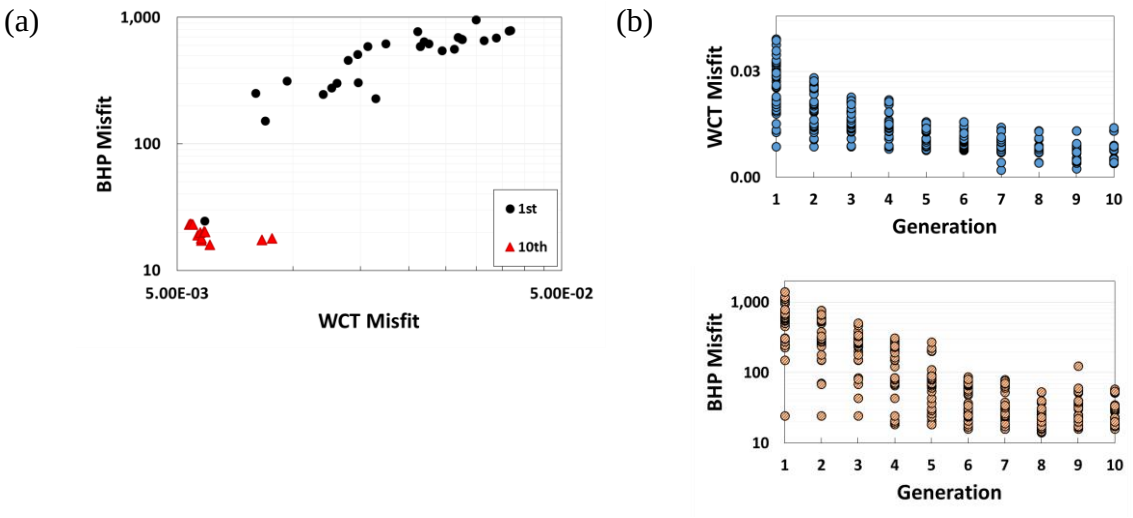

Figure 3.32 Data misfits comparison (a) at the 1st and 10th generation and (b) individual misfits through all the generation

The updated simulation results of water cut and bottom-hole pressure at the 10th generation are shown in Figure 3.33. Compared with the 1st generation, significant improvements on both data misfits are achieved.

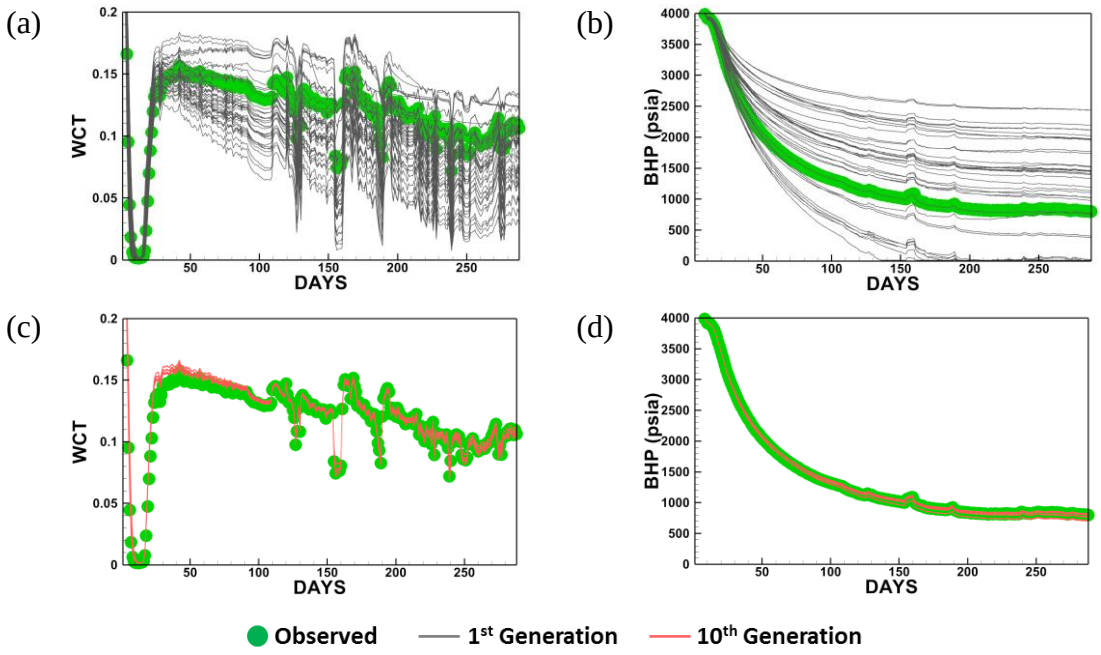

Figure 3.33 (a) Simulated water cut and (b) bottom-hole pressure at the 1st generation and (c) simulated water cut and (d) bottom-hole pressure at 10th generation along with observed data

In the boxplots of Figure 3.34, uncertainty reduction of the parameters are observed after history matching. The first generation of permeability multiplier for SRV in Figure 3.34(a) has a high uncertainty with the evenly distributed populations within the specified range. After MOGA, the 10th generation has a lower uncertainty with decreased values. The uncertainty on the hydraulic fracture conductivity in Figure 3.34(b) has also

been significantly reduced, with the median value shift from 120 mD-ft to 110 mD-ft. For the fracture half lengths, in Figure 3.34(c), the uncertainties on all the groups have been reduced, requiring longer fractures in a group 1 and shorter fractures in group 2 and 3. The parameter collapses for group 1 and 3 ('XfCell1', 'XfCell3') are caused by the discontinuous representation of fracture half length by the number of grid cells to describe the hydraulic fracture planes. Figure 3.34(d) shows the MGCT basis coefficients used to calibrate the matrix permeability field to the production data. A comparison of matrix permeability multiplier fields between 1st and 10th generations is shown in Figure 3.35. Each line represents the distribution of the matrix permeability multipliers for every grid cells within a single model. From the broad spread of the 1st generation to the narrow spread of 10th generation, along with the box plots in Figure 3.34(d), it is clear that the uncertainty of a matrix permeability field has been reduced after history matching.

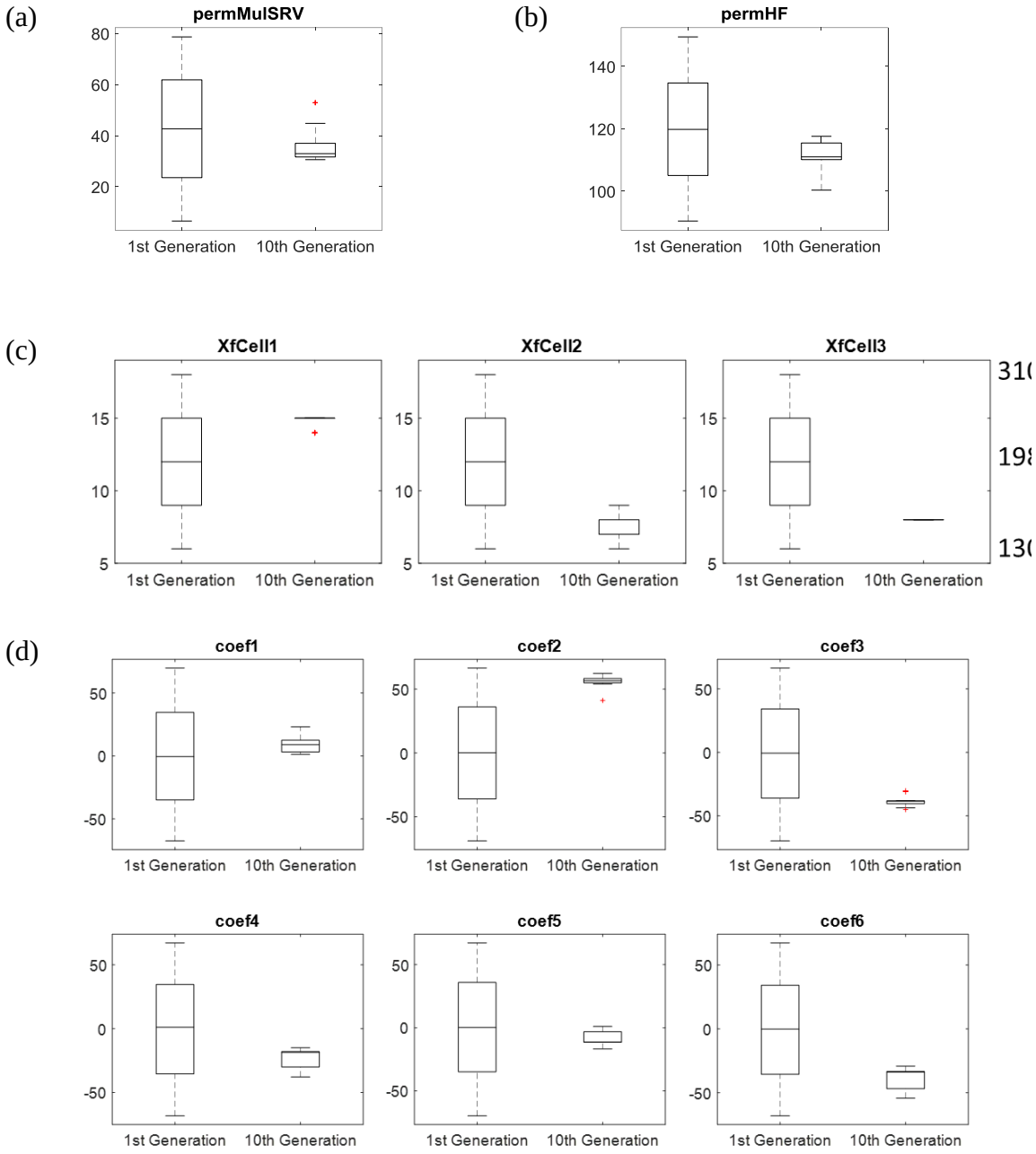

Figure 3.34 Box plots of parameter distribution for 1st and 10th generations. (a) Permeability multiplier for SRV. (b) Hydraulic fracture conductivity. (c) Fracture half length on each group. (d) Basis coefficients for matrix permeability multiplier

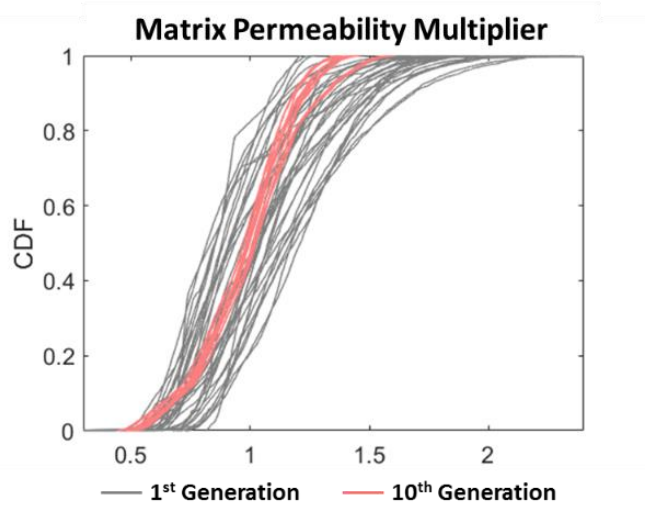

Figure 3.35 Comparison of matrix permeability multiplier fields between 1st and 10th generations

3.4.2.4. Production Forecast

The history matched models at the 10th generation are used to predict future production as in Figure 3.36. The constraint for the history matching was oil production rate. In the production forecast, however, the operating constraint is a bottom-hole pressure (800 psia). The results show the variations of predicted water cut and oil production rate.

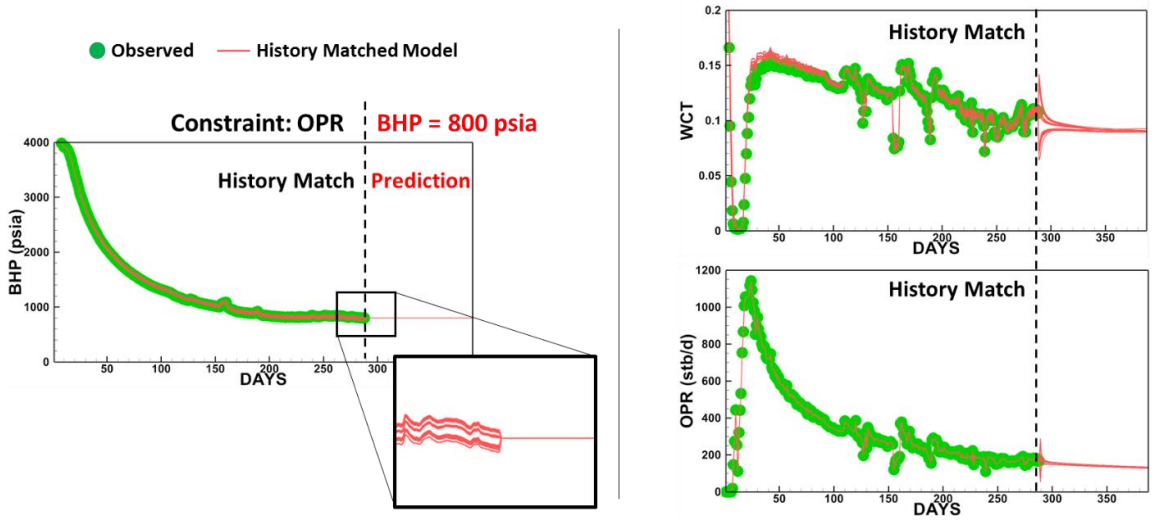

Figure 3.36 Production forecast with uncertainty quantification by history matched models

3.5. Conclusions

In this chapter, we have introduced a novel multi-resolution parameterization method for efficient history matching, especially when the spatial data resolution is variant in a reservoir. The multi-resolution basis vectors are achieved by coarsening the region outside AOI and eigen-decomposing the corresponding grid Laplacian. By this method, the resolution in the AOI becomes higher at the cost of lower resolution in the coarsened region. Basis vectors are then used to linearly map the spatial properties in grid cells to parameters in transform domain, which are updated in the history matching.

As MGCT is still dependent only on the grid connectivity, the basis functions can be constructed from any grid geometry if the connectivity is updated according to the coarsening schemes. Due to the coarsening, it has a smaller Laplacian matrix than GCT, and therefore requires a reduced computation time for eigen-decomposition. The more powerful aspect of MGCT is the ability to adjust the modal frequencies or resolutions of basis functions to comply with the various data resolutions. Hence, it better regularizes the underdetermined history matching problem compared to GCT.

In the applications of MGCT to the model calibrations, multi-objective genetic algorithm was utilized to directly use the dominance relation between each solutions and to secure as diverse realizations as possible that equivalently meet the data misfit criteria. We showed in the conventional waterflooded reservoir that history matching quality can be improved by the proposed multi-resolution parameterization compared to the uniform-resolution parameterization. We also demonstrated its applicability to history matching of the unconventional tight oil reservoir with multi-stage hydraulic fractures.

Although this study employs multi-resolution parameterization method to the history matching with a single iteration (the same number of basis functions through MOGA), the sequential refinement of spatial properties by iteratively adding more basis functions can be used to get better improvements in data misfits. Whether we use a single iteration or sequential refinement method, MGCT will outperform GCT, when there is a variation on data resolutions.

4. PARAMETERIZATION OF EMBEDDED DISCRETE FRACTURE MODELS (EDFM) FOR EFFICIENT HISTORY MATCHING OF FRACTURED RESERVOIRS

4.1. Chapter Summary

Embedded Discrete Fracture Model (EDFM) is a promising approach to describe the reservoirs with fractures. Conventional streamline-based inversion method has been limited to the dual-porosity models where the natural fractures are modeled implicitly and flow between matrix blocks is not accounted for. To address this challenge, we propose a novel parameterization and hierarchical multi-scale history matching formulation for EDFM's. We sequentially includes basis functions, from large to small scale, to calculate basis coefficient sensitivity combined with streamline-based analytical sensitivity, for updating matrix and fracture properties to match the reservoir dynamic response.

In EDFM dominant fractures are explicitly represented within the matrix domain. The matrix-fracture and fracture-fracture interactions are modeled using non-neighbor connections (NNCs) with corresponding transmissibility. In this research, grid connectivity information including NNCs and the reservoir properties in the prior model are first used to construct a grid Laplacian matrix. Next, the eigenvectors of the Laplacian matrix are used as the transformation basis vectors through which matrix and fracture properties are mapped to a low-dimensional transform domain. This step significantly reduces the number of unknowns and also regularizes the inverse problem. Finally, the basis coefficient sensitivity in the transform domain is analytically calculated using

streamlines and the updated basis coefficients are then used to reconstruct the reservoir property field.

We first illustrate the proposed parameterization of the EDFM and its effectiveness by reconstructing low rank approximations of the spatial distribution of the matrix and fracture properties. Conventional streamline-based inversion method typically leads to large property changes along the streamlines. With the proposed parameterization approach, the basis coefficient sensitivities enable us to effectively calibrate the EDFM in a more geologically continuous manner on both matrix domain and fracture planes. We demonstrate the power and efficacy of our method through application to a field scale reservoir model with complex fault structure, channels, and dominant natural fractures. The example involves waterflood history matching with water-cut and bottom-hole pressure data. The proposed approach effectively updates the prior permeability field along the fracture planes and the matrix domain, resulting in significantly improved history match.

The parameterization of EDFM has high compression power to represent important geological trend and fracture properties with significantly reduced number of parameters. The new model calibration method extends the capability of the streamline-based inversion method to explicitly model flow in natural fractures and also flow between matrix blocks.

4.2. Introduction

Significant amount of hydrocarbons come from conventional reservoirs with natural fractures or faults and unconventional reservoirs with hydraulic fractures. It has been challenging to accurately predict future production and optimize development plan for reservoirs with fractures due to its complexity and heterogeneity. Therefore, reservoir simulation and characterization of complex fracture system are critical to develop and manage the fractured reservoirs.

Dual continuum model was introduced by Warren and Root (1963) and has been widely used for reservoir simulation with densely distributed small-scale fractures (Azom and Javadpour 2012, Kang et al. 2015, Sævik, Lien, and Berre 2017). For reservoirs with sparsely distributed large-scale fractures, it is more appropriate in terms of accuracy to use Discrete Fracture Model (DFM) to represent fluid flow within fractures and between matrix and fractures. However, it requires high computation time for simulation and an unstructured grid system, introducing additional complexity for field scale models. Embedded Discrete Fracture Model (EDFM) was proposed to adopt accuracy of DFM and efficiency of dual continuum model (Li and Lee 2008). There have been studies on history matching of EDFM by Bayesian approach (Chai, Tang, et al. 2018, Chai, Yan, et al. 2018, Dachanuwattana et al. 2018). These studies are limited to calibrate variables that are constant over the reservoir and in general are incapable of calibration of spatial heterogeneity distribution. Streamline-based inversion method is known to efficiently improve the history matching quality when used after large-scale calibrations (Kam, Han,

and Datta-Gupta 2017, Hetz, Kim, et al. 2017). However, there has not been any research for the streamline-based inversion on EDFM.

In this chapter, we extend the ABT parameterization to Embedded Discrete Fracture Models (EDFM) by using non-neighbor connections (NNCs) between matrix-fracture and fracture-fracture interactions. During history matching, basis coefficient sensitivity to production data in the transform domain is analytically calculated using streamlines and predefined basis functions. The updated basis coefficients are then used to reconstruct the reservoir property field. The history matching formulation follows the previous adaptive multi-scale approach (Bhark, Jafarpour, and Datta-Gupta 2011, Bhark et al. 2012, Bhark, Jafarpour, and Datta-Gupta 2011). Spatial heterogeneity is sequentially refined by adding basis functions of higher-frequency, until calibration resolution balances with the data resolution. With the proposed parameterization approach, the basis coefficient sensitivities enable us to effectively calibrate the EDFM in a more geologically continuous manner on both matrix domain and fracture planes. We demonstrate the power and efficacy of our method through application to a field scale reservoir model with complex fault structure, channels, and dominant natural fractures.

4.3. Background and Methodology

In this section, background and methodologies of previous studies on EDFM, streamline-based sensitivity, the proposed parameterization, analytical basis coefficient sensitivity, and hierarchical multi-scale history matching formulation are explained.

4.3.1. Embedded Discrete Fracture Model (EDFM)

EDFM adopts accuracy of DFM and efficiency of dual continuum model (Li and Lee 2008) by connecting discrete fractures to the matrix of a structured grid system by additional connection information (NNCs) and corresponding transmissibility. Figure 4.1 shows an illustration of EDFM with the simulated geologic model and the actual grid structure in a numerical domain. In Figure 4.1(a), purple, yellow, and blue lines represent NNCs between fracture-matrix, intersecting fractures, and fracture-fracture respectively. Their transmissibilities are calculated as in equation (4.1) – (4.3) (Moinfar 2013).

$$\text{Fracture-Matrix: } \frac{A^{NNC}k^{NNC}}{d^{NNC}} = \frac{A\bar{k}_{mf}}{\langle d \rangle}, \quad \langle d \rangle = \frac{\int_V x_n dV}{V} \tag{4.1}$$

$$\text{Intersecting Fractures: } \frac{A^{NNC}k^{NNC}}{d^{NNC}} = \frac{T_1 T_2}{T_1 + T_2}, \quad T_i = \frac{k_{f_i}\omega_{f_i} l_{\text{int}}}{d_{f_i}} \tag{4.2}$$

$$\text{Fracture-Fracture: } \frac{A^{NNC}k^{NNC}}{d^{NNC}} = \frac{\omega l_{\text{int}} \bar{k}_{ff}}{d_{ff}} \tag{4.3}$$

For fracture-matrix interaction in equation (4.1), A is the fracture surface area in the grid cell, $\bar{k}_{mf}$ is the harmonic average of matrix and fracture permeabilities, and $\langle d \rangle$ is the average normal distance. x_n is the normal distance of the element from the fracture and V is the volume of grid cell. For the interaction of intersecting fractures in equation (4.2), T_i is a transmissibility of each fracture, where d_{f_i} is the average of normal distances from the center of the fracture subsegments to the intersection line shown as yellow line in Figure 4.1(a), k_{f_i} is a fracture permeability, ω_{f_i} is a fracture aperture, and l_{int} is the

length of the intersection line. For fracture-fracture interaction in equation (4.3), d_{ff} is the distance between the centers of each fractures, ω is the fracture aperture, l_{int} is the length of the intersection line, and $\bar{k}_{ff}$ is the harmonic average of fracture permeabilities.

(a)

(b)

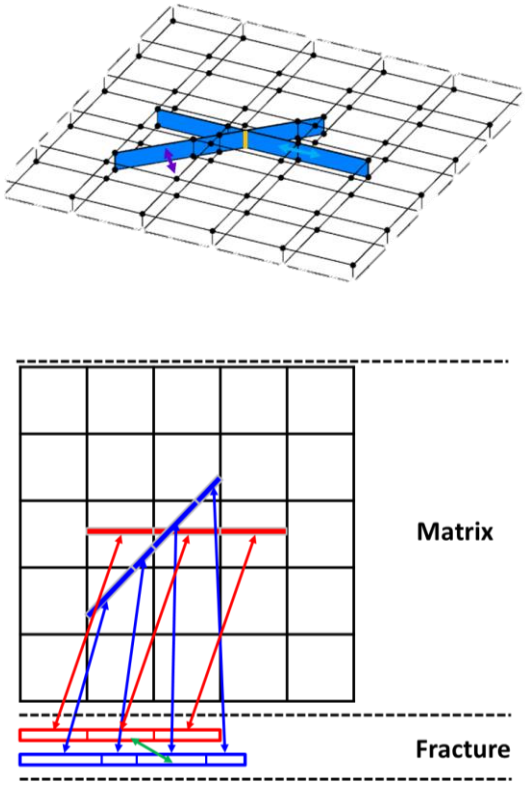

Figure 4.1 An illustration of EDFM with (a) simulated geologic model and (b) actual grid structure in a numerical domain

4.3.2. Parameterization of EDFM

4.3.2.1. Extended Adjacency-Based Transform

In EDFM, fractures are simulated by NNCs and their transmissibilities, located in a separate numerical domain from the matrix domain. The permeability contrast between matrix and fracture is significant, a requirement for the purpose of designing EDFM. Therefore, the previous parameterization methods (GCT, ABT) are not appropriate for EDFM. The elements of similarity matrix for GCT is calculated as in equation (4.4).

$$a_{i,j} = \begin{cases} 1 & \textit{if neighbored} \\ 0 & \textit{otherwise} \end{cases} \tag{4.4}$$

Although it includes all the connectivity information, both the connection within matrix grid cells and the fracture-matrix connection by NNCs, there will be no property information in the basis functions. Therefore, GCT is not appropriate for EDFM that has a significant property contrast between matrix and fracture. ABT takes property difference and distance into account in the similarity matrix as in equation (4.5).

$$a_{i,j} = \exp\left(\frac{-\left\|p_i - p_j\right\|_2^2}{\sigma_p}\right)\begin{cases} \exp\left(\dfrac{-\left\|x_i - x_j\right\|_2^2}{\sigma_x}\right) & \textit{if } \left\|x_i - x_j\right\| < r \\ 0 & \textit{otherwise} \end{cases} \tag{4.5}$$

However, as the fracture numerical domain is separated from the matrix domain in EDFM, the distance between two domains is artificially large. The elements of a Laplacian matrix interacting matrix and fracture will be calculated as zero since the distance ($\left\|x_i - x_j\right\|$ in equation (4.5)) is larger than Euclidean cut-off distance. Therefore, ABT is not appropriate

for EDFM because it does not properly account for the NNCs between matrix and fracture. Considering we are simulating embedded fractures, the distance between matrix and fracture should be treated as almost zero rather than significantly large value. Then, we can approximate $\exp\left(\frac{-\|x_i - x_j\|_2^2}{\sigma_x}\right)$ term as 1 for the connected grid cell pairs.

We propose a novel parameterization method by extending ABT so that it includes the connectivity information in basis functions. The elements of similarity matrix in an extended ABT are calculated as in equation (4.6).

$$a_{i,j} = \exp\left(\frac{-\|p_i - p_j\|_2^2}{\sigma_p}\right)\begin{cases} 1 & \textit{if neighbored} \\ 0 & \textit{otherwise} \end{cases} \tag{4.6}$$

Figure 4.2 shows an illustration of the extended ABT in a 5-points grid system with a fracture embedded. A tilted thin grid cell in Figure 4.2(a) is an embedded fracture and colors represent the property value in each grid cell. The Laplacian matrix of an extended ABT for this model is shown in Figure 4.2(b). The region outlined with a blue dotted line in Figure 4.2(b) explains the similarities within a matrix domain. The yellow box explains the interactions between fracture grid cells and the matrix grid cells. The red box represents the interaction within fracture grid cells.

(a)

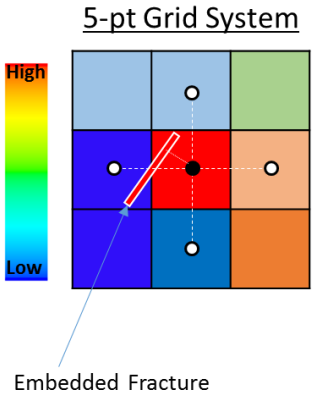

(b)

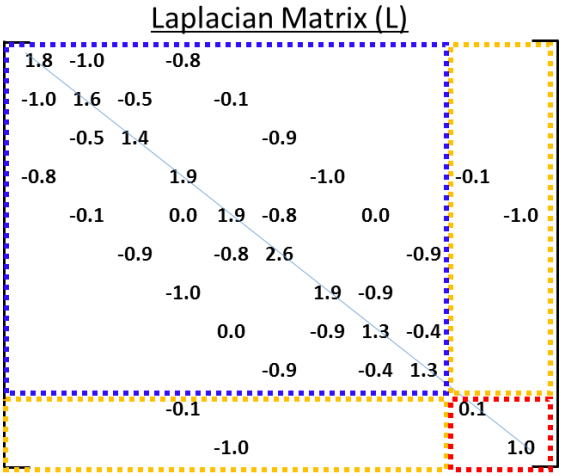

Figure 4.2 Illustration of EDFM and Laplacian matrix of an extended ABT

4.3.2.2. Two-Dimensional Synthetic EDFM

For detailed explanation of the extended ABT, a two-dimensional synthetic EDFM is modeled as in Figure 4.3. The reference permeability field is shown together in Figure 4.3(a), and three-dimensional views of the matrix field and embedded fractures are shown in Figure 4.3(b) and Figure 4.3(c), respectively. The number of matrix grid cells is 2500 (

$50 \times 50 \times 1$) and its size is $1640\,ft \times 1640\,ft \times 33\,ft$. Information on the embedded fractures are given in Table 4.1.

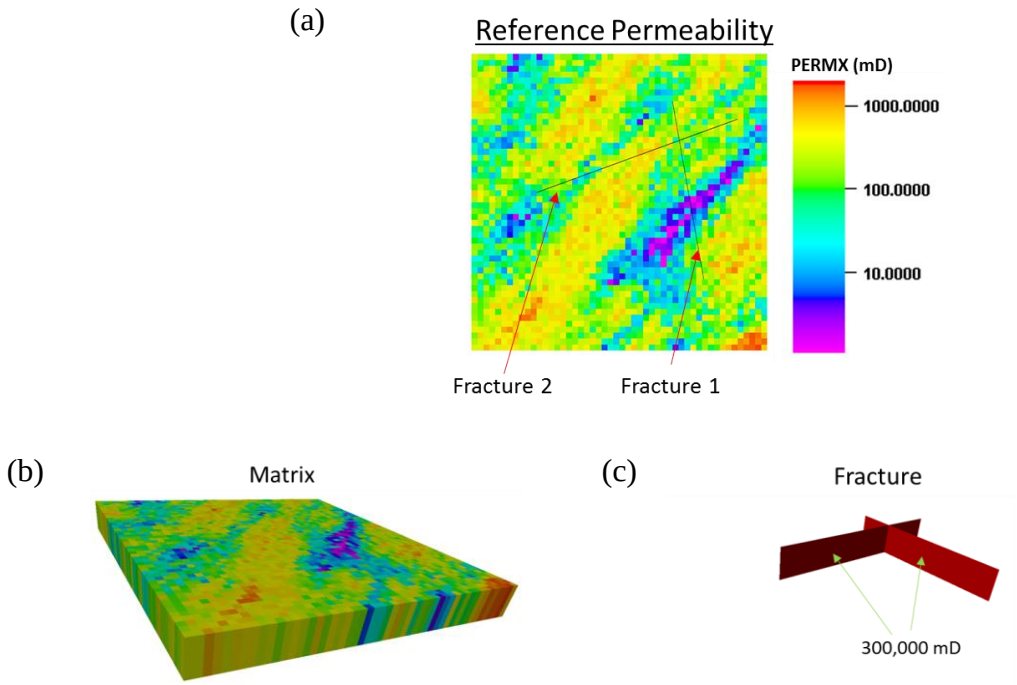

Figure 4.3 Two-dimensional synthetic EDFM. (a) Top view of reference permeability field with matrix and fracture together. Three-dimensional views of (b) matrix field and (c) embedded fractures

Table 4.1 Properties of embedded fractures in a synthetic EDFM

Fracture ID	Starting Point	Orientation	Aperture	Length	Permeability
1	$(1{,}115\ ft,\ 262\ ft)$	80°	$0.05\ ft$	$1{,}000\ ft$	$300\ D$
2	$(1{,}476\ ft,\ 361\ ft)$	160°	$0.05\ ft$	$1{,}200\ ft$	$300\ D$

Basis functions of the extended ABT are shown in Figure 4.4(a) and (b) for matrix and fracture domains respectively. They obviously include not only grid connectivity information but also property information. The low rank approximations of EDFM are shown in Figure 4.5 for the matrix permeability field and fracture permeability.

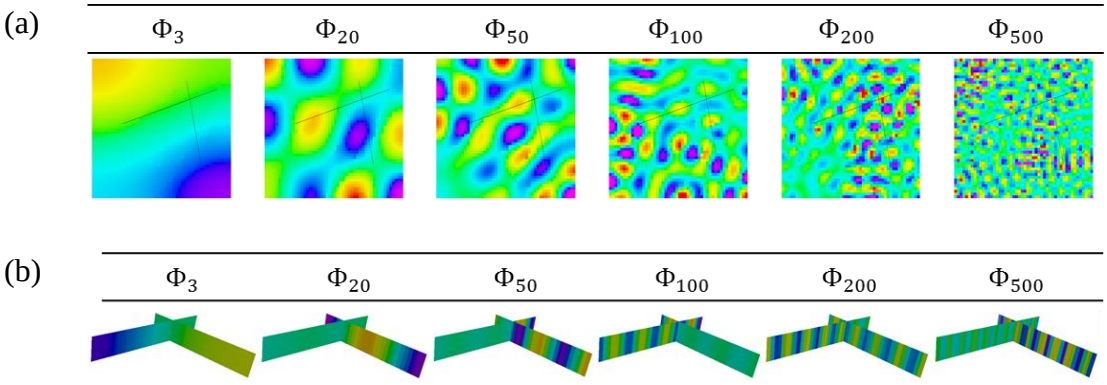

Figure 4.4 Extended ABT basis functions of a synthetic EDFM for (a) matrix domain and (b) fracture domain

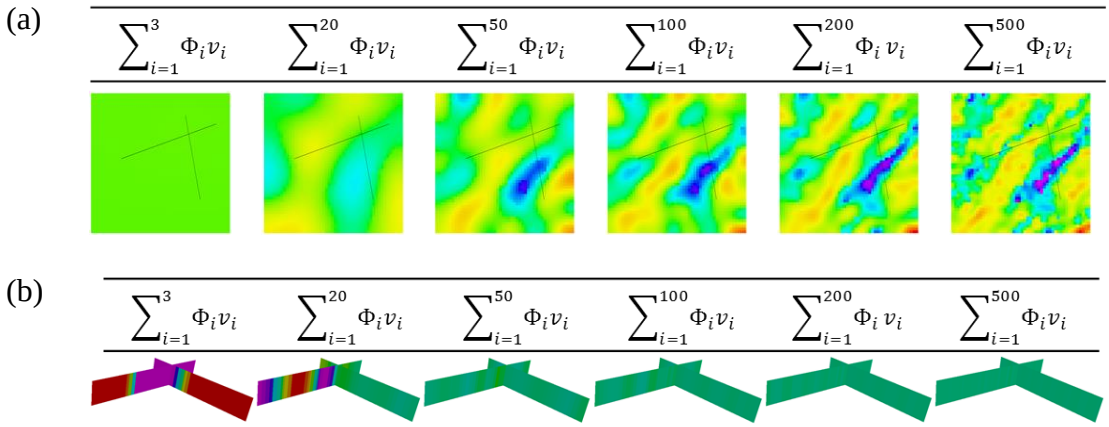

Figure 4.5 Low rank approximations of a synthetic EDFM for (a) matrix permeability field and (b) fracture permeability

The compression performances of the extended ABT are calculated by root mean square error (RMSE) as in equation (4.7) between a low-rank approximation and the reference permeability field, for matrix and fracture separately with respect to the number basis functions. RMSE for the entire field is dominated by several orders of magnitude larger fracture permeability, although the heterogeneous matrix permeability is as important as fracture permeability when characterizing the fractured reservoir model. Therefore, separate RMSE's are calculated as in Figure 4.6 in order to differentiate compression performances on matrix and fracture domains, respectively. While the RMSE for heterogeneous matrix permeability has gradually reduced as more basis functions are included in a re-parameterization, the RMSE for the fracture permeability has rapidly reduced even with first several basis functions. It is attributed to the fact that heterogeneity of fracture domain is significantly smaller than that of matrix domain. In this synthetic case a uniform fracture permeability value is used, and the number of basis functions to

parameterize for fracture domain is much smaller. Therefore, it is comparatively easy to capture the geological trend of fracture domain with smaller number of basis functions.

$$RMSE = \frac{1}{N}\sqrt{\sum_{i=1}^{N}\left|k_i^{reference} - k_i^{re-parameterized}\right|^2} \tag{4.7}$$

(a)

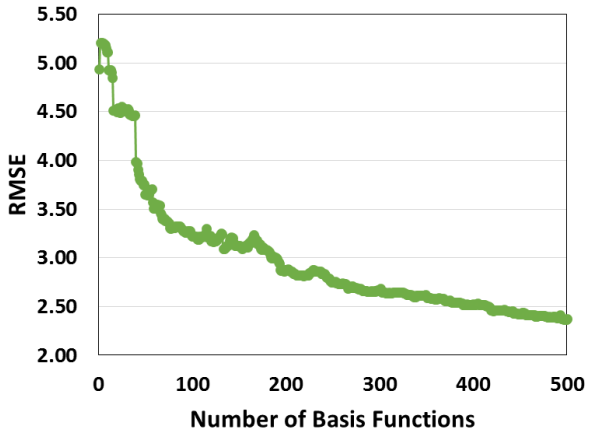

(b)

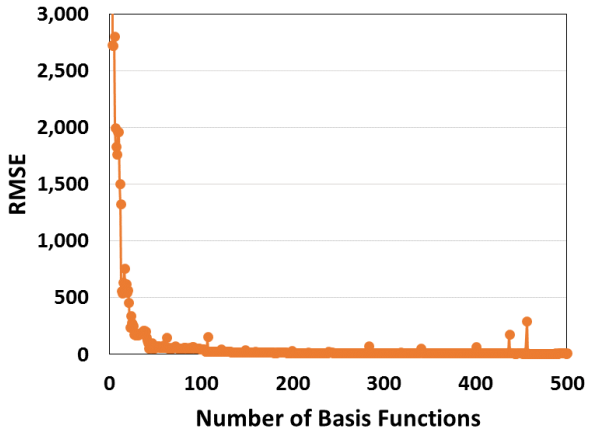

Figure 4.6 RMSE of re-parameterized permeability for (a) matrix domain and (b) fracture domain

In order to eliminate the dominance of fracture permeability on the entire RMSE, a normalized RMSE is calculated as in equation (4.8) to represent the compression performance over the entire reservoir including fractures. Normalized RMSE's for each domain are calculated by normalizing RMSE's with the initial RMSE from the re-parameterization when only the basis function of lowest frequency is used.

$$\text{Normalized RMSE} = \frac{\text{Normalized Matrix RMSE} + \text{Normalized Fracture RMSE}}{2} \quad (4.8)$$

The normalized RMSE for the synthetic EDFM is shown in Figure 4.7, which radically reduces with the first several basis functions. It is obvious that the extended ABT effectively parameterizes EDFM with a small number of parameters.

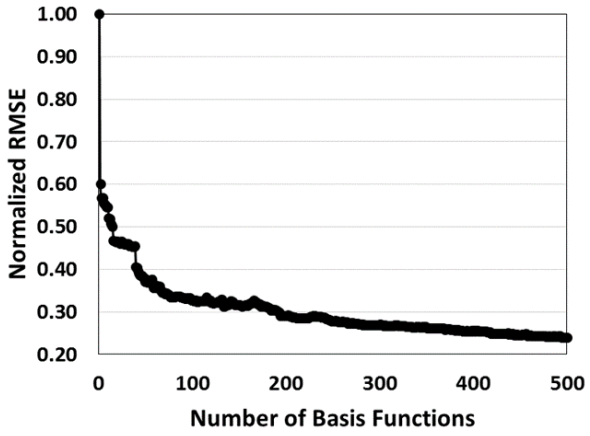

Figure 4.7 Normalized RMSE of re-parameterized permeability field for matrix and fracture domains combined

4.3.3. Streamline-Based Sensitivity

Streamline-based history matching has been widely used as it is highly effective in that parameter sensitivities are analytically computed after a single forward simulation. As the sensitivities are calculated along streamlines, where the properties are updated, it is also efficient to update small scale properties in a high resolution geologic model. There have been research on the analytical streamline-based sensitivity for various historical data (Tanaka et al. 2015, Hetz, Kim, et al. 2017, Kam, Han, and Datta-Gupta 2017, Watanabe et al. 2017, Chen et al. 2019). Streamline tracing in EDFM has recently been developed by Chen et al. (2018). Therefore previous streamline-based history matching algorithm can now be extended to EDFM. In this section, the analytical sensitivities of permeability on water cut and bottom-hole pressure are explained.

4.3.3.1. Saturation Front Arrival Time Sensitivity

Time of flight (TOF), which is the travel time of a neutral tracer along a streamline (Datta-Gupta and King 2007) is expressed as equation (4.9).

$$\tau = \int_{\psi} s(x)\, dr \tag{4.9}$$

where ψ is a streamline trajectory, along which r is the distance, and $s(x)$ is the slowness defined as the reciprocal of the interstitial velocity shown in equation (4.10).

$$s(x) = \frac{1}{\left|\vec{v}(x)\right|} = \frac{\phi(x)}{\lambda_{rt} k(x) \left|\nabla P\right|} \tag{4.10}$$

$\phi(x)$ is porosity, $k(x)$ is permeability at the location x. λ_{rt} and ∇P are total relative mobility and pressure gradient respectively. The shift of travel time to perturbation in permeability and porosity is then approximated by equation (4.11).

$$\begin{aligned}\delta\tau &= \int_{\psi} \delta s(x)\, dr = \int_{\psi} \left[\frac{\delta s(x)}{\delta k(x)} \delta k(x) + \frac{\delta s(x)}{\delta \phi(x)} \delta\phi(x) \right] dr \\ &\approx \int_{\psi} \left[\frac{-\phi(x)}{\lambda_{rt} \left(k(x)\right)^2 |\nabla P|} \delta k(x) + \frac{1}{\lambda_{rt} k(x) |\nabla P|} \delta\phi(x) \right] dr \\ &= \int_{\psi} \left[-\frac{s(x)}{k(x)} \delta k(x) + \frac{s(x)}{\phi(x)} \delta\phi(x) \right] dr\end{aligned} \tag{4.11}$$

The sensitivity of the permeability at a location x on the travel time along a streamline ψ is calculated by equation (4.12), integrating $-\frac{s(x)}{k(x)}$ within a grid cell along the arc length (Δr) of the streamline.

$$\frac{\delta\tau(\psi)}{\delta k(x)} = \int \left[-\frac{s(x)}{k(x)} \right] dr = -\frac{s(x)}{k(x)} \Delta r \tag{4.12}$$

By the Buckley-Leverett equation, the water saturation propagation time is expressed in terms of time of flights as in equation (4.13).

$$\left(\frac{\partial \tau}{\partial t} \right)_{S_w} = \left(\frac{\partial f_w}{\partial S_w} \right)_{S_w} \tag{4.13}$$

Therefore, the sensitivity of travel time of water saturation with respect to permeability at a location x is given by equation (4.14).

$$\frac{\delta t(S_w, \tau; \psi)}{\delta k(x)} = \frac{\delta\tau(\psi)}{\delta k(x)} \frac{\delta t(S_w, \tau; \psi)}{\delta\tau(\psi)} = \frac{\delta\tau(\psi)}{\delta k(x)} / \frac{df_w}{dS_w} = -\frac{s(x)}{k(x)} \Delta r / \frac{df_w}{dS_w} \tag{4.14}$$

4.3.3.2. Bottom-hole Pressure Sensitivity

The pressure drop between wells is expressed as in equation (4.15) by the summation of pressure drops at each grid cells along the streamtube.

$$\Delta P_{well} = \sum_{i=node} \Delta P_i \tag{4.15}$$

The sensitivity of permeability on pressure drop between wells is then approximated by equation (4.16).

$$\frac{\partial \Delta P_{well}}{\partial k_i} = \frac{\partial}{\partial k_i}\left(\sum_{i=node} \Delta P_i \right) \approx \frac{\partial \Delta P_i}{\partial k_i} \tag{4.16}$$

Pressure drop along a streamline is computed by Darcy's law in equation (4.17). It can be represented in terms of the pressure head drop as in equation (4.18).

$$\Delta P_{sl} = \int_{sl} \left(\frac{q_{sl}}{\lambda_{rt} k A_{sl}} dr - \rho g \nabla D \cdot d\vec{r} \right) \tag{4.17}$$

$$\Delta \Phi_{sl} = \Delta P_{sl} + \int_{sl} \left(\rho g \nabla D \right) \cdot d\vec{r} = \int_{sl} \left(\frac{q_{sl}}{\lambda_{rt} k A_{sl}} \right) dr \tag{4.18}$$

Assuming that Darcy's equation can be applied along streamlines, the pressure drop sensitivity along the streamline can be given in equation (4.19), by combining equation (4.16), (4.17), and (4.18).

$$\frac{\partial \Delta P_{well}}{\partial k_i} \approx \frac{\partial \Delta P_i}{\partial k_i} = \frac{\partial \Delta P_{sl}}{\partial k_i} = \frac{\partial \Delta \Phi_{sl}}{\partial k_i} = -\frac{\Delta \Phi_i^{sl}}{k_i} = -\frac{q_i^{sl,eff} L_i}{\lambda_{rt,i} A_i k_i^2} = \frac{\Delta P_i^{sl} + \overline{\rho}_i g \Delta D}{\rho_i^{eff} k_i} \tag{4.19}$$

where $q^{sl,eff}$ is an effective rate along the streamline, A is the associated cross section, and L is distance shown in equation (4.20) – (4.22), respectively.

$$q_i^{sl,eff} = \frac{q_0^{sl}}{\rho_i^{eff}} \tag{4.20}$$

$$A_i = \frac{q_i^{sl,eff} \Delta \tau_i}{\phi_i L_i} \tag{4.21}$$

$$L_i = \sqrt{\Delta x_i^2 + \Delta y_i^2 + \Delta z_i^2} \tag{4.22}$$

q_0^{sl} is the flow rate assigned to streamline starting location and ρ^{eff} is an effective density that captures the fluid volume changes with pressure. Both are traced along streamlines. ΔP_{sl} is calculated by half-cell pressure drop between neighboring grid cells. It is weighted by half-cell transmissibilities shown in equation (4.23) and (4.24). Therefore, pressure drop along streamline is represented by equation (4.25).

$$\Delta P_{i-}^{sl} = \Delta P_{i-1/2} \frac{\frac{L_{i-}}{k_i A_{i-}}}{\left(\frac{L_{i-}}{k_i A_{i-}} + \frac{L_{i-1+}}{k_{i-1} A_{i-1+}} \right)} \tag{4.23}$$

$$\Delta P_{i+}^{sl} = \Delta P_{i+1/2} \frac{\frac{L_{i+}}{k_i A_{i+}}}{\left(\frac{L_{i+}}{k_i A_{i+}} + \frac{L_{i+1-}}{k_{i+1} A_{i+1-}} \right)} \tag{4.24}$$

$$\Delta P_i^{sl} = \Delta P_{i-}^{sl} + \Delta P_{i+}^{sl} = \Delta P_{i-1/2} \frac{\frac{L_{i-}}{k_i A_{i-}}}{\left(\frac{L_{i-}}{k_i A_{i-}} + \frac{L_{i-1+}}{k_{i-1} A_{i-1+}} \right)} + \Delta P_{i+1/2} \frac{\frac{L_{i+}}{k_i A_{i+}}}{\left(\frac{L_{i+}}{k_i A_{i+}} + \frac{L_{i+1-}}{k_{i+1} A_{i+1-}} \right)} \tag{4.25}$$

In model calibration of reservoir models, grid cell sensitivity is required to update grid cell reservoir properties. To get the grid cell sensitivity, all streamlines that are reached at

well p are considered and their sensitivities along each streamline are weighed by the flux ratio based on the streamlines passing through the i-th grid cell as in equation (4.26).

$$\frac{\partial \Delta P_{i,p}}{\partial k_i} = \sum_{k=1}^{\substack{\text{all sl pass through} \\ \text{i-th grid, p}}} \left(\frac{q_{\text{along the single sl, j}}}{\sum_{j=\text{all sl to the well p}} q_{sl,j}} \frac{\partial \Delta P_i^{sl}}{\partial k_i} \right) \tag{4.26}$$

The bottom-hole pressure sensitivity calculation depends on the boundary conditions of each well pair. Equation (4.16) is the bottom-hole pressure sensitivity if either of one well has a pressure constraint. When we have rate constraints for both wells that streamlines connect, the bottom-hole pressure sensitivity is calculated as in equation (4.27) by modifying the sensitivity of pressure-rate constraint.

$$\left.\frac{\partial P_{bhp}^{prod}}{\partial k_i}\right|_{rate \leftrightarrow rate} = \left.\frac{\partial P_{bhp}^{prod}}{\partial k_i}\right|_{pressure \leftrightarrow rate} \frac{\tau_i}{\tau_{total}} \tag{4.27}$$

where P_{bhp}^{prod} is the bottom-hole pressure at a producer, τ_{total} is the total time of flight between well pair, and τ_i is the time of flight from injector to grid cell i. Detailed explanation and validation can be found in previous research (Tanaka et al. 2015, Kam, Han, and Datta-Gupta 2017).

4.3.4. Analytical Basis Coefficient Sensitivity

A multi-scale and smooth reservoir property update is possible by sequentially including higher frequency basis functions and their coefficient sensitivities. The analytical basis coefficient sensitivity is derived in this subsection, combined with

streamline-based analytical sensitivity shown in the previous subsection. The re-parameterization of a reservoir property field is performed as in equation (4.28).

$$u = \Phi v \tag{4.28}$$

where u is the n-component column vector of a re-parameterized reservoir property field, v is m-component column vector of parameters in transform domain, and Φ is the predefined $n \times m$ matrix with columns of interpolation or transformation basis vectors. The basis coefficient sensitivity with respect to any production data (ξ) is calculated as in equation (4.29) by chain rule using analytical streamline-based sensitivity.

$$\frac{\delta \xi}{\delta v_i} = \frac{\delta \xi}{\delta k}\frac{\delta k}{\delta v_i} \approx \frac{\delta \xi}{\delta k}\frac{\delta\left[\sum_{j=1}^{m} \Phi_j v_j\right]}{\delta v_i} = \frac{\delta \xi}{\delta k}\Phi_i \tag{4.29}$$

where v_i is the i-th basis coefficient, k is the permeability field whose low rank approximation can be represented by $\sum_{j=1}^{m} \Phi_j v_j$. The level of approximation is controlled by the number of basis functions (m). $\frac{\delta \xi}{\delta k}$ is the analytical streamline-based sensitivity which is easily calculated after a single forward reservoir simulation. Therefore, the basis coefficient sensitivity can be analytically computed by multiplying the streamline-based sensitivity with the corresponding basis function. Note that the dimensions of $\frac{\delta \xi}{\delta k}$ and Φ_i are $1 \times n$ and $n \times 1$ respectively, therefore $\frac{\delta \xi}{\delta k}\Phi_i$ is a scalar value for each coefficient.

The linear equation for permeability update based on streamline-based sensitivity is written in equation (4.30), where $\boldsymbol{S}_k$ is the sensitivity matrix ($D \times n$), $\delta \boldsymbol{k}$ is the column

vector for required permeability changes ($n \times 1$), and $\delta \boldsymbol{d}$ is the column vector for data misfits ($D \times 1$). D is the number of observed data for history matching.

$$\boldsymbol{S}_k \delta \boldsymbol{k} = \delta \boldsymbol{d} \tag{4.30}$$

On the other hand, the linear equation for basis coefficient update is written in equation (4.31), where $\boldsymbol{S}_v$ is the sensitivity matrix ($D \times m$), $\delta \boldsymbol{v}$ is the column vector for required basis coefficient changes ($m \times 1$). Updated basis coefficients are utilized to update a permeability field with equation (4.28), enabling a multi-scale and smooth property changes.

$$\boldsymbol{S}_v \delta \boldsymbol{v} = \delta \boldsymbol{d} \tag{4.31}$$

The impact of the number of basis coefficients on the property change during calibration is shown in Figure 4.8. It shows the property changes after a single iteration with the same initial property and data misfits. As clearly seen in Figure 4.8, more inclusion of basis functions makes the property change closer to the streamline-based change. Hence, we first carry out pressure history matching by including a small set of low frequency basis functions in order to calibrate the large scale property. As demonstrated in Figure 4.8, more inclusion of higher frequency basis functions enables sequential refinement of spatial property changes.

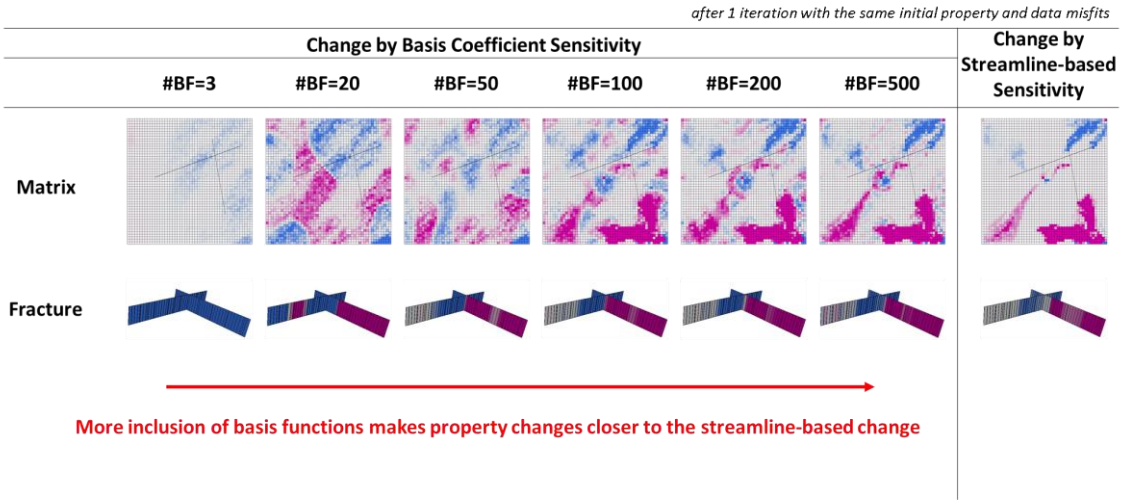

Figure 4.8 Impact of the number of basis coefficients on the property change, compared with streamline-based method

4.3.5. Hierarchical Multi-Scale History Matching Formulation

In this chapter, the main production data to which we calibrate a permeability field are well water cut and bottom-hole pressure. Vasco, Keers, and Karasaki (2000) noted that pressure data is less affected by tracer dispersion and fractional flow properties. These small-scale property variations rather influence water cut data. Therefore, a hierarchical history matching workflow is proposed, where we first start with a large scale reservoir model calibration to pressure data, followed by a small scale calibration to water cut only or also to pressure data further if necessary. Bhark et al. (2012) proposed a multi-scale history matching workflow for bottom-hole pressure and water cut together, utilizing GCT and calculating parameter sensitivity by adjoint method. In their large scale calibration, a reservoir property multiplier field is parameterized and the inversion process is iterated by sequentially including additional parameters (basis coefficients), thus enabling a

refinement of the re-parameterized multiplier field. It was designed to adaptively update spatial details in the reservoir model until the re-parameterization scales are reached to the level at which the history matching is no longer improved by further refinement. They showed with several field cases that history matching is successful only if it begins from the low resolution.

We propose a hierarchical multi-scale history matching workflow for EDFM as in Figure 4.9. In the large scale calibration, we follow the adaptive multi-scale history matching (Bhark, Jafarpour, and Datta-Gupta 2011, Bhark et al. 2012, Bhark, Jafarpour, and Datta-Gupta 2011, Bhark et al. 2011) by sequential refinement of permeability multiplier field with the extended ABT, mainly focusing on the pressure data match. It is because the pressure data is more sensitive to large scale reservoir property than to small scale parameters. The basis coefficient sensitivity is calculated from the streamline-based sensitivity, which is more amenable than the adjoint method in that we are efficiently able to compute it only with simulation results and an access to simulator's source codes is not required. Note that the basis functions are computed only once and are not updated during iterations. If the large scale calibration meets the stopping criteria (maximum number of basis functions included, or no more data misfit reduction), a small scale calibration follows with streamline-based inversion workflow focusing more on water cut data match or also pressure data further if necessary. Note that in both calibration steps a pre-process of EDFM simulation should be performed after every property update, in order to calculate connectivity and transmissibility of matrix-fracture and fracture-fracture interactions.

(a)

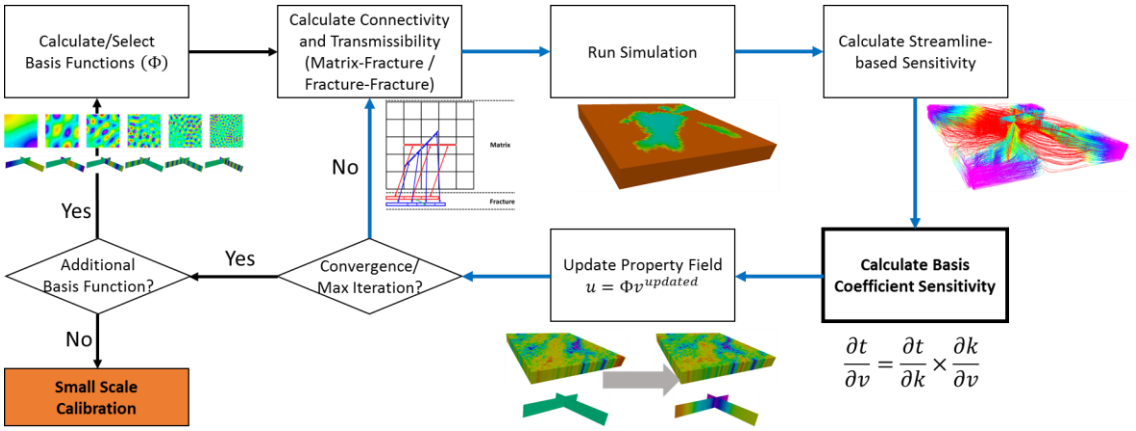

(b)

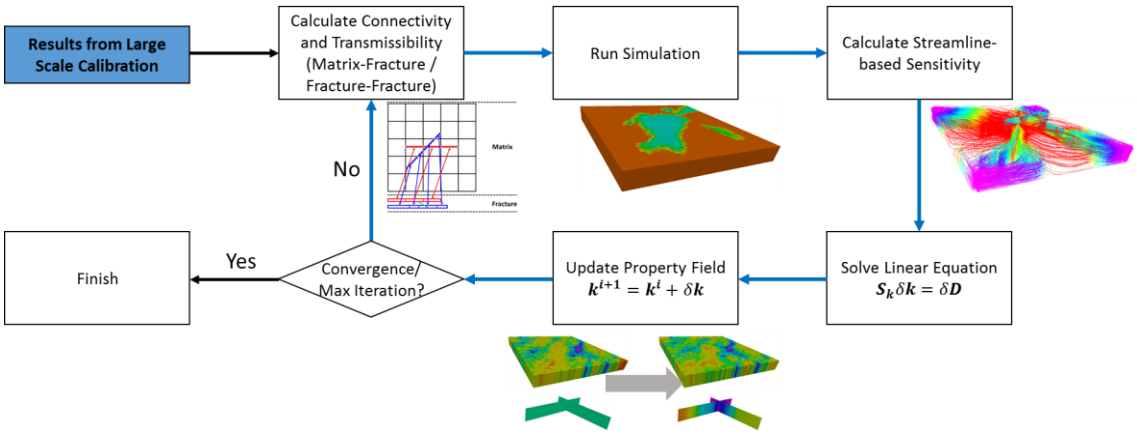

Figure 4.9 Hierarchical EDFM history matching workflow. (a) Large scale calibration with an adaptive multi-scale re-parameterization. (b) Small scale calibration with a streamline-based inversion

4.4. Applications

In this section, we demonstrate the power and efficacy of our proposed parameterization and hierarchical multi-scale history matching workflow with two-dimensional synthetic and field scale EDFM's. First in a synthetic example, we illustrate the effectiveness and validation of the proposed workflow by comparing the history matching results with the conventional streamline-based inversion. We show its effectiveness and practical feasibility further by history matching of a field example with complex fault structure, channels, and dominant natural fractures.

4.4.1. Synthetic Case – Comparison With Streamline-Based Inversion

We compare the history matching results of the proposed parameterization and hierarchical workflow with the results from a conventional streamline-based inversion method. The model is composed of 50×50 matrix grid cells and two embedded fractures as shown in Figure 4.10. It shows the comparison between the initial model and the reference model for matrix and fracture permeabilities, respectively. The history matching is carried out from the initial model (Figure 4.10(a) and (c)). The observed data are reproduced by the reference model (Figure 4.10(b) and (d)). Note that the reference permeabilities for fracture as well as matrix are heterogeneous. The reservoir oil is produced by an inverted 5-spot pattern for 50 months. Four producers are controlled by total liquid rates and an injector is constrained by bottom-hole pressure. We calibrate matrix and fracture permeabilities to water cut and bottom-hole pressure of the producers.

The detailed model descriptions and history matching parameters are summarized in Table 4.2.

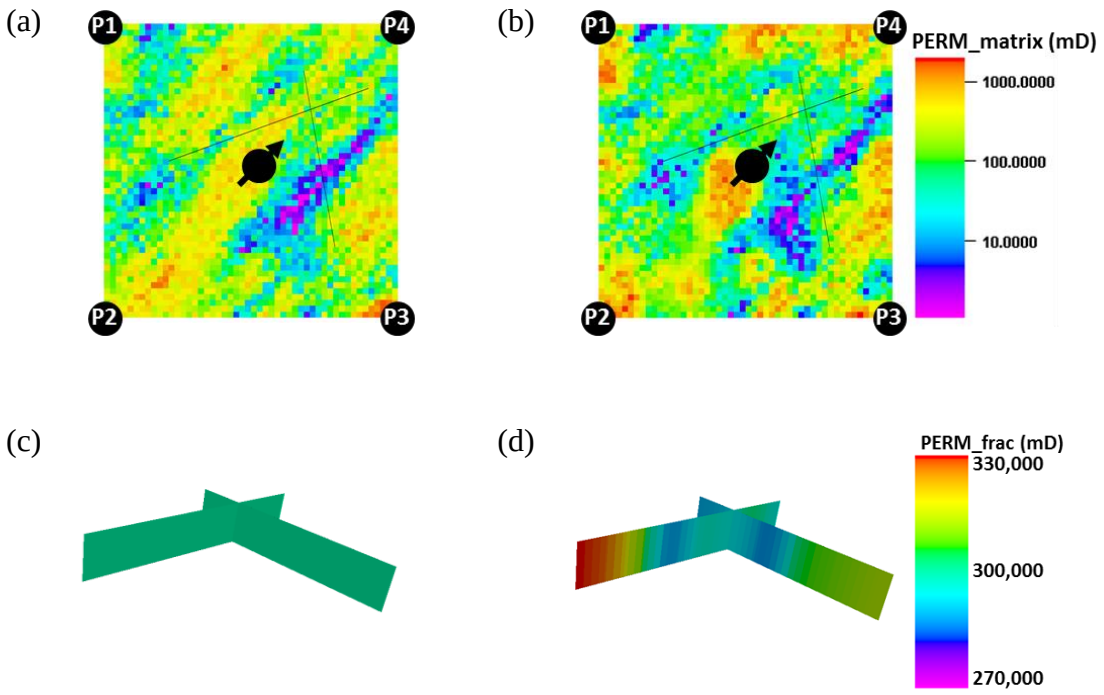

Figure 4.10 Permeability fields for a synthetic EDFM. (a) Matrix permeability of the initial model. (b) Matrix permeability of the reference model. (c) Fracture permeability of the initial model. (d) Fracture permeability of the reference model

Table 4.2 Model descriptions and history matching parameters in a synthetic EDFM. Streamline-based inversion and the proposed hierarchical workflow are compared

Phases	Oil and water
Matrix Grid	$50 \times 50 \times 1 = 2,500$
Number of Embedded Fractures	2
Well	4 producers / 1 injector
History Period	50 months
Constraint	Producer: Total liquid rates Injector: Bottom-hole pressure
Objective Function	Water cut misfit, Bottom-hole pressure misfit
Inversion Method	Streamline-based Vs. Hierarchical workflow

Normalized data misfits for bottom-hole pressure and water cut (generalized travel time and amplitude) are shown in Figure 4.11. In hierarchical multi-scale workflow, large scale calibration to BHP data is performed four times with basis coefficient sensitivity, beyond which match quality is not improved further. Small scale inversion is carried out by the joint sensitivities for BHP and WCT, based on streamlines through all iterations. The water cut misfit for both methods is computed by 'generalized travel time' to reduce the non-linearity (Kam and Datta-Gupta 2016). The amplitude water cut misfit is also computed for reference as in Figure 4.11(c).

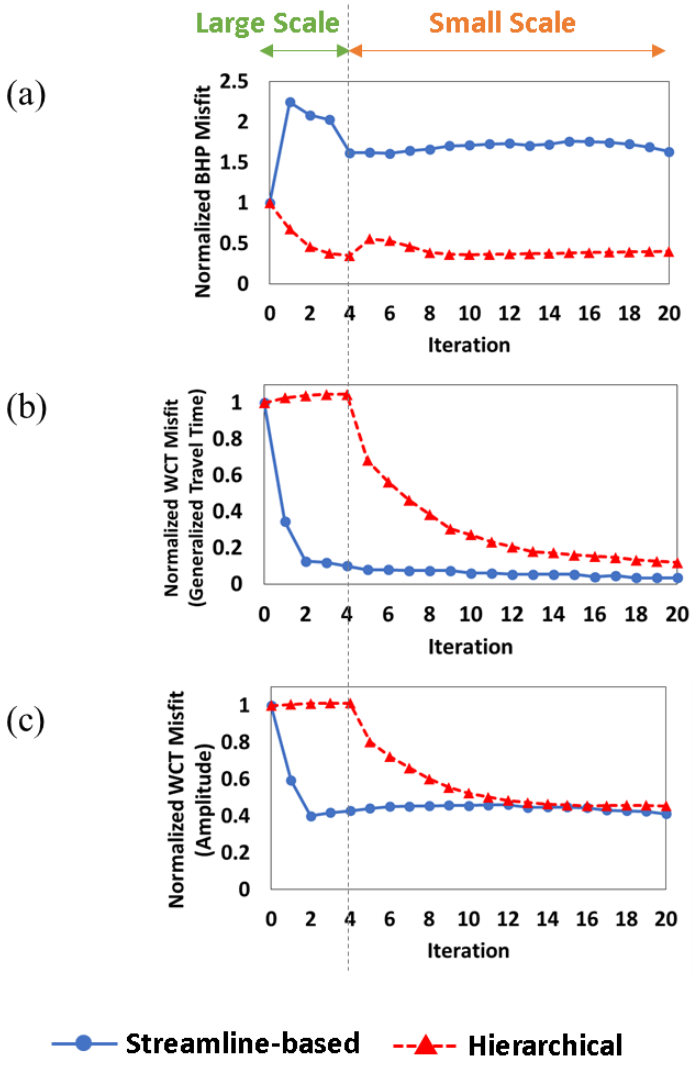

Figure 4.11 Normalized data misfit reduction by streamline-based inversion and hierarchical workflow respectively in synthetic EDFM. (a) BHP misfit. (b) WCT misfit (generalized travel time). (c) WCT misfit (amplitude)

While significantly reducing WCT misfit after two iterations, the streamline-based inversion increased BHP misfit to more than double. Further iterations after this could not improve both BHP and WCT match. It is caused by the fact that it tries to calibrate small

scale grid cell permeability to match BHP and WCT at the same time, resulting in a local minima with small WCT misfit. Therefore, further iterations could not improve the match results. However, the large scale calibration in a hierarchical workflow significantly reduced BHP misfit with slight increase of WCT misfit. Continuing with the small scale calibration gradually reduced WCT misfit, to the same degree as the streamline-based inversion after 20 iterations. The match results are improved by calibrating permeability field in a large scale first to match the energy in the reservoir and distributing saturations through small scale updates. In other words, the large scale calibration helps the solution not to be trapped in a local minima.

Figure 4.12 shows match results for both the methods along with the observed data. Both streamline-based inversion and the hierarchical workflow have improved WCT match to the similar degree, compared to the initial model as in Figure 4.12(a). However, the streamline-based inversion has deteriorated BHP match especially on producers ‘P1’ and ‘P4’. The match results after the hierarchical workflow, on the other hand, have been significantly improved for every producers as in Figure 4.12(b).

(a)

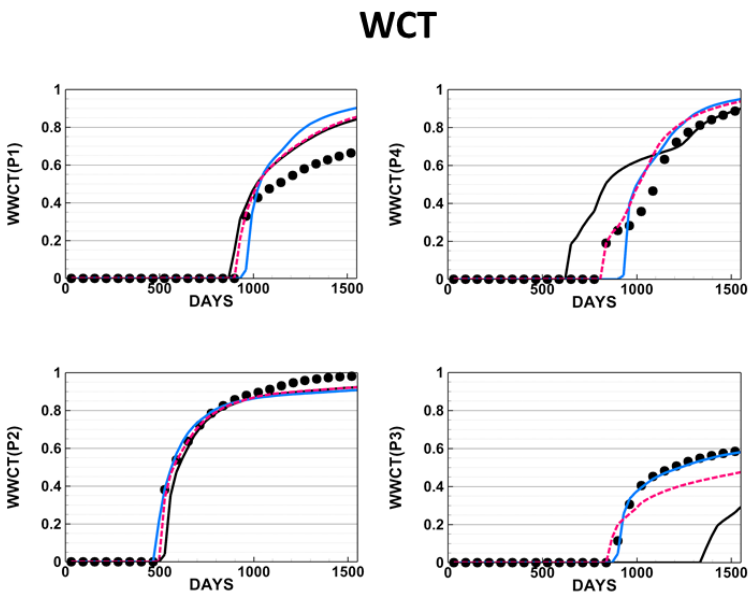

(b)

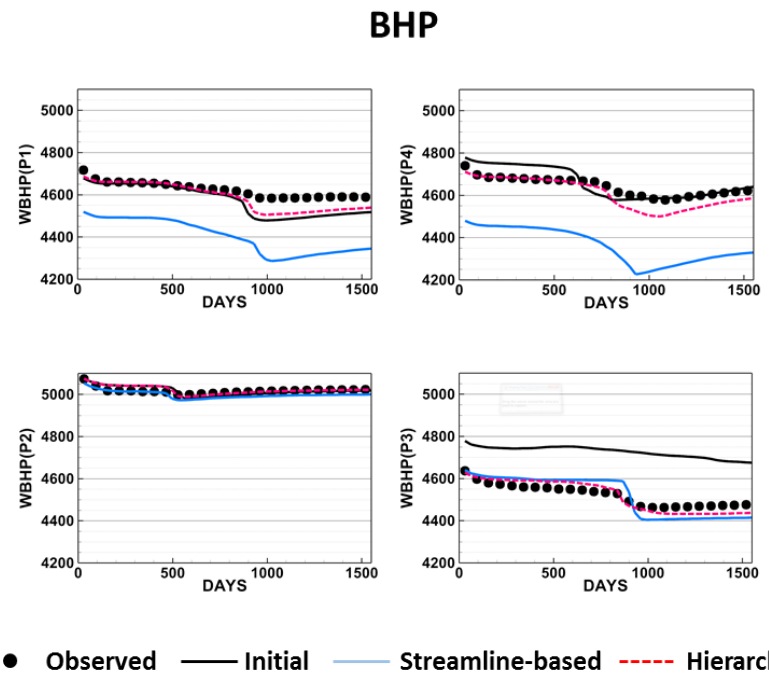

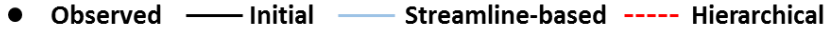

Figure 4.12 Match results after streamline-based inversion and hierarchical workflow for (a) WCT and (b) BHP in synthetic EDFM

Updated permeability fields after history matching are compared with the initial and reference models in Figure 4.13. It is difficult to decide based on Figure 4.13 whether the permeability field is updated in the correct direction because of the large heterogeneity. Therefore, permeability changes are compared with the required change ($= reference\ permeability - initial\ permeability$) in Figure 4.14. Note that the permeability change after large scale calibration has geologically smooth and large trend. It is because the property field is updated not by streamline-based grid cell sensitivity, but by basis coefficient sensitivity of large scale basis functions. The gray circles on the permeability change after small scale calibration in Figure 4.14 represent the regions that have the same trend with the required change. Of these regions, green check marks are given if the trend is the same as the one from the streamline-based inversion. Therefore, the rest of circled regions (with red arrows) contributes to BHP match mainly resulting from the large scale calibration.

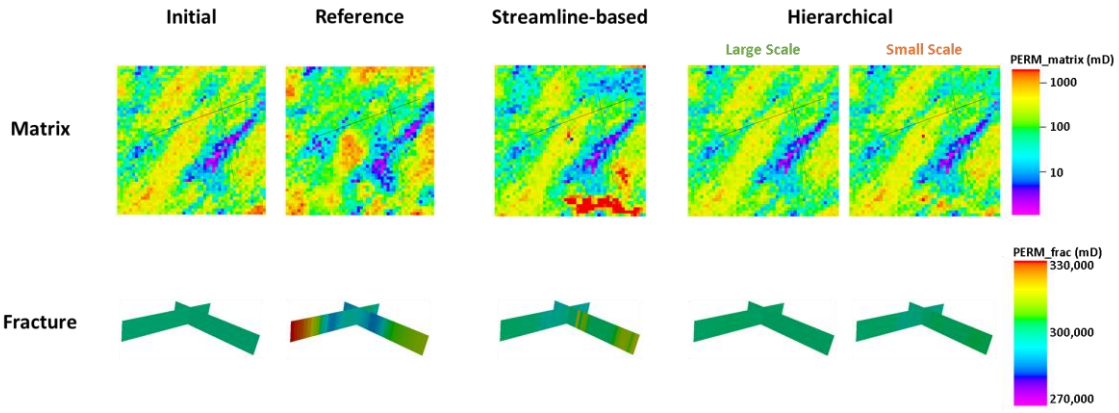

Figure 4.13 Updated permeability fields after history matching, compared with initial and reference models of synthetic EDFM

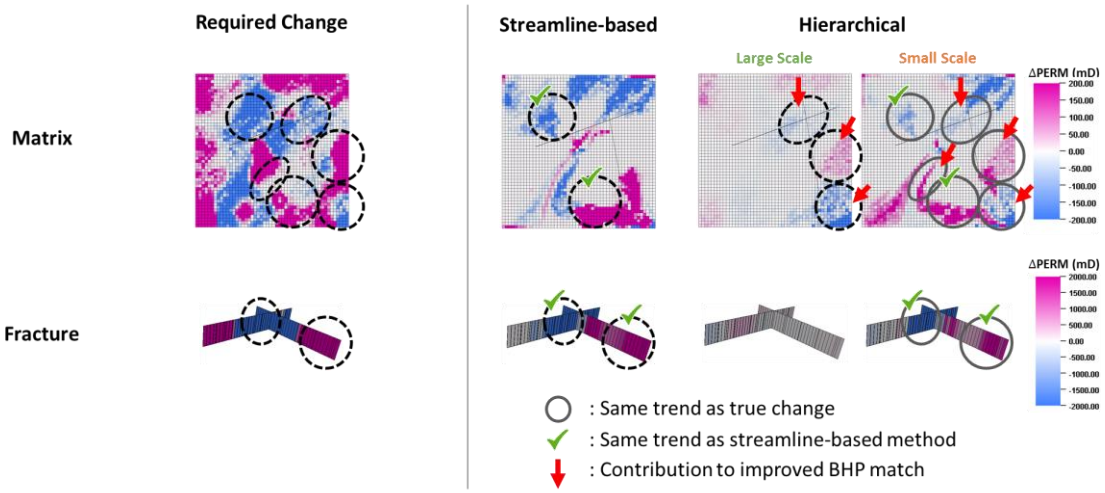

Figure 4.14 Permeability changes after history matching, compared with the required change of synthetic EDFM

Streamlines are compared after history matching with the initial and reference models in Figure 4.15. The first row shows the time of flights from producers and second row shows the producer drainage volume partition, respectively. Since we have the

reference model and true flow properties, it is possible to select the better calibrated region based on the flow diagnostics. The regions with gray circle have more similar trends to the reference case than the flow properties from the model after streamline-based inversion.

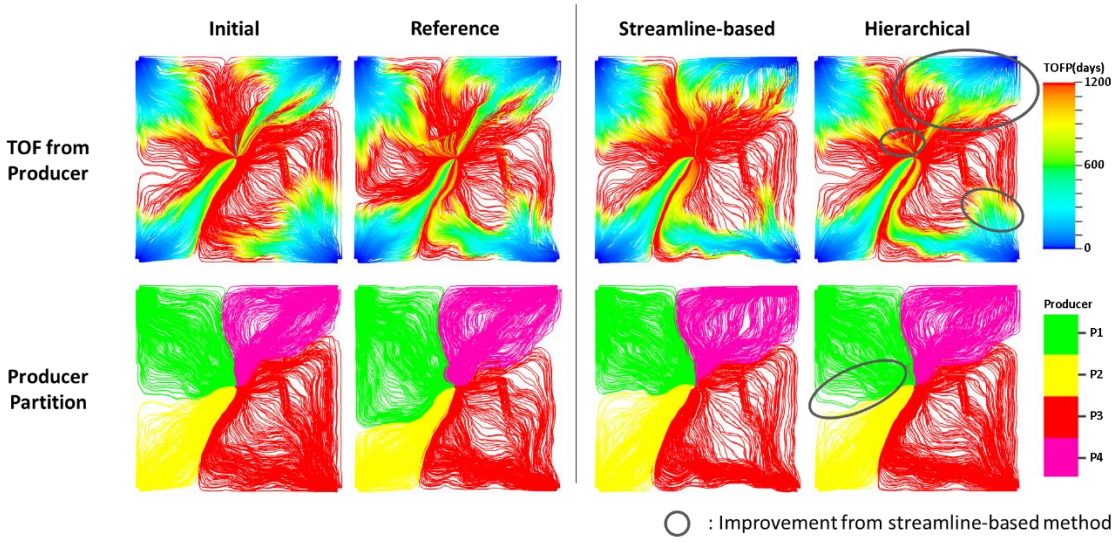

Figure 4.15 Comparison of streamlines after history matching along with initial and reference models of synthetic EDFM. First row shows the time of flights from producer and second row shows the producer drainage volume partitions

Based on the comparisons of data misfit, match results, permeability change, and flow diagnostic, it is demonstrated that the hierarchical multi-scale history matching workflow is more effective than the conventional streamline-based inversion method for the calibration of EDFM.

4.4.2. Field Case – Reservoir With Faults / Fractures

We apply the proposed parameterization method and the hierarchical multi-scale history matching workflow to a field scale reservoir model with complex faults, channels, and fractures. It was made for the 'Sensitivity Analysis of the Impact of Geological Uncertainties Project (SAIGUP)' (Manzocchi et al. 2008). Seven large fractures are embedded by EDFM construction shown in Figure 4.16, along with initial rock and fluid distributions. The reservoir oil is produced by peripheral water injection during 15 years. Ten producers are controlled by total liquid rates and eleven injectors are constrained by bottom-hole pressure. We calibrate matrix and fracture permeabilities to water cut and bottom-hole pressure of the producers. The detailed model descriptions and history matching parameters are summarized in Table 4.3.

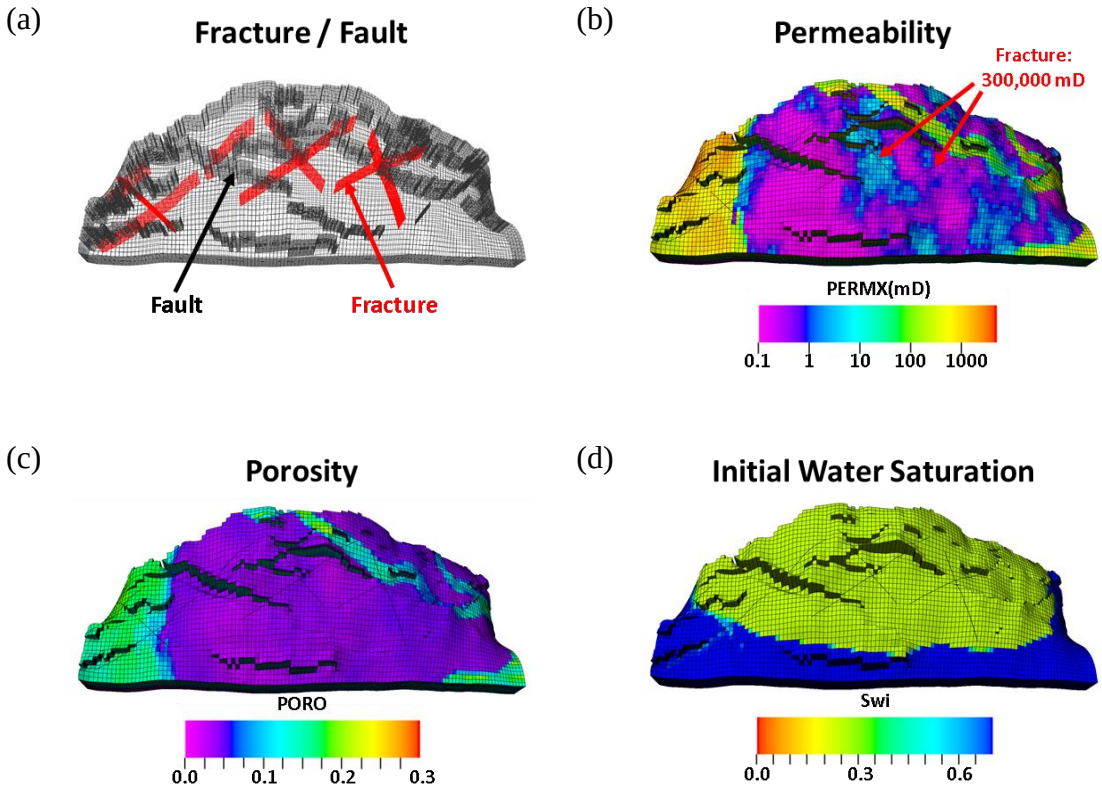

Figure 4.16 Initial rock and fluid distributions in SAIGUP EDFM. (a) Grid structure with fractures and faults. (b) Initial permeability field. (c) Porosity field. (d) Initial water saturation distribution

Table 4.3 Model descriptions and history matching parameters in SAIGUP EDFM

Phases	Oil and water
Matrix Grid	$40 \times 120 \times 20 = 96,000$
Number of Embedded Fractures	7
Well	10 producers / 11 injector
History Period	15 years
Constraint	Producer: Total liquid rates Injector: Bottom-hole pressure
Objective Function	Water cut misfit, Bottom-hole pressure misfit
Inversion Method	Hierarchical workflow

Basis functions are calculated by the extended ABT and shown in Figure 4.17. It shows basis functions on the matrix and the fracture plane in the left and right columns respectively. Transparent views are also shown in the middle column to observe the distinct features between matrix and fractures.

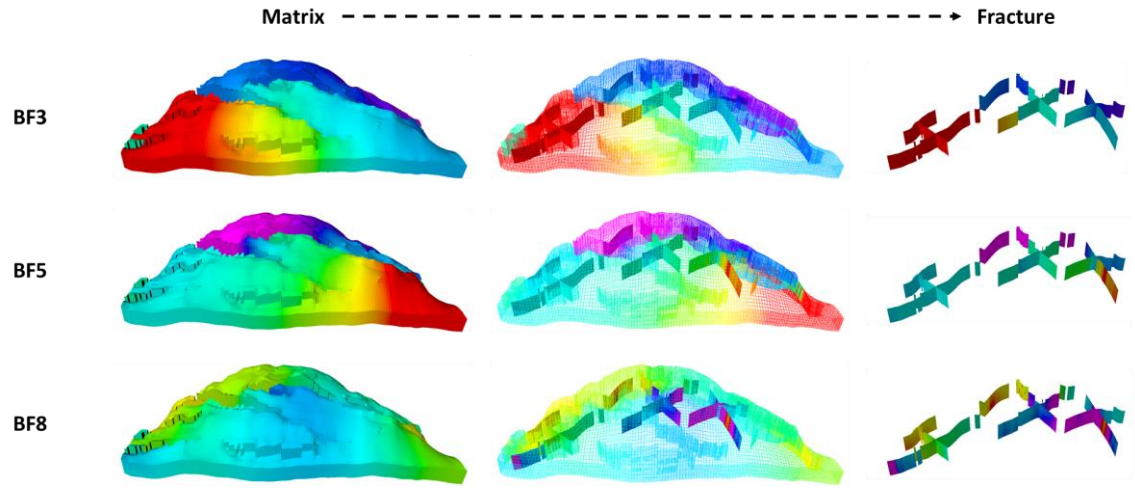

Figure 4.17 Basis functions of SAIGUP EDFM calculated by the extended ABT. Left column shows values on matrix. Right column shows values on fracture planes. Middle column shows the transparent view to observe the distinct features between matrix and fractures

Normalized data misfits for bottom-hole pressure and water cut (generalized travel time and amplitude) are shown in Figure 4.18. The large scale calibration to BHP data with basis coefficient sensitivity is performed three times, followed by small scale streamline-based inversion for WCT data. The large scale calibration significantly reduced BHP misfit accompanying small decrease of WCT misfit (generalized travel time) and small increase of WCT misfit amplitude. The following small scale calibration could gradually reduce WCT misfit.

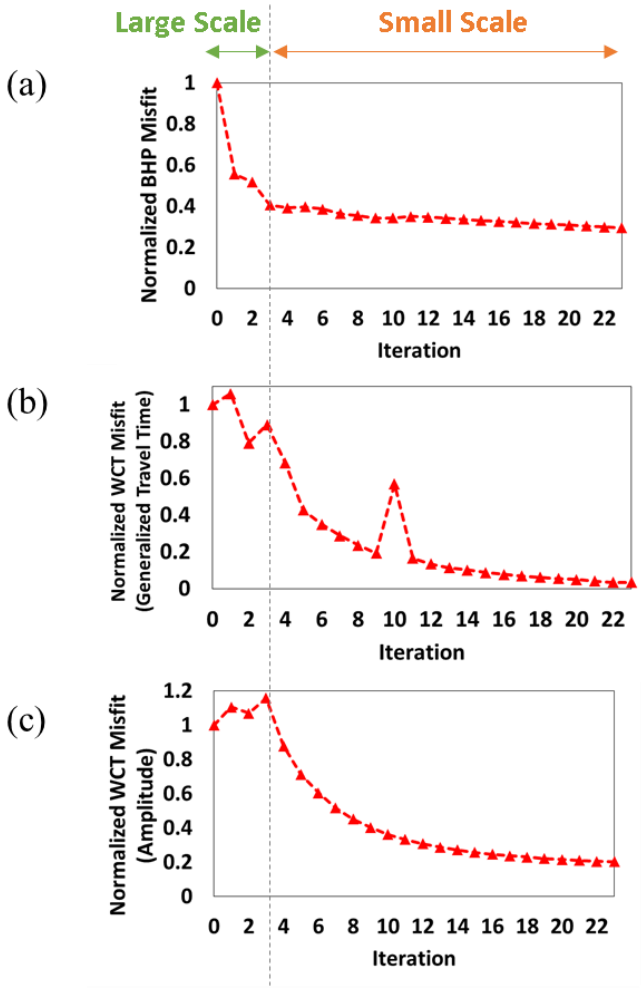

Figure 4.18 Normalized data misfit reduction by hierarchical workflow in SAIGUP EDFM. (a) BHP misfit. (b) WCT misfit (generalized travel time). (c) WCT misfit (amplitude)

Figure 4.19 shows match results after the hierarchical history matching workflow along with the observed data and initial simulation results. Both water cut and bottom-hole pressure match were significantly improved for every producers. It is attributed to the proposed effective parameterization method and multi-scale calibrations. It calibrated permeability field in the large scale first to match the energy in reservoir and distributed

fluid saturations into each producers through small scale updates. It clearly shows practical feasibility of the proposed approach through the field scale EDFM with complex geological structures.

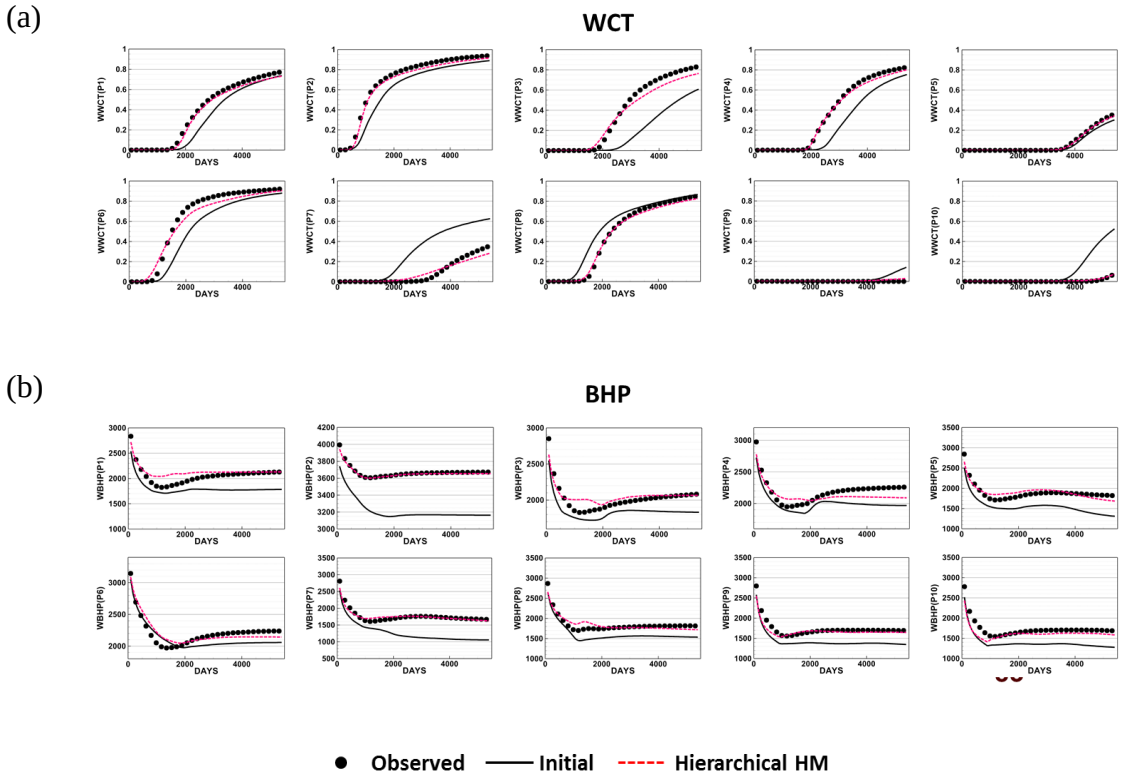

Figure 4.19 Match results after the hierarchical history matching for SAIGUP EDFM, along with the observed data and initial simulation results for (a) WCT and (b) BHP

Updated matrix permeability field after history matching are shown for each layers in Figure 4.20(b), along with the initial model in Figure 4.20(a). Figure 4.21 shows the

matrix permeability changes ($= updated\ permeability - initial\ permeability$) after history matching, where most of changes are located within layer 1 – layer 10. Green dotted circles represent the permeability changes calibrated by the small scale calibration. Note that the permeability change in the large scale calibration is along the geological structure, while the small scale calibration changed the model along the streamlines and around wells.

(a)

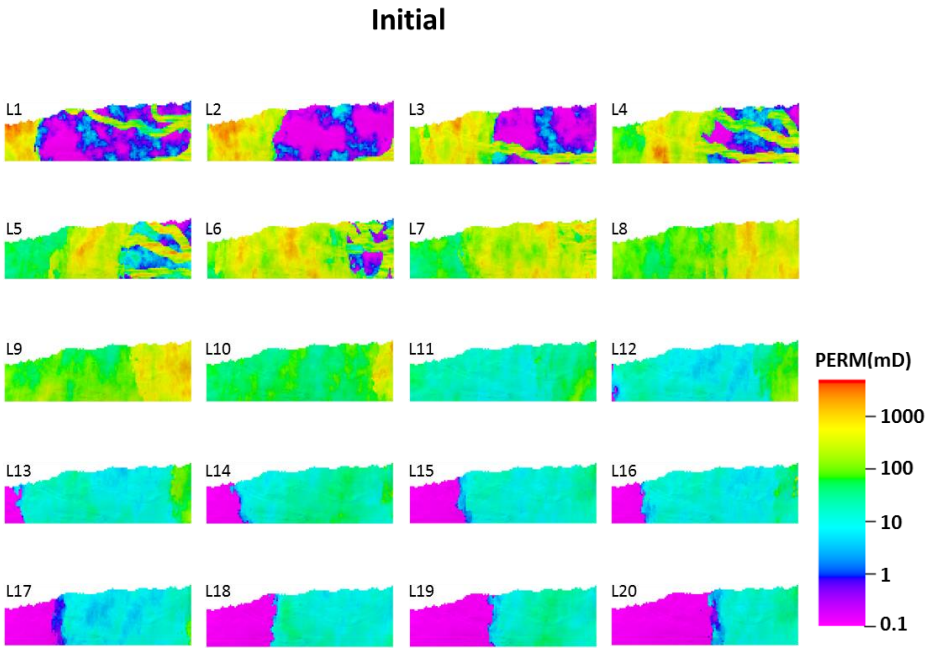

(b)

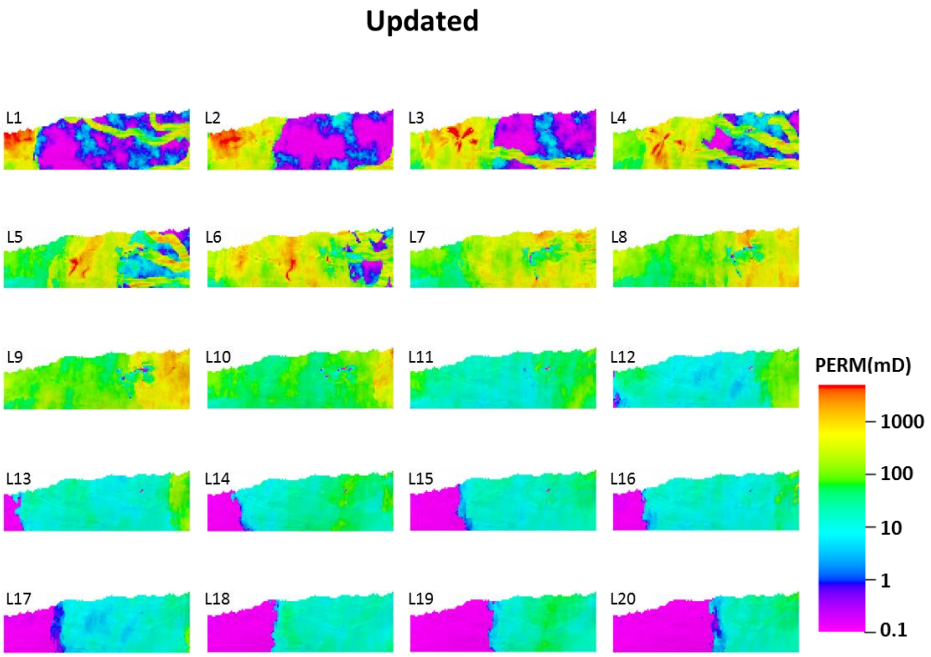

Figure 4.20 SAIGUP EDFM. (a) Initial matrix permeability field. (b) Updated matrix permeability filed after history matching for each layers

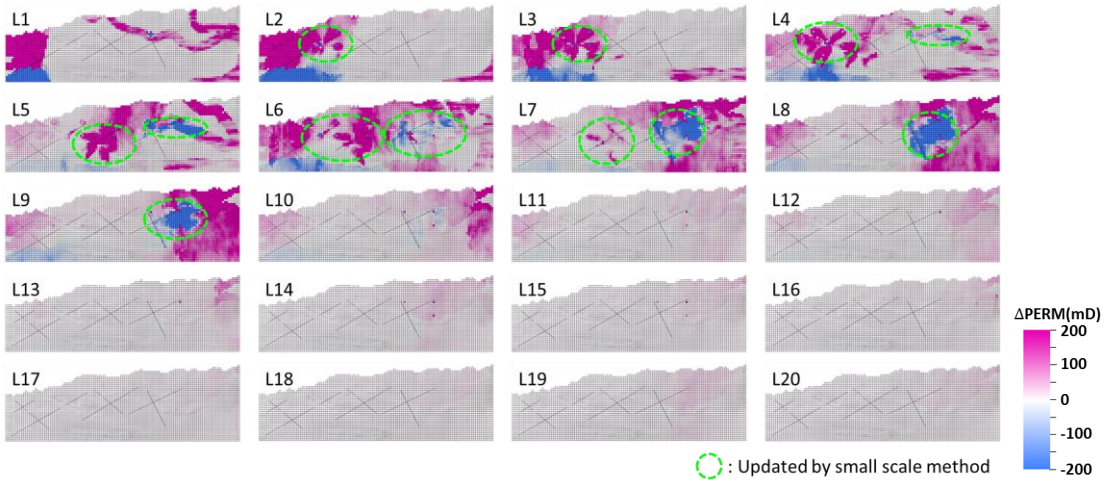

Figure 4.21 Matrix permeability changes after history matching in SAIGUP EDFM. Green dotted circles represent permeability updates by small scale calibration

Updated fracture permeability and its change are shown in Figure 4.22. Green dotted circles again represent the permeability changes calibrated by the small scale calibration. It is obvious that the small scale calibration changed fracture permeability along the streamlines.

(a)

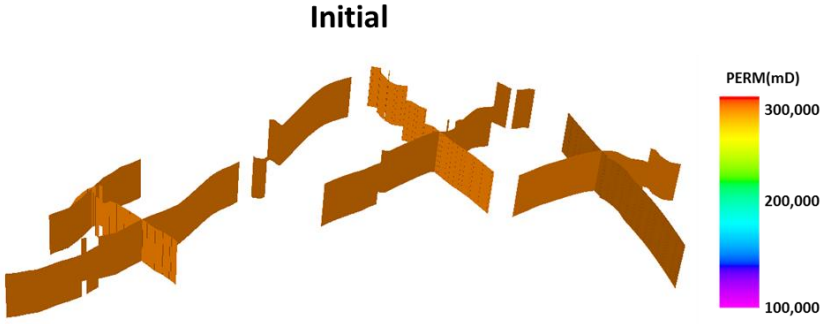

(b)

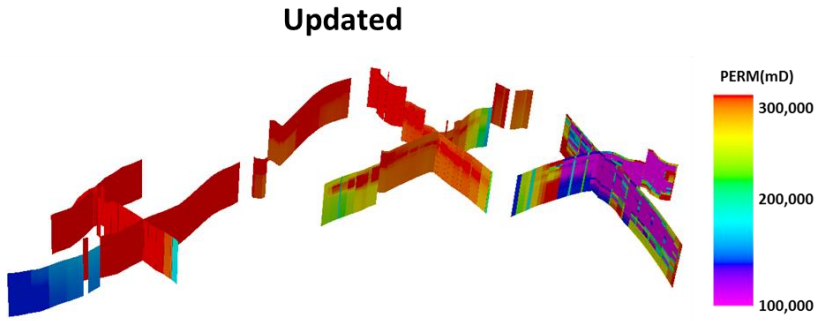

(c)

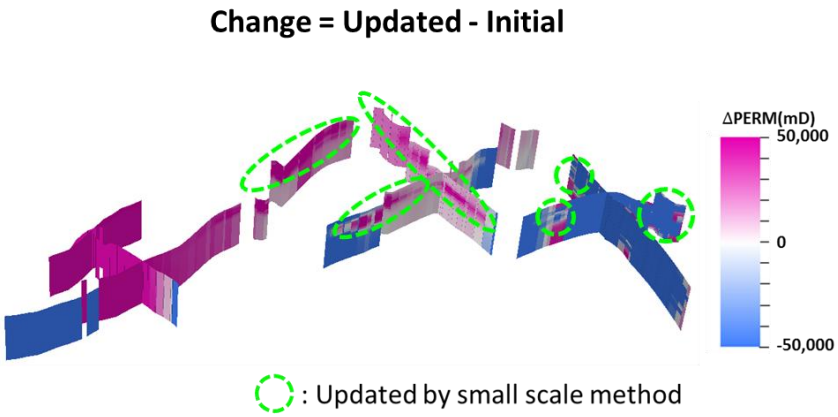

Figure 4.22 SAIGUP EDFM. (a) Initial fracture permeability. (b) Updated fracture permeability after history matching. (c) Fracture permeability change after history matching. Green dotted circles represent permeability updates by small scale calibration

We also examined the change of streamlines after history matching in Figure 4.23, compared with the initial model. The first row shows the time of flights from producers and second row shows the producer drainage volume partition, respectively. It is clearly seen that the flow patterns are changed after history matching.

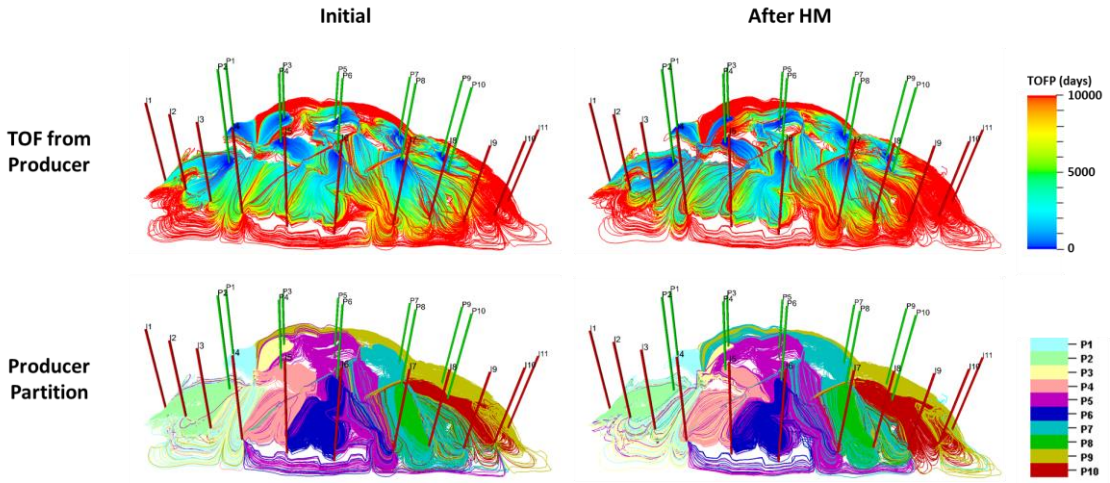

Figure 4.23 Comparison of streamlines after history matching with initial model of SAIGUP EDFM. First row shows the time of flights from producer and second row shows the producer drainage volume partitions

In order to explain the improved match results by flow diagnostics, streamlines from producer 'P10' are shown as an example in Figure 4.24. Even though streamline trajectories are similar to each other, it shows different flow properties before and after history matching. First row shows the time of flights from 'P10' and WCT match results. Compared to the initial model, history matched model has smaller drainage volume despite the same liquid production rate (constraint). It means that the pressure drawdown around 'P10' changed to be smaller after history matching. The change of flow pattern explains the delayed water breakthrough in the updated model compared to the initial model and hence the improved match WCT match. Improvement is noted as a green dotted arrow in the water cut response graph. Second row shows the pressure distribution along the streamlines. The pressure around 'P10' changed to be higher than the initial model after history matching. The pressure increase explains how we could get the improved

BHP match. In this way, we are able to utilize the streamlines for flow diagnostic as well as for the hierarchical multi-scale history matching combined with the extended ABT basis functions.

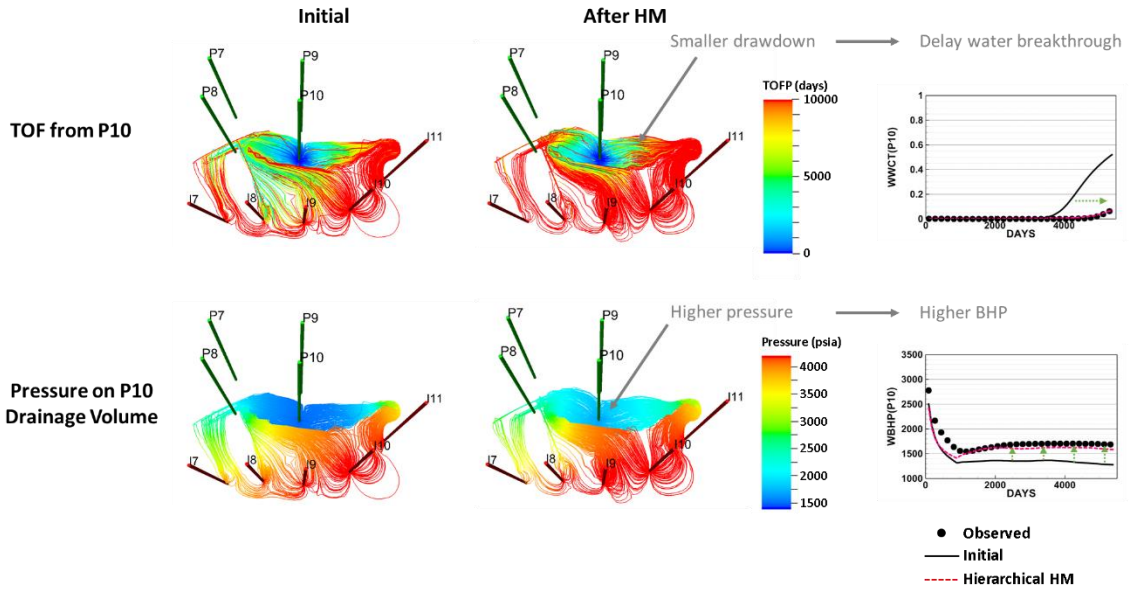

Figure 4.24 Streamlines from producer 'P10' in SAIGUP EDFM. First row shows the time of flight from 'P10' and WCT match of 'P10'. Second row shows the pressure distribution along the streamlines and BHP match of 'P10'. Both rows compare the properties and match results between the initial model and history matched model

4.5. Conclusions

In this chapter, we have extended adjacency-based transform to parameterize embedded discrete fracture model for efficient history matching of reservoir models with fractures. As fracture domain is connected to matrix domain by non-neighbor connections and they have significant property difference in EDFM, both grid connectivity information and property difference are considered in Laplacian construction. Therefore, the proposed method can effectively parameterize EDFM, both for matrix and fractures.

We have also proposed a hierarchical multi-scale history matching workflow for EDFM. In the large scale calibration, basis coefficient sensitivity to production data is analytically computed based on streamline-based sensitivity in order to calibrate EDFM to pressure data, which is more affected by large scale parameters. The inversion process is iterated by sequentially including additional basis coefficients of higher frequency. It enables a refinement of the re-parameterized multiplier field until the re-parameterization scales are reached to the level at which the history matching is no longer improved by further refinement. The large scale calibration is followed by small scale calibration where streamline-based sensitivity is utilized to match saturation data by updating grid cell properties.

In two-dimensional synthetic EDFM case, we demonstrated the power and efficacy of the extended ABT parameterization by efficient compression performance both on matrix and fracture domains. The proposed hierarchical workflow showed improved match results than the conventional streamline-based inversion. The match quality is determined by data misfits, simulation results compared to the observed data, permeability

change, and flow diagnostics by streamlines. In field scale EDFM case with complex fault structure, channels, and fractures, the proposed parameterization and hierarchical history matching workflow could efficiently reduce both water cut and bottom-hole pressure misfits. Through successful field scale EDFM history matching, we clearly showed its effectiveness and practical feasibility.

The parameterization of EDFM enables to represent important geological trend and fracture properties with significantly reduced number of parameters. The hierarchical model calibration method combined with the proposed parameterization facilitates the efficient history matching for the fractured reservoirs.

5. CONCLUSIONS AND RECOMMENDATIONS

5.1. Conclusions

In this study, we developed, validated, and applied novel model parameterization methods for efficient history matching of conventional and unconventional reservoirs. The spatial property distribution of reservoir model is transformed into a few parameters in the spectral domain with appropriate basis functions. The parameters in the spectral domain are then updated during model calibration. Substantially reduced number of unknown parameters regularizes the ill-posed history matching problem, and addresses the non-uniqueness and stability issues. The novelty of this study is the basis formulation for various reservoir models, data types, and data resolution to achieve efficient history matching. The conclusions of this study are summarized as follows:

- We proposed a novel approach to integrate frequent time lapse seismic data into high resolution reservoir models based on seismic onset times. The ABT parameterization was used to simultaneously reconcile the model heterogeneity by compressing multiple seismic surveys into a single map of onset times that represents the propagation of changes in the reservoir. The Peace River application demonstrated the feasibility and the robustness of the history matching workflow (MOGA with ABT) to integrate onset times and pressure data. Our approach updated the parameters simultaneously, which allows testing different combinations of parameters uncertainty range.

- We introduced a novel multi-resolution grid connectivity-based transform (MGCT) for more efficient history matching, especially when the production data resolution is variant in a reservoir. The multi-resolution basis vectors are achieved by coarsening the region outside the area of interest (AOI) and eigen-decomposing the corresponding grid Laplacian. By this method, the resolution in the AOI becomes higher at the cost of lower resolution in the coarsened region. Due to the coarsening, it has a smaller Laplacian matrix than GCT, and therefore requires reduced computation time for eigen-decomposition. The more powerful aspect of MGCT is the ability to adjust the modal frequencies or resolutions of basis functions to comply with the various data resolutions. Hence, it better regularizes the underdetermined history matching problem compared to GCT. We showed in the conventional waterflooded reservoir that history matching quality can be improved by the proposed multi-resolution parameterization compared to the uniform-resolution parameterization. We also demonstrated its applicability to history matching of unconventional tight oil reservoir with multi-stage hydraulic fractures.
- We extended adjacency-based transform to parameterize embedded discrete fracture model (EDFM) for efficient history matching of reservoir models with fractures. As fracture domain is connected to matrix domain by non-neighbor connections and they have significant property difference in EDFM, both grid connectivity information and property difference are considered in the Laplacian construction. Therefore, the proposed method can effectively parameterize EDFM,

both for matrix and fractures. We also proposed a hierarchical multi-scale history matching workflow for EDFM. In the large scale calibration, basis coefficient sensitivity to production data is analytically computed using streamline-based sensitivity in order to calibrate EDFM to pressure data, which is more affected by large scale property variations. The inversion process is iterated by sequentially including additional basis coefficients to include higher frequencies. It enables a refinement of the re-parameterized multiplier field until the re-parameterization levels are reached to the level at which the history matching is no longer improved by further refinement. The large scale calibration is followed by the small scale calibration where streamline-based sensitivity is utilized to match saturation data by updating grid cell properties. We demonstrated the power and efficacy of the extended ABT parameterization by efficient compression performance both on matrix and fracture domains. The proposed hierarchical workflow showed much improved match results than the conventional streamline-based inversion. In the field scale EDFM case with complex fault structure, channels, and fractures, the proposed parameterization and hierarchical history matching workflow could efficiently reduce both water cut and bottom-hole pressure misfits. Through successful field scale EDFM history matching, we clearly showed its effectiveness and practical feasibility.

5.2. Recommendations and Future Study

This study can be extended and improved by the following recommendations and future study:

- History matching with parameterization and multi-objective genetic algorithm in this study is carried out with a fixed number of basis functions after re-parameterization analysis. Multi-stage MOGA with sequential inclusion of basis functions would remove subjectivity of the number of basis functions and improve history matching quality.
- In multi-resolution GCT, the area of interest (AOI) is set by qualitative engineering judgement since there is no specific data resolution provided. The definition of AOI by quantitative criteria (data resolution, sensitivity to production data) would improve history matching.
- Hierarchical multi-scale history matching workflow for EDFM is carried out with the fixed fracture geometries. The proposed matrix/fracture property calibration should be preceded by the calibration of fracture distribution and geometries which have high uncertainty. The workflow for the calibration of fracture distribution is recommended in Appendix B.
- There are subjectivities on the weighting functions in the similarity formulation of ABT. Alternative similarity definition by ‘diffusive time of flight’ (DTOF) is proposed in Appendix D, in order to mitigate subjectivity.

REFERENCES

Alcolea, Andrés, Jesús Carrera, Agustín Medina. 2006. Pilot points method incorporating prior information for solving the groundwater flow inverse problem. *Advances in Water Resources* **29** (11): 1678-1689.

Arenas, Eliana, Cor van Kruijsdijk, Tanja Oldenziel. 2001. Semi-automatic history matching using the pilot point method including time-lapse seismic data. Proc., SPE Annual Technical Conference and Exhibition, New Orleans, Louisiana, USA.

Azom, Prince Nnamdi, Farzam Javadpour. 2012. Dual-continuum modeling of shale and tight gas reservoirs. Proc., SPE Annual Technical Conference and Exhibition, San Antonio, Texas, USA.

Behrens, Ronald, Patrick Condon, William Haworth et al. 2001. 4D seismic monitoring of water influx at Bay Marchand: The practical use of 4D in an imperfect world. Proc., SPE Annual Technical Conference and Exhibition, New Orleans, Louisiana, USA.

Bhark, Eric, Behnam Jafarpour, Akhil Datta-Gupta. 2011. An adaptively scaled frequency-domain parameterization for history matching. *Journal of Petroleum Science and Engineering* **75** (3-4): 289-303.

Bhark, Eric, Alvaro Rey, Akhil Datta-Gupta et al. 2012. A multiscale workflow for history matching in structured and unstructured grid geometries. *SPE Journal* **17** (03): 828-848.

Bhark, Eric W, Behnam Jafarpour, Akhil Datta-Gupta. 2011. A generalized grid connectivity–based parameterization for subsurface flow model calibration. *Water Resources Research* **47** (6).

Bhark, Eric Whittet, Akhil Datta-Gupta, Behnam Jafarpour. 2011. History matching with a multiscale parameterization based on grid connectivity and adaptive to prior information. Proc., SPE Annual Technical Conference and Exhibition, Denver, Colorado, USA.

Bhark, Eric Whittet, Alvaro Rey, Akhil Datta-Gupta et al. 2011. Multiscale parameterization and history matching in structured and unstructured grid geometries. Proc., SPE Reservoir Simulation Symposium, The Woodlands, Texas, USA.

Britanak, Vladimir, Patrick C Yip, Kamisetty Ramamohan Rao. 2010. *Discrete cosine and sine transforms: general properties, fast algorithms and integer approximations*, Elsevier (Reprint).

Chai, Z, B Yan, JE Killough et al. 2018. An efficient method for fractured shale reservoir history matching: The embedded discrete fracture multi-continuum approach. *Journal of Petroleum Science and Engineering* **160**: 170-181.

Chai, Zhi, Hewei Tang, Youwei He et al. 2018. Uncertainty quantification of the fracture network with a novel fractured reservoir forward model. Proc., SPE annual technical conference and exhibition, Dallas, Texas, USA.

Chavent, Guy, Robert Bissell. 1998. Indicator for the refinement of parameterization. In *Inverse problems in engineering mechanics*, 309-314. Elsevier.

Chen, Hongquan, Tsubasa Onishi, Feyisayo Olalotiti-Lawal et al. 2018. Streamline tracing and applications in naturally fractured reservoirs using embedded discrete fracture models. Proc., SPE Annual Technical Conference and Exhibition, Dallas, Texas, USA.

Chen, Hongquan, Changdong Yang, Akhil Datta-Gupta et al. 2019. A hierarchical multiscale framework for history matching and optimal well placement for a HPHT fractured gas reservoir, Tarim Basin, China. Proc., International Petroleum Technology Conference, Beijing, China.

Cheng, Hao, Kaveh Dehghani, Travis C Billiter. 2008. A structured approach for probabilistic-assisted history matching using evolutionary algorithms: Tengiz field applications. Proc., SPE annual technical conference and exhibition, Denver, Colorado, USA.

Cho, Yongchae, Jr. Richard L. Gibson, Hyunmin Kim et al. 2019. Time-lapse 3-D seismic wave simulation via the generalized multiscale finite element method. *Communications in Computational Physics*.

Dachanuwattana, Silpakorn, Jianli Jin, Pavel Zuloaga-Molero et al. 2018. Application of proxy-based MCMC and EDFM to history match a Vaca Muerta shale oil well. *Fuel* **220**: 490-502.

Dadashpour, Mohsen, David Echeverría-Ciaurri, Jon Kleppe et al. 2009. Porosity and permeability estimation by integration of production and time-lapse near and far offset seismic data. *Journal of Geophysics and Engineering* **6** (4): 325-344.

Dadashpour, Mohsen, David Echeverria Ciaurri, Tapan Mukerji et al. 2010. A derivative-free approach for the estimation of porosity and permeability using time-lapse seismic and production data. *Journal of Geophysics and Engineering* **7** (4): 351-368.

Dadashpour, Mohsen, Martin Landrø, Jon Kleppe. 2007. Nonlinear inversion for estimating reservoir parameters from time-lapse seismic data. *Journal of Geophysics and Engineering* **5** (1): 54-66.

Datta-Gupta, Akhil, Michael Joseph King. 2007. *Streamline simulation: theory and practice*, Vol. 11, Society of Petroleum Engineers Richardson (Reprint).

Deb, Kalyanmoy, Amrit Pratap. 2002. A fast elitist non-dominated sorting genetic algorithm for multi-objective optimization: NSGA-II. Proc., International conference on parallel problem solving from nature, Berlin, Heidelberg.

Eastwood, John, Pierre Lebel, Andrew Dilay et al. 1994. Seismic monitoring of steam-based recovery of bitumen. *The Leading Edge* **13** (4): 242-251.

Gassmann, Fritz. 1951. Elastic Waves through a Packing of Spheres. *Geophysics* **16** (4): 673-685.

Gonzalez, Rafael C. 2001. Digital Image Processing/Richard E. *Woods. Interscience, NY*.

Grimstad, Alv-Arne, Trond Mannseth, Geir Nævdal et al. 2003. Adaptive multiscale permeability estimation. *Computational Geosciences* **7** (1): 1-25.

Hetz, G, A Datta-Gupta, JK Przybysz-Jarnut et al. 2017. Integration of continuous time lapse seismic data into reservoir models using onset times. EAGE.

Hetz, Gill, Hyunmin Kim, Akhil Datta-Gupta et al. 2017. History matching of frequent seismic surveys using seismic onset times at the Peace River field, Canada. Proc., SPE Annual Technical Conference and Exhibition, San Antonio, Texas, USA.

Iino, Atsushi, Aditya Vyas, Jixiang Huang et al. 2017. Efficient modeling and history matching of shale oil reservoirs using the fast marching method: Field application and validation. Proc., SPE Western Regional Meeting, Bakersfield, California, USA.

Jafarpour, Behnam, Dennis B McLaughlin. 2009. Reservoir characterization with the discrete cosine transform. *SPE Journal* **14** (01): 182-201.

Jahns, Hans O. 1966. A rapid method for obtaining a two-dimensional reservoir description from well pressure response data. *Society of Petroleum Engineers Journal* **6** (04): 315-327.

Jain, Anil K. 1989. *Fundamentals of digital image processing*, Englewood Cliffs, NJ: Prentice Hall (Reprint).

Kam, Dongjae, Akhil Datta-Gupta. 2016. Streamline-based transport tomography with distributed water arrival times. *SPE Reservoir Evaluation & Engineering* **19** (02): 265-277.

Kam, Dongjae, Jichao Han, Akhil Datta-Gupta. 2017. Streamline-based history matching of bottomhole pressure and three-phase production data using a multiscale approach. *Journal of Petroleum Science and Engineering* **154**: 217-233.

Kang, Suksang. 2014. A model segmentation from spectral clustering: new zonation algorithm and application to reservoir history matching. Proc., SPE Annual Technical Conference and Exhibition, Amsterdam, The Netherlands.

Kang, SukSang, Eric Bhark, Akhil Datta-Gupta et al. 2015. A hierarchical model calibration approach with multiscale spectral-domain parameterization:

Application to a structurally complex fractured reservoir. *Journal of Petroleum Science and Engineering* **135**: 336-351.

Karhunen, Kari. 1947. *Über lineare Methoden in der Wahrscheinlichkeitsrechnung*, Vol. 37, Sana (Reprint).

Kim, H, C Park, B Min et al. 2014. Multiphase flow simulation for in situ combustion to investigate field-scale hydraulic heterogeneity and air injection rate affecting oil production. *Energy Sources, Part A: Recovery, Utilization, and Environmental Effects* **36** (21): 2328-2337.

Kim, Hyunmin, Feyi Olalotiti-Lawal, Akhil Datta-Gupta. 2019. Multi-resolution grid connectivity-based transform for efficient history matching of unconventional reservoirs Proc., SPE/AAPG/SEG Unconventional Resources Technology Conference, Denver, Colorado, USA.

Landa, Jorge L, Roland N Horne. 1997. A procedure to integrate well test data, reservoir performance history and 4-D seismic information into a reservoir description. Proc., SPE Annual Technical Conference and Exhibition, San Antonio, Texas, USA.

Landrø, M, P Digranes, LK Strønen. 2001. Mapping reservoir pressure and saturation changes using seismic methods-possibilities and limitations. *First Break* **19** (12): 671-684.

LaVenue, A. Marsh, John F. Pickens. 1992. Application of a coupled adjoint sensitivity and kriging approach to calibrate a groundwater flow model. *Water Resources Research* **28** (6): 1543-1569. https://doi.org/10.1029/92WR00208.

Lehoucq, Richard B, Danny C Sorensen, Chao Yang. 1998. *ARPACK users' guide: solution of large-scale eigenvalue problems with implicitly restarted Arnoldi methods*, Vol. 6, Siam (Reprint).

Li, Liyong, Seong H Lee. 2008. Efficient field-scale simulation of black oil in a naturally fractured reservoir through discrete fracture networks and homogenized media. *SPE Reservoir Evaluation & Engineering* **11** (04): 750-758.

Loève, M. 1978. Chapter 27. Concept of Conditioning. *Loève, M. Probability Theory* **2**: 3-12.

Lopez, JL, PB Wills, JR La Follett et al. 2015. Real-time seismic surveillance of thermal EOR at Peace River. Proc., SPE Canada Heavy Oil Technical Conference, Calgary, Alberta, Canada.

Lumley, David E. 2001. Time-lapse seismic reservoir monitoring. *Geophysics* **66** (1): 50-53.

Manzocchi, Tom, Jonathan N Carter, Arne Skorstad et al. 2008. Sensitivity of the impact of geological uncertainty on production from faulted and unfaulted shallow-marine oil reservoirs: objectives and methods. *Petroleum Geoscience* **14** (1): 3-15.

Mohar, Bojan. 1997. Some applications of Laplace eigenvalues of graphs. In *Graph symmetry*, 225-275. Springer.

Moinfar, Ali. 2013. Development of an efficient embedded discrete fracture model for 3D compositional reservoir simulation in fractured reservoirs. Doctorate, The University of Texas at Austin.

Olalotiti-Lawal, Feyi, Tsubasa Onishi, Hyunmin Kim et al. 2017. Post-combustion CO2 EOR development in a mature oil field: Model calibration using a hierarchical approach. Proc., SPE Annual Technical Conference and Exhibition, San Antonio, Texas, USA, 20.

Olalotiti-Lawal, Feyi, Tsubasa Onishi, Hyunmin Kim et al. 2019. Post-combustion carbon dioxide enhanced-oil-recovery development in a mature oil field: Model calibration using a hierarchical approach. *SPE Reservoir Evaluation & Engineering*.

Onishi, Tsubasa, Minh C Nguyen, J William Carey et al. 2019. Potential CO2 and brine leakage through wellbore pathways for geologic CO2 sequestration using the National Risk Assessment Partnership tools: Application to the Big Sky Regional Partnership. *International Journal of Greenhouse Gas Control* **81**: 44-65.

Osher, Stanley, James A Sethian. 1988. Fronts propagating with curvature-dependent speed: algorithms based on Hamilton-Jacobi formulations. *Journal of Computational Physics* **79** (1): 12-49.

Park, Han-Young, Akhil Datta-Gupta, Michael J King. 2015. Handling conflicting multiple objectives using Pareto-based evolutionary algorithm during history matching of reservoir performance. *Journal of Petroleum Science and Engineering* **125**: 48-66.

Park, Jaeyoung, Atsushi Iino, Akhil Datta-Gupta et al. 2019. Rapid modeling of injection and production phases of hydraulically fractured shale wells using the fast marching method. Proc., SPE/AAPG/SEG Unconventional Resources Technology Conference, Denver, Colorado, USA.

Park, Jaeyoung, Candra Janova. 2019. SRV characterization and optimum lateral well spacing study of two-well pad in Midland Basin. Proc., SPE/AAPG/SEG Unconventional Resources Technology Conference, Denver, Colorado, USA.

Peters, Lies, Rob Arts, Geert Brouwer et al. 2010. Results of the Brugge benchmark study for flooding optimization and history matching. *SPE Reservoir Evaluation & Engineering* **13** (03): 391-405.

Ping, Jing, Dongxiao Zhang. 2013. History matching of fracture distributions by ensemble Kalman filter combined with vector based level set parameterization. *Journal of Petroleum Science and Engineering* **108**: 288-303.

Przybysz-Jarnut, JK, C Didraga, JHHM Potters et al. 2015. Value of information of frequent time-lapse seismic for thermal EOR monitoring at Peace River. Proc., SPE Annual Technical Conference and Exhibition, Houston, Texas, USA.

Przybysz-Jarnut, JK, PB Wills, MG Araujo et al. 2016. Combining frequent 4D seismic and mechanistic reservoir modeling to improve the effectiveness of steam injection operations. Proc., SPE Annual Technical Conference and Exhibition, Dubai, UAE.

Rao, K Ramamohan, Ping Yip. 2014. *Discrete cosine transform: algorithms, advantages, applications*, Academic press (Reprint).

Rey, Alvaro, Eric Bhark, Kai Gao et al. 2012. Streamline-based integration of time-lapse seismic and production data into petroleum reservoir models. *Geophysics* **77** (6): M73-M87.

Reynolds, Albert C, Nanqun He, Lifu Chu et al. 1996. Reparameterization techniques for generating reservoir descriptions conditioned to variograms and well-test pressure data. *SPE Journal* **1** (04): 413-426.

Sævik, Pål Næverlid, Martha Lien, Inga Berre. 2017. History matching of dual continuum reservoirs—preserving consistency with the fracture model. *Computational Geosciences* **21** (3): 553-565. https://doi.org/10.1007/s10596-017-9632-5.

Sorkine, Olga. Differential representations for mesh processing. Vol. 25, 789-807: Wiley Online Library.

Stovas, Alexey, Børge Arntsen. 2006. Vertical propagation of low-frequency waves in finely layered mediaPropagation of low-frequency waves. *Geophysics* **71** (3): T87-T94.

Strang, Gilbert. 1999. The discrete cosine transform. *SIAM review* **41** (1): 135-147.

Tanaka, Shusei, Dongjae Kam, Akhil Datta-Gupta et al. 2015. Streamline-based history matching of arrival times and bottomhole pressure data for multicomponent compositional systems. Proc., SPE Annual Technical Conference and Exhibition, Houston, Texas, USA.

Tarantola, Albert. 2005. *Inverse problem theory and methods for model parameter estimation*, Philadelphia (Pa.) : SIAM (Reprint). http://lib.ugent.be/catalog/rug01:000846885.

Tikhonov, A. N. 1977. *Solutions of ill-posed problems / Andrey N. Tikhonov and Vasiliy Y. Arsenin ; translation editor, Fritz John*. Washington : New York: Scripta series in mathematics., Winston ; distributed solely by Halsted Press (Reprint).

Tonkin, Matthew, John Doherty. 2009. *Calibration-constrained Monte Carlo analysis of highly-parameterized models using subspace methods*, Vol. 45 (Reprint).

Tura, Ali, David E Lumey. 1999. Estimating pressure and saturation changes time-lapse AVO data. In *SEG Technical Program Expanded Abstracts 1999*, 1655-1658. Society of Exploration Geophysicists.

Vasco, D. W., T. M. Daley, A. Bakulin. 2014. Utilizing the onset of time-lapse changes: a robust basis for reservoir monitoring and characterization. *Geophysical Journal International* **197** (1): 542-556.

Vasco, Don W, Akhil Datta-Gupta, Ron Behrens et al. 2004. Seismic imaging of reservoir flow properties: Time-lapse amplitude changes. *Geophysics* **69** (6): 1425-1442.

Vasco, Donald W, Andrey Bakulin, Hyoungsu Baek et al. 2014. Reservoir characterization based upon the onset of time-lapse amplitude changes. *Geophysics* **80** (1): M1-M14.

Vasco, DW, Henk Keers, Kenzi Karasaki. 2000. Estimation of reservoir properties using transient pressure data: An asymptotic approach. *Water Resources Research* **36** (12): 3447-3465.

Von Luxburg, Ulrike. 2006. A tutorial on spectral clustering. Max Planck Institute for Biological Cybernetics. *Tech Rep*.

Warren, JE, P Jj Root. 1963. The behavior of naturally fractured reservoirs. *Society of Petroleum Engineers Journal* **3** (03): 245-255.

Watanabe, Shingo, Jichao Han, Gill Hetz et al. 2017. Streamline-based time-lapse-seismic-data integration incorporating pressure and saturation effects. *SPE Journal* **22** (04): 1,261-1,279.

Yao, Mengbi, Haibin Chang, Xiang Li et al. 2018. Tuning fractures with dynamic data. *Water Resources Research* **54** (2): 680-707.

APPENDIX A

CONCEPT AND ILLUSTRATION OF PARAMETERIZATION USING BASIS FUNCTION

For high resolution reservoir models, it is almost infeasible to directly calibrate every single grid cell properties. In Figure A.1, if we have an appropriate transformation matrix (Φ), the large property vector (u) can be reduced into much smaller vector (v). u represents the parameters in spatial domain (grid cell properties in a high resolution reservoir model), v is the parameters in spectral domain (basis coefficients) where model calibration is performed, and Φ is the transformation matrix that is consisted of basis functions (Φ_i). Note that the size of v is significantly smaller than u. It enables the history matching problem to be highly regularized by reducing the number of unknowns while keeping the same number of observed data.

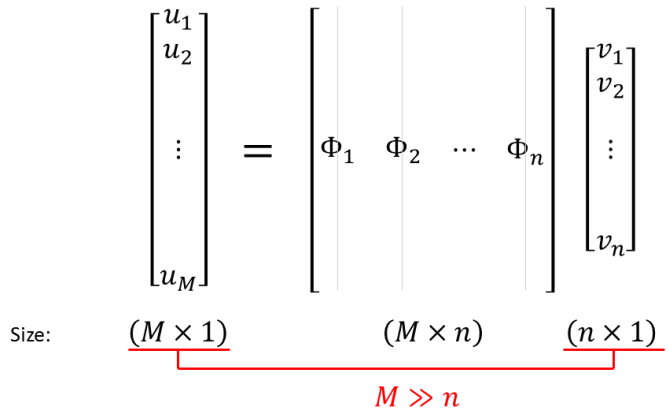

Figure A.1 Linear transform from high resolution reservoir property to parameters in transform domain

Figure A.2 illustrates the re-parameterization using basis functions with a one-dimensional graph for one million reservoir properties. The gray dotted line is the original reservoir property along with the grid cell number. If we utilize three basis functions and corresponding basis coefficients, it is possible to make a low rank approximation of the reservoir properties (Figure A.2(a)). By the parameterization using basis function, the number of parameters is reduced from one million to three. With twenty basis functions, the low rank approximation with higher resolution is computed as in Figure A.2(b). Note that there is a tradeoff between the property resolution and the number of parameters.

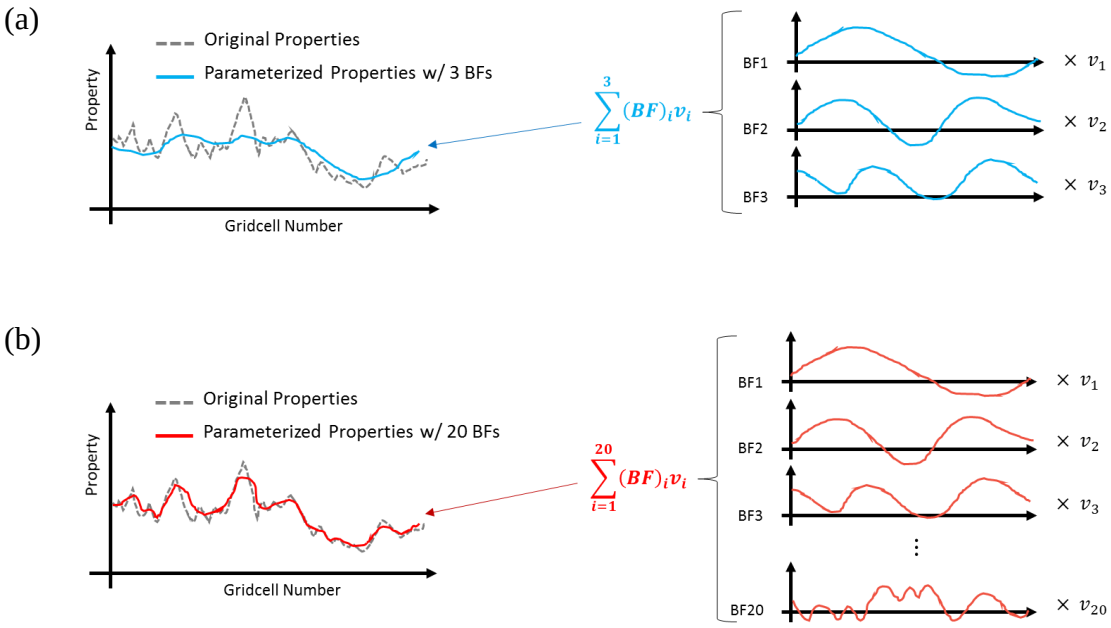

Figure A.2 Illustration of the re-parameterization using (a) three basis functions and (b) twenty basis functions

The original and low rank approximations of two-dimensional permeability field images with respect to different number of basis functions are shown in Figure A.3. The more basis functions we utilize, the more detailed feature of reservoir properties we are able to capture by re-parameterization. Basis functions are the building blocks for the spatial reservoir property distribution.

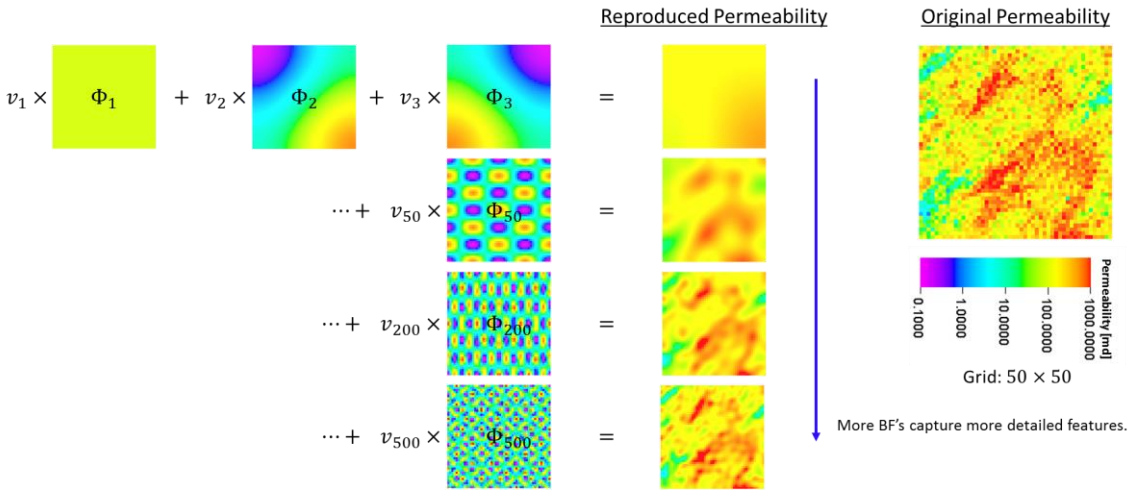

Figure A.3 Illustration of re-parameterization for two-dimensional permeability field with respect to different number of GCT basis functions

APPENDIX B

FRACTURE DISTRIBUTION CALIBRATION

Characterization of fractured reservoir is challenging because of high uncertainty on fracture distribution and properties. The hierarchical multi-scale workflow proposed in Chapter 4 is effective if we have reliable fracture distribution and geometries. If the fracture distribution is not correct, the fracture property calibration would give a geologically unrealistic solution. Even with satisfactory history match results, its prediction will be inaccurate and hence can lead to suboptimal development plan.

We recommend a higher level of hierarchical history matching workflow for fractured reservoir. The first stage is to calibrate fracture distribution with uniform fracture conductivity. After reducing the uncertainty on fracture distribution and geometries, we carry out the second stage to calibrate fracture conductivity as described in Chapter 4. Note that the second stage is also the hierarchical workflow utilizing the extended ABT and streamline-based sensitivity. Several representative fracture distribution models from the first stage can independently step into the second stage for matrix and fracture property calibrations. In this appendix, the first stage of fracture distribution calibration is proposed.

Pixel-based characterization of fractured reservoirs is difficult because of its geometry and non-Gaussian property. Exact location, direction, and length of each fracture is commonly unknown. Hence, a good estimation of the fracture distribution is very important for predicting and optimizing the reservoir production. Ping and Zhang (2013) parameterized fracture distribution by employing level set function to differentiate the

nodes whether fracture can start or not. They transformed non-Gaussian fracture distribution to Gaussian field where each node has Gaussian random number for level set function, fracture length and orientation. Yao et al. (2018) employed Hough-transform method to parameterize non-Gaussian fracture distribution with continuous parameter fields. The purpose of fracture distribution parameterization in their research is mainly on conversion of non-Gaussian field to Gaussian field, so that parameters satisfy the assumption of Ensemble-based inversion methods. The transformed parameter set in their method is too large to be used in non-gradient based inversion methods, however, it is not a drawback in Ensemble-based inversion methods. Remind that the main purpose of parameterization in this study is to regularize the underdetermined history matching problems by reducing parameter set with little loss of spatial heterogeneity information. Therefore, large parameter set size does not coincide with the main purpose of parameterization with non-gradient inversion process. We recommend a new fracture distribution parameterization method resulting in a much smaller parameter set.

We are limited to reduce the uncertainty on fracture distribution in reservoir, to which simulation results are highly sensitive. Therefore, we rather parameterize fracture distribution than explicit individual fractures. Fracture distribution can be represented by three factors in two-dimensional case; statistical distributions of fracture length, angle, and density. In order to control fracture location within reservoir, we employ level set function and GCT basis functions to make a continuous field. A set of GCT basis coefficients determines the region that fractures exist. The workflow of fracture distribution construction with the proposed parameters is shown in Figure B.1.

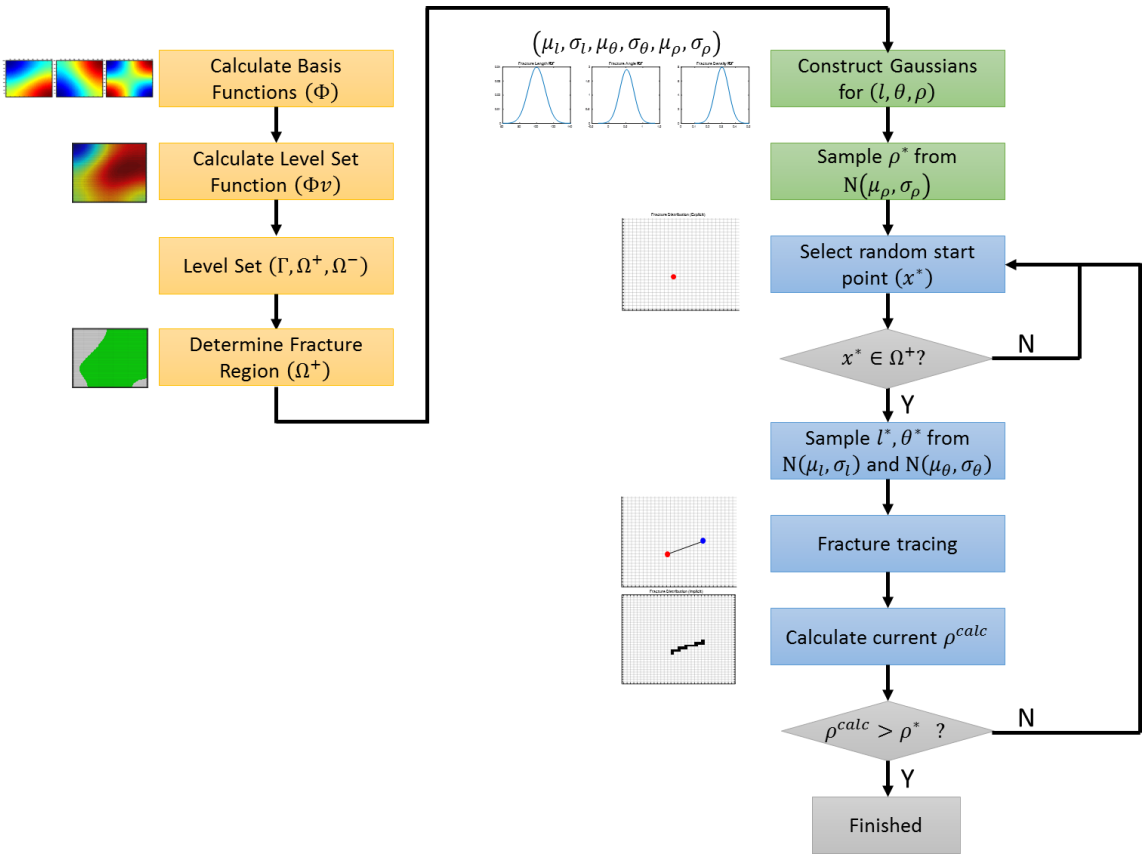

Figure B.1 Workflow of fracture distribution generation

First, we calculate GCT basis function (Φ) and continuous level set function (Φv) with a set of basis coefficients. The number of basis functions and coefficients can be determined based on desired fracture region resolution. After level set (Osher and Sethian 1988), the region that individual fracture can start its geometry is determined (Ω^+). Assuming that fracture length (l), angle (θ), and density (ρ) in a reservoir follow Gaussian distribution, we construct three Gaussian distributions with each mean and standard deviation ($\mu_l, \sigma_l, \mu_\theta, \sigma_\theta, \mu_\rho, \sigma_\rho$). It transforms explicit non-Gaussian fracture

distribution to Gaussian parameters. One value of fracture density (ρ^*) is sampled from its distribution, $N\left(\mu_\rho, \sigma_\rho\right)$, to determine if individual fracture generation should be stopped afterwards. One random coordinate (x^*) is selected and tested if it is within the fracture region (Ω^+). If satisfied, fracture length (l^*) and angle (θ^*) are sampled from each Gaussians, $N\left(\mu_l, \sigma_l\right)$ and $N\left(\mu_\theta, \sigma_\theta\right)$. One fracture geometry can be determined with sampled parameters (x^* , l^* , θ^*). Individual fracture geometry generation is repeated until calculated fracture density (ρ^{calc}) is not less than the sampled one (ρ^*). In this workflow, the parameter set is $\left\langle \mu_l, \sigma_l, \mu_\theta, \sigma_\theta, \mu_\rho, \sigma_\rho, v_1, v_2, v_3, \cdots, v_N \right\rangle$, where N is the number of GCT basis functions. Hence, the number of parameters is $\left(6+N\right)$ which is significantly smaller than the previous studies. Another advantage of the proposed fracture distribution parameterization is that it enables uncertainty quantification even with a single parameter set since it involves random processes. Examples of fracture distribution with a parameter set without fracture region constraint $\left\langle N\left(100,10\right), N\left(\frac{\pi}{6}, \frac{\pi}{15}\right), N\left(0.3, 0.05\right) \right\rangle$ are shown in Figure B.2. For the explicit representation of fractures (Figure B.2(a)), EDFM can be utilized as forward simulation to adopt accuracy and efficiency. If desired to use single porosity model, the pixel-based representation (Figure B.2(b)) in an extremely fine grid can be used. In this case, fast-marching method (FMM) is able to reduce simulation computation load by orders of magnitude (Iino et al. 2017). Fracture distribution parameters are then calibrated to historical production data with any of

efficient forward simulations. Figure B.3 shows more fracture distributions with respect to different parameter sets.

(a)

(b)

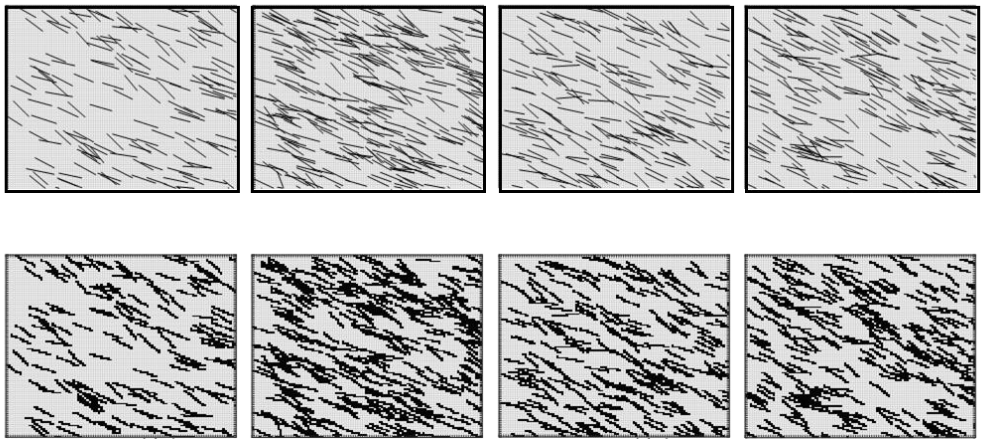

Figure B.2 Examples of fracture distribution with a single parameter set. Representations for (a) Explicit fractures and (b) Pixel-based fractures

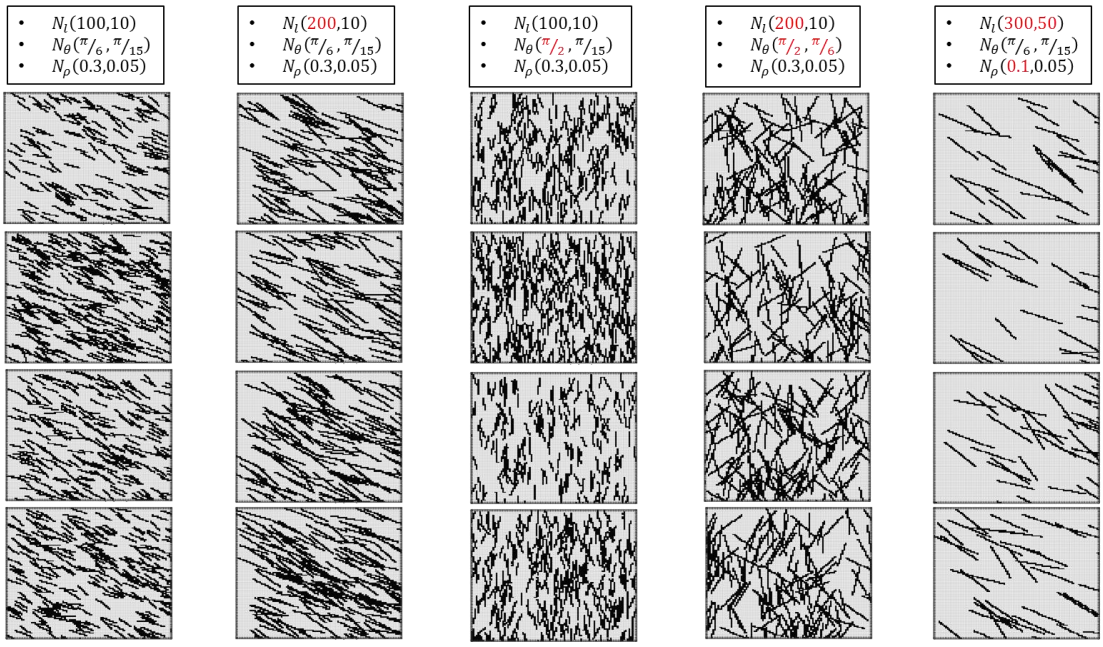

Figure B.3 Fracture distributions with respect to different parameter sets

The impact of fracture region, determined by five GCT basis coefficients in this example and level set method, is demonstrated in Figure B.4 with fixed Gaussian parameters $\left\langle N\left(200,10\right), N\left(\frac{\pi}{2},\frac{\pi}{6}\right), N\left(0.3,0.05\right)\right\rangle$. It is clearly observed that the shape of fracture swarm is controlled by GCT basis coefficients.

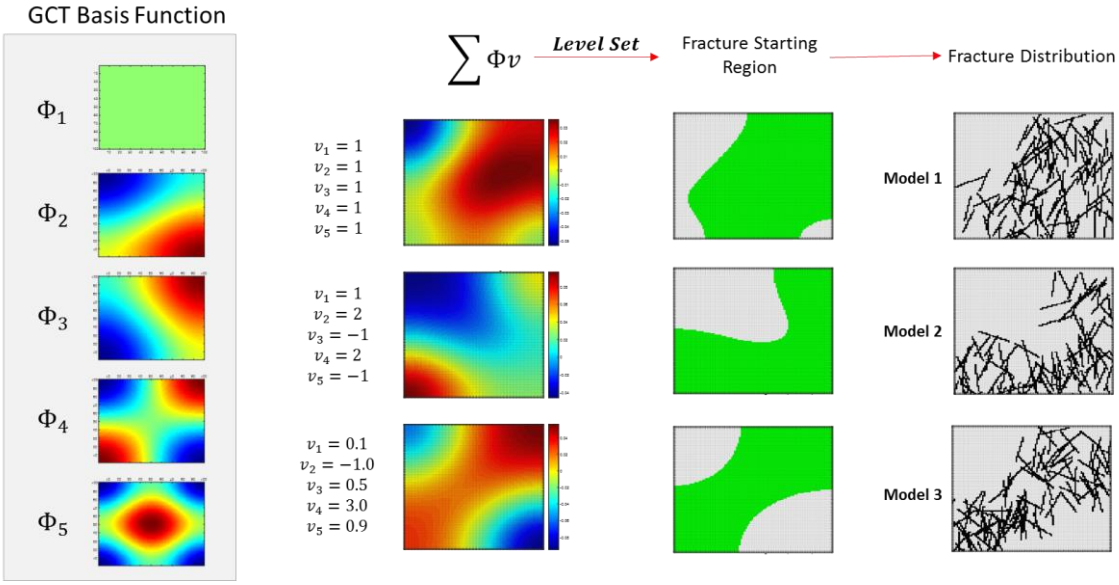

Figure B.4 Fracture distributions with respect to the fracture region, determined by GCT basis coefficients and level set method

Utilizing the proposed fracture distribution parameterization method and efficient forward simulation method (EDFM or FMM), we will be able to reduce the uncertainty on the fracture distribution and geometry. As mentioned above, the fracture/matrix conductivity can be further calibrated by the parameterization method and history matching workflow formulated in Chapter 4. This would make the complete hierarchical calibration workflow for the reservoir with fractures.

APPENDIX C

USER MANUAL FOR PARAMETERIZATION/CLUSTERING SOFTWARE

C.1 Introduction

This is the user manual for parameterization software for all the parameterization methods utilized in this dissertation (GCT, MGCT, ABT, Extended ABT for EDFM) and additional spectral clustering functions. This software is an independent pre-processor before any history matching workflow. It is written in C++ language and compatible with ECLIPSE developed by Schlumberger.

C.2 Overview

The input for this software are input deck file ('Destiny.dip'), grid and initial property files (GRID, EGRID, INIT). The output is basis function files for parameterization and region number for spectral clustering. In order to calculate basis functions, we need an efficient linear algebra tool for the eigen-decomposition of a large and sparse Laplacian matrix. There are two tools employed to the software. (1) ARPACK (Lehoucq, Sorensen, and Yang 1998) and (2) SPECTRA. Therefore, there are two versions of the software, both of which are working identically. Using output files along with history matching tools, efficient model calibration is performed.

C.3 Input Files

C.3.1 Input Data Deck

In the input deck file ('Destiny.dip'), we have to select specific option and provide corresponding information. All options and keywords are described as below.

- DIP_DATA_FILE

  Case Name

  The keyword is followed by a line with case name with an extension 'DATA'. For example, 'CASENAME.DATA'. The software reads other input files (GRID, EGRID, INIT) with the case name specified by this keyword.

- DIP_GCT_SETTING

  Basic Parameterization Setting

  The keyword is followed by a line with 4 records. The records are defined as follows.

1st keyword (String)	Parameterization method – GCT: Grid Connectivity-Based Transform. It can be used for Multiresolution GCT if 'COARSEN' keyword is specified. If 'GCT' is specified, 'DIP_ABT_SETTING' will be ignored. – ABT: Adjacency-Based Transform. If 'ABT' is specified, 'DIP_ABT_SETTING' should be correctly provided. – PCT: Extended ABT for Embedded Discrete Fracture Model (EDFM)
2nd keyword (Boolean)	Bool to generate basis function files – TRUE: Generate basis function files – FALSE: Do not generate basis function files. If the software is used for region definition by spectral clustering, basis function files does not necessarily need to be generated.

3rd keyword (Integer)	Number of basis functions to be generated. If the software is used for region definition by spectral clustering, it can be any number larger than 1.
4th keyword (Boolean)	Bool to make single file for basis functions – TRUE: Write basis functions in a single file ('BF_Final.GRDECL'). If 'DIP_LAYER_SETTING' is specified more than one keyword, it should be set as 'TRUE'. – FALSE: Write basis functions in separate files ('BASIS001.GRDECL', 'BASIS002.GRDECL', …)

- DIP_ABT_SETTING

  ABT Parameterization Setting

  The keyword is followed by a line with 5 records. The records are defined as follows.

1st keyword (Float)	Weight of distance on similarity calculation (σ_X in equation (2.4)). The larger this value is, the larger similarity it calculates. Even though the distance between two grid cells is large, it would consider them similar if this keyword is large. It determines the shape of basis functions along with 2nd keyword, both of which are subjective depending on the reliability of prior model. The recommended first trial value is $-\frac{r^2}{\ln(\varepsilon)}$, where r is the Euclidean cut-off distance which is normally considered as the range of variogram and ε is the negligible value (for example, 0.001).
2nd keyword (Float)	Weight of property difference on similarity calculation (σ_P in equation (2.4)). The larger this value is, the larger similarity it calculates. Even though the property difference between two grid cells is large, it would consider them similar if this keyword is large. It determines the shape of basis functions along with 1st keyword, both of which are subjective depending on the reliability

	of prior model. The recommended first trial value is $S_p\sqrt{range}$, where $S_p = 0.01 \sim 0.02$.
3rd keyword (Integer)	Number of grid cells in I direction for search radius of ABT Laplacian. The software searches grid cells whose indices are within the range [Considering I index – Keyword, Considering I index + Keyword].
4th keyword (Integer)	Number of grid cells in J direction for search radius of ABT Laplacian. The software searches grid cells whose indices are within the range [Considering J index – Keyword, Considering J index + Keyword].
5th keyword (Integer)	Number of grid cells in K direction for search radius of ABT Laplacian. The software searches grid cells whose indices are within the range [Considering K index – Keyword, Considering K index + Keyword].

- DIP_LAYER_SETTING

  Layer Grouping Setting

  This keyword is useful when there are distinct geological units separated by the vertical indices and user desires to generate basis functions separately for each unit.

  The keyword is followed by a line with user specified records (series of integers). Records are the number of layers of each group. User may want to calculate basis functions grouped by several layer groups, usually dependent on distinct geological unit. For example, the reservoir model with 9 layers has three distinct features which can be divided by K indices. Suppose that K index for group 1 is [1, 2], group 2 has [3, 5], and group 3 has [6, 9]. Then this keyword should be the number of layers of each group, '2 3 4'. It makes the output files 'BF_Group_1.GRDECL', 'BF_Group_2.GRDECL', 'BF_Group_3.GRDECL'

that contain basis functions of each group. There will also be the combined basis function file, 'BF_Final.GRDECL'. If there is no specific group and user want to calculate basis functions for the entire layer, this keyword should be '9'. Keep in mind that the summation of records should be exactly same as the total number of layers in the model.

- COARSEN

  Grid Coarsening Setting

  The keyword is followed by user defined lines with 9 records (series of integers) for each line. This keyword setting is required to calculate multiresolution GCT (MGCT) basis functions. When preparing other input files (GRID, EGRID, INIT), the initialization simulation should be run with 'COARSEN' keyword in ECLIPSE data deck. The definition of each record is exactly following ECLIPSE 'COARSEN' setting as below. If MGCT is not required, user needs to remove this keyword. Due to coarsening, there are sparse nonzero values for the coarsened region in 'BF_Final.GRDECL' file. For visualization purpose, those sparse nonzero values are copied to the rest of the coarsened region in 'BF_full_Group_#.GRDECL' file.

1st keyword (Integer)	Lower I index of the coarsening region
2nd keyword (Integer)	Upper I index of the coarsening region
3rd keyword (Integer)	Lower J index of the coarsening region

4th keyword (Integer)	Upper J index of the coarsening region
5th keyword (Integer)	Lower K index of the coarsening region
6th keyword (Integer)	Upper K index of the coarsening region
7th keyword (Integer)	Number of coarsened cells along the I direction in this coarsening region
8th keyword (Integer)	Number of coarsened cells along the J direction in this coarsening region
9th keyword (Integer)	Number of coarsened cells along the K direction in this coarsening region

- CLUSTER_SETTING

  Spectral Clustering Setting

  The keyword is followed by a line with 3 records. Please refer to Kang et al. (2015) for the theoretical backgrounds of spectral clustering. If dividing the reservoir only by its grid structure, user needs to specify the 1st keyword as 'GCT' in DIP_GCT_SETTING. If considering prior model property, it should be 'ABT' and DIP_ABT_SETTING should also be correctly provided. If clustering is not required, user needs to remove this keyword. The output is the array of region numbers for all grid cells, ranging [1, Number of clusters] and zero for inactive grid cells in 'Cluster_Group_#.GRDECL'. The records are defined as follows.

1st keyword (String)	Clustering method – RCUT: Ratio cut. It is to find a 'cut', which is relaxed by the vertices between clusters. – NCUT: Normalized cut. The size of clustering is measured by the weights of its cutting edge. – RCC: Ratio Cheeger cut. The Cheeger constant is a measurement of 'bottleneckedness' in a graph.

	– NCC: Normalized Cheeger cut. It is optimized by the minimum volume of clusters.
2nd keyword (Integer)	Number of clusters
3rd keyword (Integer)	Clustering threshold type – 0: Zero – 1: Median – 2: Mean – -1: Optimal

C.3.2 Reservoir Simulation Output Files

Grid and initial property files (GRID, EGRID, INIT) should be prepared by the initialization simulation by ECLIPSE with 'NOSIM' keyword.

C.3.3 ARPACK Library Files

SPECTRA version does not require any library files. However, ARPACK library files are required to run the software of the ARPACK version. The library files for Windows 64 bit system are as below.

- Arpack_win64.dll
- libgcc_s_sjlj-1.dll
- libgfortran-3.dll
- libquadmath-0.dll

C.4 Code Structure

For future developer, main code structure is explained in this section. The descriptions are common for both versions of softwares.

The software commences with the main source code, 'DESTINY.cpp'. All the parameterizations are performed by 'runInversion(&p_PROJECT)' function in 'DIPGCT.cpp' file, as shown in Figure C.1.

```
int main (int argc, char** args)
{

    clock_t t = clock();

    bool fileWrite = false;
    if( fileWrite ) {
        FILE *stream ;
        if((stream = freopen("destiny.prt", "w", stdout)) == NULL)
          return 0;
        freopen( "DESTINY.PRT", "w", stdout );
    }

    cleanDir();

    //! Project File name
    string pFileName;
    if(argc==1) pFileName = DIP_FILE; //"chears.genopt";
    else pFileName = args[1];

#ifdef __unix
    dos2unix( pFileName );
#endif

    //! Defining class to load project
    CPROJECT p_PROJECT;
    p_PROJECT.load_project( pFileName.c_str() );

    //! ------------------------------
    //! Parameterization
    //! ------------------------------
    if ( p_PROJECT.m_bGCT || p_PROJECT.m_bABT || p_PROJECT.m_bPCT) {
        CDIPGCT *p_DIPGCT;
        p_DIPGCT = new CDIPGCT;
        p_DIPGCT->runInversion(&p_PROJECT);

        // for Clustering [Hyunmin.Kim]
        if (p_PROJECT.m_iClusterCriterion == 1 || p_PROJECT.m_iClusterCriterion == 2 ||
            p_PROJECT.m_iClusterCriterion == 3 || p_PROJECT.m_iClusterCriterion == 4){


        }
    }
    else {
        printf(" Something wrong with the input.\n");
    }
```

Figure C.1 Main function for parameterization in the main source code (DESTINY.cpp)

In ‘runInversion(&p_PROJECT)’ function of ‘DIPGCT.cpp’ file, it prompts to read grid geometry and grid property with ‘scan_static_data(0)’ function. After reading all grid information, ‘generateGCTBasis()’ function is called to generate basis functions as shown in Figure C.2.

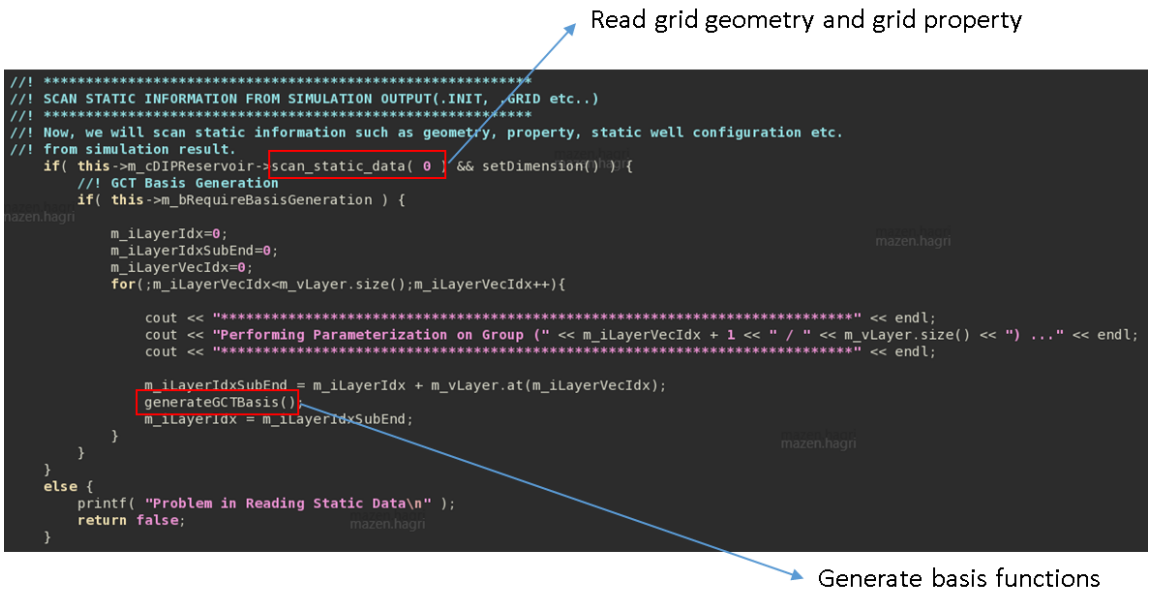

Figure C.2 Code to call functions to read grid information and generate basis functions (‘runInversion(&p_PROJECT)’ function of ‘DIPGCT.cpp’ file)

The core part of the software is ‘generateGCTBasis(void)’ function in ‘DIPGCT.cpp’ file. According to the types of parameterization, it uses corresponding function to calculate basis functions. If ABT basis functions are to be calculated, it calls ‘constructABTMatrix()’ function. Otherwise, if GCT or PCT are required, it calls

'storeAdjecentCells()' function to save the grid connectivity information, and 'CheckSimulationNNC()' function to save non-neighbor connections from the extended grid (EGRID) file. After saving all the information for the desired parameterization method, it calls 'constructLaplacian()' function to construct Laplacian matrix and eigen-decompose it to generate the desired number of basis functions. In this function, either ARPACK or SPECTRA is used to efficiently eigen-decompose a large sparse matrix. If the developer is to replace the eigen-decomposition tool, the source codes in this function need to be modified. In order to write basis functions in a text file, it calls 'generateGCTBasisModels(m_iNumberOfModels)' function. The above descriptions are shown in Figure C.3.

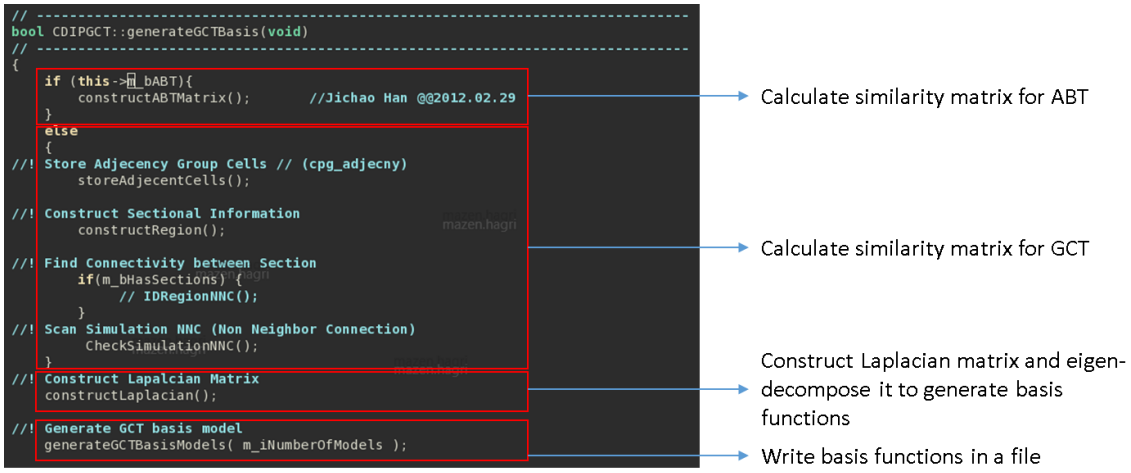

Figure C.3 Core part of the software ('generateGCTBasis(void)' function in 'DIPGCT.cpp' file)

APPENDIX D

WEIGHTING FUNCTIONS OF SIMILARITY

Incorporation of reliable prior knowledge is beneficial to reservoir model characterization. As one of efficient and practical parameterization methods, ABT is explained and applied to the field case in Chapter 2. The similarity of ABT is defined as equation (D.1).

$$a_{i,j} = \exp\left(\frac{-\left\|p_i - p_j\right\|_2^2}{\sigma_p}\right)\begin{cases}\exp\left(\dfrac{-\left\|x_i - x_j\right\|_2^2}{\sigma_x}\right) & \text{if } \left\|x_i - x_j\right\| < r \\ 0 & \text{otherwise}\end{cases} \tag{D.1}$$

where $p_{i,j}$ is the property value of grid cell, $x_{i,j}$ is the coordinate of grid cell centroid, and r is a Euclidean cutoff distance, beyond which a similarity is considered as zero regardless of their properties and distance. σ_p and σ_x are weighting functions to determine the strictness of similarity between adjacent grid cells, regarding distance and grid property, respectively. The smaller the weighting function is, the stricter it calculates the similarity. It means that we consider the adjacent grid cells as more similar if we have larger weighting functions. As an extreme case, if both weighting functions are significantly large, then two kernel functions will be unity within the Euclidean cutoff distance. It results in the Laplacian matrix consisting only of zero and unity, similar to grid Laplacian. On the other hand, if either of weighting functions is extremely small, the Laplacian matrix will be almost zero matrix and eigen-decomposition is not feasible in this case.

Determination of the weighting functions, therefore, is admittedly subjective step, and there is no general rule. Although there have been guidelines on how to determine the weighting functions (Bhark, Datta-Gupta, and Jafarpour 2011, Kang 2014), it still requires iterative trial and error on both weighting functions to select appropriate basis functions.

In order to mitigate subjectivity on weighting functions, alternative definition of similarity is proposed by 'diffusive time of flight' (DTOF). It is a representation of the travel time of pressure propagation in the reservoir. Therefore, the DTOF embeds the distance and reservoir properties as in equation (D.2).

$$\left|\nabla \tau\right| = \frac{1}{\sqrt{\alpha}} \tag{D.2}$$

where τ is DTOF and α is the diffusivity defined as $\alpha = k / \phi \mu c_t$. As the DTOF also embeds fluid source and sink locations, it can lead to more effective basis functions (in terms of model calibration by flow simulation) which reflect flow patterns in the reservoir. In addition, incorporated with fast-marching method (FMM), it is able to reduce simulation computation load by orders of magnitude (Iino et al. 2017).

The similarity of ABT on DTOF is defined as in equation (D.3). Subjectivity on the weighting function of distance is removed by incorporating distance and property into the DTOF.

$$a_{i,j} = \begin{cases} \exp\left(\dfrac{-\left\|\tau_i - \tau_j\right\|_2^2}{\sigma_\tau}\right) & \text{if neighbored} \\ 0 & \text{otherwise} \end{cases} \tag{D.3}$$

For example, two-dimensional synthetic reservoir model with a horizontal well is parameterized based on permeability and DTOF, respectively. Figure D.1 shows the permeability field and DTOF.

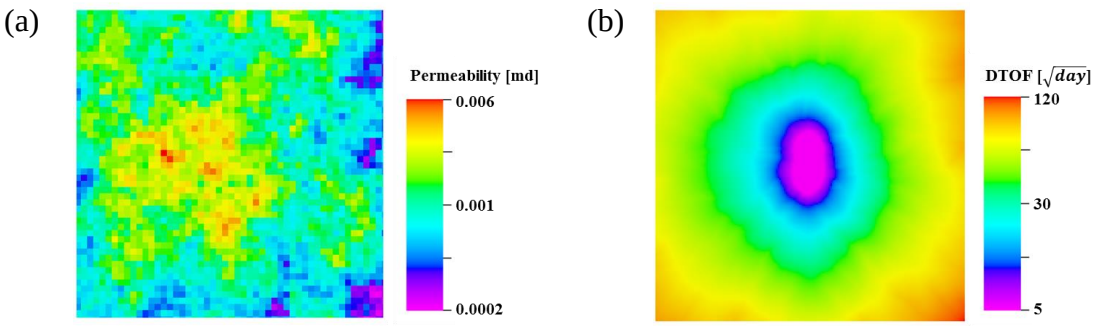

Figure D.1 (a) Permeability field and (b) diffusive time of flight for two-dimensional synthetic reservoir model with a horizontal well

ABT basis functions are compared as in Figure D.2. Notice that basis functions of DTOF reflect the flow pattern incurred by horizontal producer at the center. The reconstructed permeability field and DTOF map are shown in Figure D.3 with respect to different number of ABT basis functions. Notice here that the parameterization of DTOF is more effective than permeability field, that is, the important features of the reference property can be captured with smaller number of basis functions. It is resulted by incorporating distinct rock and fluid properties into the DTOF which has more simple and smooth patterns and influences the flow pattern.

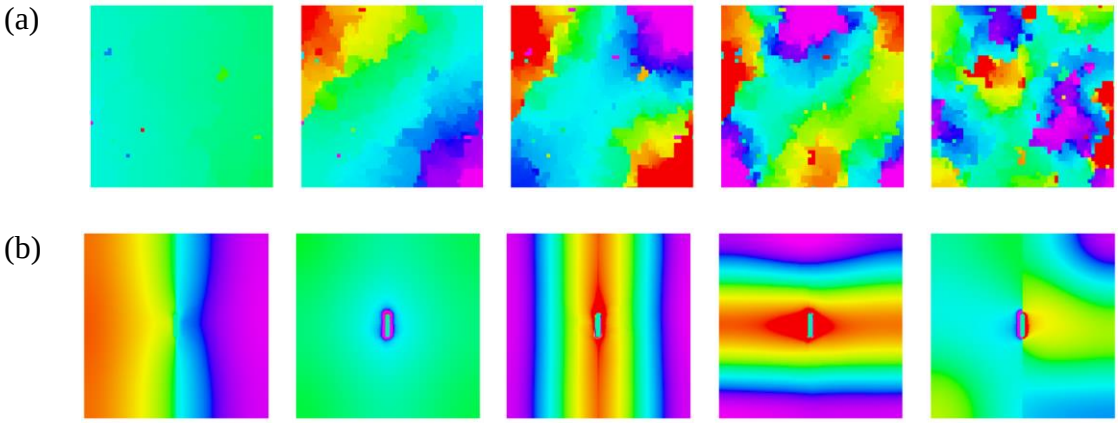

Figure D.2 ABT basis functions of (a) permeability field and (b) DTOF

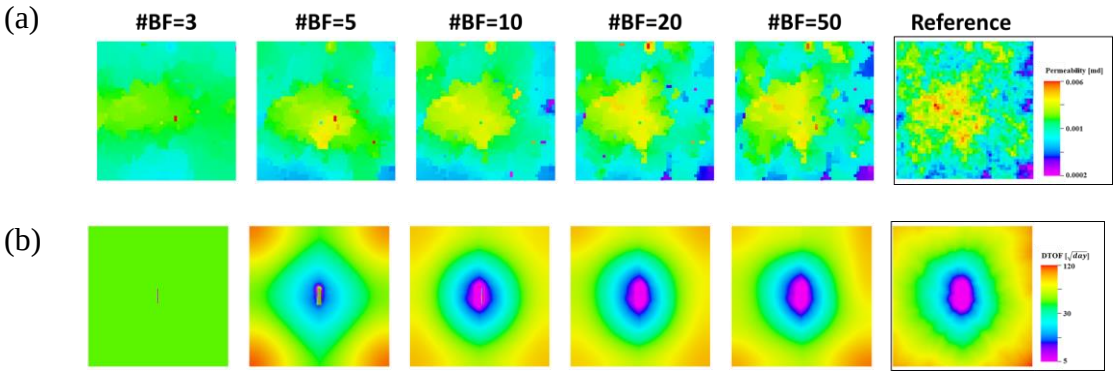

Figure D.3 Reconstructed property distributions for (a) permeability field and (b) DTOF